

THESIS FOR THE DEGREE OF DOCTOR OF PHILOSOPHY IN CHEMISTRY

Hydrous iridium oxide for *in situ* pH
sensing
electrodeposition, properties and applications

by

Patrick Steegstra



UNIVERSITY OF GOTHENBURG

Department of Chemistry and Molecular Biology
University of Gothenburg
Gothenburg, Sweden 2013

Hydrous iridium oxide for *in situ* pH sensing: *electrodeposition, properties and applications*

© Patrick Steegstra, 2013

Department of Chemistry and Molecular Biology
University of Gothenburg
412 96 Gothenburg, Sweden

ISBN 978 91 628 8479 6

Typeset with L^AT_EX2e

All images prepared with Python (Matplotlib, Numpy & Scipy), Gimp, Inkscape and ImageJ

Printed by Kompendiet
Göteborg, Sweden 2013

So it goes...

Kurt Vonnegut Jr.

Abstract

For heterogeneous processes, such as electrochemical reactions taking place at an electrode, the chemical conditions at the reaction interface can differ significantly from the bulk. Consumption of reactants leads to local depletion, whereas product formation results in excess concentration. For reactions involving protons and hydroxide ions, these changes can be described in terms of local pH. In this thesis, a method to measure near surface pH with rotating ring disc electrodes (RRDE) was investigated. In this method, the RRDE is not used in the classical generator collector mode with amperometric detection on the ring, but with the ring as a potentiometric pH sensor. Hydrous iridium oxide films (HIROF) were electrodeposited to serve as thin film pH sensors.

The chemistry of the deposition medium used for preparing the HIROFs was studied in detail. The existence of crystalline nanoparticles in the film was proven by transmission electron microscopy. HIROF exhibit a pH response greater than 60 mV, up to 90 mV, depending on the amount of crystalline matter and the redox buffering in the film. Variations in the pH sensitivity were related to the average oxidation state, by measuring titration curves after potential conditioning at different potentials. The pH sensitivity followed the cyclic voltammogram (CV) of HIROF, with two maxima near the two redox couples in the CV.

The films did not fully adapt to conditioning potentials more positive than the first redox couple. This phenomenon was discussed within the context of a DFT study on the binuclear mechanism for the oxygen evolution reaction. Combination of experimental observations and results from DFT calculations, revealed that the full oxidation of Ir(IV) to Ir(V) oxide is inhibited and only partial oxidation to Ir(V) is allowed before the start of oxygen evolution.

After determining the pH sensing properties of HIROFs, films were deposited on the ring of RRDEs and successfully used in *in situ* near surface pH measurements. The ocp of HIROF ring electrode was measured, during water and oxygen reduction on the disc. Next, the ocp values were correlated to pH, using calibration curves measured in standard buffer solutions, to obtain information on the near surface pH changes

Hydrogen peroxide, a redox compound, is one of the products of O₂ reduction. Redox reactions between the EIROF and such species, could hinder pH measurements. However, for low H₂O₂ concentrations, a suitable potential conditioning of the HIROF, was shown to subdue this influence. Thus, optimisation for systems under study is possible, facilitating *in situ* pH measurements even in the presence of electroactive substances in solution.

Finally, the growth of ZnO rods was studied, with focus on electrodeposition on gold. Deposition is induced by changing near surface pH with a electrochemical reaction, like oxygen reduction, to induce precipitation of ZnO onto the electrode. The current density, related to the local pH, was found to have a profound influence on coverage density and rod dimensions.

Keywords: hydrous iridium oxide, zinc oxide, electrodeposition, pH sensor, oxidation state, RDE, RRDE, SEM

List of publications

This thesis is based on the papers presented below. In the text these papers will be referred to by their roman numerals.

- I** Involvement of nanoparticles in the electrodeposition of hydrous iridium oxide
P. Steegstra and E. Ahlberg, *Electrochimica Acta*, **2012**, 68, 206–213
- II** Influence of oxidation state on the pH dependence of hydrous iridium oxide films
P. Steegstra and E. Ahlberg, *Electrochimica Acta*, **2012**, 76, 26–33
- III** *In situ* pH measurements with hydrous iridium oxide in a rotating ring-disc configuration
P. Steegstra and E. Ahlberg, *Journal of Electroanalytical Chemistry*, **2012**, 685, 1–7
- IV** pH controlled electrochemical Ir oxidation by suppression of the competing oxygen evolution reaction
P. Steegstra, M. Busch, I. Panas and E. Ahlberg, *manuscript*
- V** Deposition of ZnO rods by electrochemically induced hydrolysis
P. Steegstra and E. Ahlberg, *Submitted to Journal of Physical Chemistry C*

Publications not included in the thesis

- Encapsulation of emulsion droplets by organo–silica shells
C.I. Zoldesi, P. Steegstra, A. Imhof
Journal of Colloid and Interface Science, **2007**, 308, 121–129
- Improved Proton Conductivity in Spark-Plasma Sintered Dense Ceramic $\text{BaZr}_{0.5}\text{In}_{0.5}\text{O}_{3-\delta}$
I. Ahmed, F.G. Kinyanjui, P. Steegstra, Z.J. Shen, S.G. Eriksson and M. Nygren
Electrochemical and Solid-State Letters, **2010**, 13, B130–B134
- Proton Conductivity in Mixed B-Site Doped Perovskite Oxide $\text{BaZr}_{0.5}\text{In}_{0.25}\text{Yb}_{0.25}\text{O}_{3-\delta}$
I. Ahmed, F.G. Kinyanjui, S.M.H. Rahman, P. Steegstra, S.G. Eriksson and E. Ahlberg
Journal of the Electrochemical Society, **2010**, 157, B1819–B1824
- Effect of co-doping on proton conductivity in perovskite oxides $\text{BaZr}_{0.9}\text{In}_{0.05}\text{M}_{0.05}\text{O}_{3-\delta}$ ($\text{M} = \text{Yb}^{3+}$ or Ga^{3+})
I. Ahmed, S.M.H. Rahman, P. Steegstra, S.T. Norberg, S.G. Eriksson, E. Ahlberg C.S. Knee and S. Hull *International Journal of Hydrogen Energy*, **2010**, 35, 6381–6391

Statement of contribution

- I** Designed and performed all experiments, responsible for data evaluation, with support from co-author, lead author with support from co-author.
- II** Designed and performed all experiments, responsible for data evaluation, with support from co-author, lead author with support from co-author.
- III** Designed and performed all experiments, responsible for data evaluation, with support from co-author, lead author with support from co-author.
- IV** Designed and performed all experiments. Lead author on the experimental part of the paper and author in collaboration with co-authors on the discussion and conclusions. Theoretical calculations were carried out by M. Busch and evaluated by M. Busch and I. Panas.
- V** Designed and performed all experiments, responsible for data evaluation, with support from co-author, lead author with support from co-author.

List of abbreviations and symbols

AIROF	Anodic Iridium Oxide Film
CA	Chronoamperometry
CBD	Chemical Bath Deposition
CE	Counter Electrode
CP	Chronopotentiometry
CV	Cyclic Voltammetry
CVD	Chemical Vapour Deposition
DFT	Density Functional Theory
DLS	Dynamic Light Scattering
EDX	Energy Dispersive X-ray Spectroscopy
EIROF	Electrodeposited Iridium Oxide Film
EIS	Electrochemical Impedance Spectroscopy
HER	Hydrogen Evolution Reaction
HIROF	Hydrous Iridium Oxide Film
HMT	Hexamine (Hexamethylenetetramine)
IROF	Iridium Oxide Film
LSV	Linear Sweep Voltammetry
NHE	Normal Hydrogen Electrode
ocp	Open Circuit Potential
OER	Oxygen Evolution Reaction
ORR	Oxygen Reduction Reaction
RDE	Rotating Disc Electrode
RE	Reference Electrode
RHE	Reversible Hydrogen Electrode
RRDE	Rotating Ring-Disc Electrode
SEM	Scanning Electron Microscopy
SIROF	Sputtered Iridium Oxide Film
TEM	Transmission Electron Microscopy
TM	Transition Metal
WE	Working Electrode

A	area
C_X	concentration of species X
C_X^*	bulk concentration of species X
C_X^0	surface concentration of species X
D_X	diffusion coefficient of species X
e	electron
i	current
j	current density
J_X	flux of species of X
k_B	Boltzmann constant
n	number of electrons
O	oxidised species
p, q	stoichiometric constants
r	radius
R	reduced species
R_H	hydrodynamic radius
R_{rd}	ohmic resistance between ring and disc
T	temperature
v	scan rate
y	normal distance to the electrode
δ	diffusion layer thickness
η	viscosity
κ	conductivity
ν	kinematic viscosity of the electrolyte
Φ	electric potential
χ	electronegativity
ω	rotation rate (rad/s)

Contents

List of publications	vi
Statement of contribution	vii
List of abbreviations and symbols	viii
Contents	xi
1 Introduction	1
2 Background	5
2.1 A short history of iridium	5
2.2 Iridium oxides	7
2.3 Hydrous iridium oxide films	8
2.3.1 Anodic iridium oxide films	8
2.3.2 Electrodeposited iridium oxide films	9
2.4 Colloidal iridium oxide	10
2.5 pH sensing	11
2.5.1 General	11
2.5.2 Metal oxide pH sensors	12
2.6 RRDE – pH measurements	14
2.7 Zinc oxide	16
2.7.1 Solution chemistry	18
2.7.2 ZnO electrodeposition	19
3 Theory	21
3.1 Electrochemical techniques	21
3.1.1 Cyclic voltammetry	21
3.1.2 Rotating electrodes	23
3.2 Dynamic light scattering	29

3.3	Electron microscopy and energy dispersive X-ray spectroscopy	30
3.3.1	SEM & EDX	30
3.3.2	TEM	31
4	Experimental	33
4.1	Electrochemical equipment	33
4.1.1	Potentiostats	33
4.1.2	Cells and electrode setup	33
4.1.3	Electrodes	34
4.2	UV-Vis spectroscopy	34
4.3	Electron microscopy and energy dispersive X-ray spectroscopy	34
4.4	Dynamic light scattering	35
4.5	Iridium oxide deposition	35
4.5.1	Preparation of the IrO ₂ deposition solution	35
4.5.2	Electrodeposition of iridium oxide	36
4.6	Zinc oxide deposition	36
5	Iridium oxide deposition	37
5.1	Introduction	37
5.2	Solution preparation	37
5.3	Solution aging	40
5.4	Iridium oxide nanoparticles	41
5.5	Electron microscopy	43
5.6	Conclusions	48
6	pH sensing properties of hydrous iridium oxide	49
6.1	Introduction	49
6.2	Film preparation	49
6.3	pH measurements	50
6.4	Oxidation state	53
6.4.1	Experiments and results	53
6.4.2	Acid base argument	56
6.4.3	Anhydrous vs hydrous contributions	58
6.5	Electrochemical properties and DFT	60
6.5.1	Models and mechanisms	60
6.5.2	Results	61
6.5.3	Interpretation of iridium oxide CV	63
6.6	Conclusions	64

7	RRDE pH measurements with iridium oxide	67
7.1	Introduction	67
7.2	EIROF pH sensing properties and H ₂ O ₂	68
7.3	RRDE preparation	70
7.4	Correction of the ring potentials	71
7.5	RRDE-pH current step experiments	71
7.5.1	Experimental	71
7.5.2	Results and discussion	72
7.6	RRDE-pH Linear sweep voltammetry	75
7.6.1	Experimental	75
7.6.2	Results and discussion	76
7.7	Practical considerations	77
7.8	Conclusions	79
8	Zinc oxide deposition	81
8.1	Introduction	81
8.2	Chemical growth	81
8.3	Electrodeposition	83
8.3.1	Morphology	84
8.3.2	Deposition curves	88
8.3.3	Surface pH	89
8.4	Conclusions	91
9	Conclusions and future work	93
9.1	Future work	95
	Acknowledgements	97
	Bibliography	99

1 Introduction

This thesis is about a meeting between two oxides, where one was investigated with the intend to use it for studying the formation of the other. However, during the project focus shifted and the intended tool became the centre of attention.

The main task specified at the start of the project was to investigate the electrochemical deposition of zinc oxide, as an alternative to chemical bath and vapour deposition. ZnO is grown electrochemically by making use of its amphoteric nature.¹⁻³ At high and low pH it is highly water soluble, but at intermediate pH values the solubility decreases several orders of magnitude.^{4,5} By using an electrochemical process to induce pH changes at an electrode surface, one can locally minimise the solubility of ZnO and force precipitation onto the electrode.^{2,3,5} Therefore, this process is sometimes, more correctly, referred to as electroprecipitation.⁶ In this work, however, the term electrodeposition will be used.

Since these pH changes only occur near the surface it is not straightforward to measure at what pH the precipitation takes place. A possible approach is to place a small pH electrode close to the surface, but this would affect local mass transport.^{5,7} Another solution is to use an electrochemical time of flight method⁸ or, the choice at present, a rotating ring-disc electrode (RRDE).⁹

The RRDE is a well known and widely used piece of equipment in electrochemical laboratories. It consists of two electrodes embedded in a cylinder: a disc electrode in the centre surrounded by a concentric ring electrode, separated by an insulating gap.¹⁰ By rotating the electrode, a well defined and well described convective flow is induced, which transports reaction products from the disc to the ring, where they can be detected.^{7,10,11} Most commonly the ring is held at a fixed potential to quantitatively oxidise

or reduce the reaction products for amperometric detection. A classic example is the study of the oxygen reduction reaction (ORR), where hydrogen peroxide produced on the disc, can be detected on the ring by oxidation.¹²

In this thesis work the RRDE was used in a different manner: one that was first described by Albery *et al.* In this approach the ring of the RRDE is covered with a film that is sensitive to the analyte (*e.g.* protons or hydroxide ions) and its open circuit potential is measured, to detect changes in analyte concentration.^{9,13–15} Thus, instead of an amperometric sensor the ring is used as a potentiometric sensor.

To measure pH with this technique iridium oxide was chosen as the sensing material on the ring. A hydrated form of iridium oxide is easily electrodeposited on a variety of substrates and has good pH sensing properties.^{16–18} Hydrated iridium oxide is an interesting material in itself: the pH sensitivity is higher than what is commonly seen for other systems;¹⁹ its cyclic voltammogram shows two features, which is well known, but not fully explained; and its electrodeposition, albeit commonly used, has not been researched much in itself. This soon led to the promotion of iridium oxide from tool to topic.

The content of this thesis is based on a series of papers: four on iridium oxide and one on zinc oxide. Each paper roughly corresponds to one chapter, but contents were reorganised where suitable, to provide a more congruous whole. After, presenting some background, theory and experimental details in Ch. 2, 3 and 4, the contents of the five papers will be presented as follows.

In paper I the preparation of the iridium oxide deposition medium was investigated. The contents are presented in Ch. 5, with the exception of preliminary pH measurements. These results were moved to Ch. 6 to allow discussion within the context of the extensive pH measurements that form the topic of Paper II. The pH measurements presented in Paper II were carried out in preparation of RRDE pH measurements on the oxygen reduction reaction. Since, hydrogen peroxide is formed in the ORR on gold, the influence of this compound on iridium oxide was tested.¹² These results are presented in Ch. 7 together with the results on the RRDE pH experiments published in Paper III.

In Sec. 6.5 an experimental and theoretical study is presented that attempts to provide insight into the processes responsible for the double featured voltammetry of iridium oxide. This study evolved from Paper II and earlier work by Busch *et al.* on the mechanism of the oxygen evolution reaction (OER) on transition metal oxides. The results will be published in Paper IV, which is currently in preparation.

The last paper based chapter, Ch. 8, concerns the electrochemical deposition of ZnO on gold rotating disc electrodes, with emphasis on the influence of near surface pH. The results presented in this chapter, lead to the interest into performing RRDE pH measurements and to Paper V.

Finally, this thesis will be finished with conclusions and a brief future outlook in Ch. 9.

2 Background

Because of the overlap in subject matter, of the papers that form the basis of this thesis, background information was collected into a single chapter. Here, a literature context is provided on which the work presented in later chapters was founded. The chapter starts with a short history of iridium, the main element in this thesis.

2.1 A short history of iridium

The discovery of iridium is closely linked to that of its companion platinum metals: rhodium, palladium and osmium. The discovery of these four elements were all presented between 1803 and 1805, by William Hyde Wollaston and Smithson Tennant.^{20,21}

In 1797, Wollaston set out to find a convenient and reproducible method for refining raw platinum ore and in 1800 his study friend Smithson Tennant joined this endeavour.²¹ Tennant was known as a talented chemist, but he had an additional asset. By the age of 20 he had sadly lost both parents, who left him a significant inheritance. This enabled the two men to purchase the considerable amount of 178 kg raw platinum ore from the Viceroyalty of New Granada, modern day Colombia.²⁰

After dissolving the platinum ore in *aqua regia* a black residue was left, which had been spotted earlier by the French chemists, Vauquelin. Fourcroy and, in an independent study, Descotils.²² The task of analysing the solution and residue was split. Wollaston went on to discover palladium and rhodium in the solution part, while Tennant worked on the residue. The

sheer amount of residue left, some 3 kg, allowed Tennant to perform much more detailed experiments than his French competitors who only had trace amounts to work with. Initial suggestions were that the material was a form of 'plumbago', the mineral form of graphite.²² However, Tennant's experiments proved that this black powder was considerably more interesting in nature.

First, the powder was fused with NaOH at red heat. The melt was then cooled and dissolved in water, resulting in a yellow, pungently smelling solution. A significant amount of residue was left, which was added to HCl, giving a deep blue solution. Again a residue was left behind though, which was once more fused with NaOH, and subjected again to the steps just described. By repeating this procedure all powder was eventually dissolved. Tennant realised two new metals were present in the solutions, but each containing an excess of only one.

Neutralisation of the alkaline solution gave a pale and volatile precipitate. A pungently smelling, but sweetish, solution of pure OsO₄ was obtained by distillation. It is to this compound that Osmium – Greek for smell – owes its name.^{21,22} The metal was obtained by shaking the OsO₄ solution with mercury, forming an amalgam, followed by filtering and distilling off the mercury.²²

The initially dark blue acidic solution turned olive green and eventually deep red upon heating. From the red solution, dark red crystals were obtained after recrystallisation, which most likely consisted of Na₂[IrCl₆] · nH₂O.²¹ By heating the crystals, a silvery white, so far unknown, metal was isolated. Owing to the great variety of colours this newly discovered metal took in hydrochloric acid, it was named iridium, after *iris*: the Greek goddess and personification of the rainbow.^{21,22}

Iridium turned out to be among the densest and hardest metals known and could not be melted by any means available at the time.^{22,23} It would take until 1813 before iridium was melted in experiment. In 1800 Alessandro Volta had discovered the voltaic pile, which had since been used by Sir Humphrey Davy to isolate sodium and potassium.²⁴ John George Children, a friend of Davy, had become interested in these electrochemical experiments and in 1813 presented a galvanic pile containing 20 copper and zinc plates, each measuring 1.82 m by 0.81 cm. The stack was placed in 4 m³ of dilute nitric and sulfuric acid.^{23,25} Under supervision of 38 friends, among whom W.H. Wollaston, Children managed to partially melt a piece of iridium. In 1815 he succeeded in the complete melting of an iridium sample, after optimising the galvanic pile and adding an additional copper plate to each

copper/zinc pair, on the advice of Wollaston.^{23,25} Unfortunately, Tennant died in a horse riding accident mere days before Children performed these experiments.²³

Most applications of metallic iridium are related to its hardness and inertness. For example, thermocouples of iridium and platinum iridium alloys are used to measure temperatures up to 2000 °C in air. For high temperature crucibles, iridium is used in place of platinum. Because of its hardness, iridium, usually as an alloy with osmium, has been used in mundane applications such as razors and fountain pen tips.²¹

In the present work, iridium was not used in its metallic form, but as an oxide. Despite iridium's inert nature towards oxygen, oxides can be formed easily using various techniques.²⁶ The preparation and properties of iridium oxide will be discussed in the next section.

Shortly coming back to the original purpose of the work by Wollaston and Tennant, besides filling gaps in the periodic table, the challenge of finding a method of platinum refinement was also completed successfully. As a result, W.H Wollaston became the main source of perfectly malleable platinum in England, which brought him considerable wealth. In 1820 Wollaston closed his platinum business: possibly because of the prohibition of platinum sale by Spain, although this is not entirely clear.²⁷ Even after shutting down his business Wollaston did not reveal his methods. Only one month before his death was his procedure made public in his Bakerian Lecture, read at the Royal Society in 1828.^{20,28}

2.2 Iridium oxides

Iridium oxides can roughly be divided into two categories: hydrous and anhydrous. Hydrous oxides are commonly prepared from solution by sol-gel methods,^{29,30} electrodeposition,^{16,18,31} anodic growth^{32,33} and sputtering.³⁴⁻³⁶ Anhydrous oxides can be formed by, among others, melt oxidation,²⁶ sol-gel methods combined with thermal treatments,³⁷ atomic layer deposition³⁸ and pyrolysis.³⁹ An overview of different preparation methods was given by Yao *et al.*²⁶

Different methods lead to different properties, and iridium films are often specified and abbreviated after their method of preparation. Scanning literature on iridium oxide the reader might, therefore, get lost in a jungle of acronyms. Different films are referred to as, among others, SIROF, AIROF, EIROF, HIROF and IROF. In given order these refer to Sputtered, Anodic, Electrodeposited and Hydrated Iridium Oxide Films

The transition of hydrous to anhydrous iridium oxide can be irreversibly achieved by heating above approximately 300 °C.^{40,41} Even metallic iridium can be formed at temperatures exceeding 1100 °C.⁴¹

There are both differences and similarities in the properties of hydrous and anhydrous iridium oxide films. The density of anhydrous IrO₂ is 11.68 g cm⁻³, while that of hydrous films can be as low as 2 g cm⁻³ for AIROFs.⁴⁰ Both materials show electrocatalytic activity towards the oxygen evolution reaction⁴²⁻⁴⁴ (OER), but each with its own advantages and drawbacks. The differences can largely be attributed to the difference in structure.

In contrast with their anhydrous counterpart, hydrated films have an open structure that allows electrolyte to penetrate, with consequences for their electrochemical properties. In addition to iridium sites on the surface, those in the interior of the film are accessible for electrochemical reactions, leading to a large electrochemically active area. Therefore, Burke *et al.* described AIROF appropriately as 3d electrocatalysts.³³ The much denser anhydrous films lack this porosity, but show better long term stability, particularly when mixed with titanium dioxide.⁴⁵⁻⁴⁷ For this reason, application of iridium oxide as electrocatalyst has moved more towards anhydrous iridium oxide films supported on titanium oxide.⁴⁸ SIROFs exhibit intermediate properties, with respect to porosity and stability.⁴⁰

In their application as pH sensors hydrous and anhydrous films each display a distinct behaviour, which will be discussed in Sec. 2.5 and in more detail in Ch. 6.

2.3 Hydrous iridium oxide films

2.3.1 Anodic iridium oxide films

Early work on hydrated iridium oxide films focused on AIROFs, commonly formed by potential cycling iridium electrodes in acid. Like on other noble metals, (*e.g.* Au, Rh, Ru, Pt, Au) hydrous oxides can be formed on iridium under anodic conditions.^{32,49-54} Under galvano- and potentiostatic conditions film growth is inhibited by dissolution, but thick films can be obtained by potential cycling in acid solution.⁵⁵ The growth of the oxide occurs at the interface between the oxide and the parent metal.^{55,56} Pickup *et al.* proposed a growth model where a dense oxide is formed initially, which gets partly hydrated upon further oxidation. During a cathodic scan the dense oxide is reduced back to the metal, leaving behind only the hydrous part.⁵⁶ By potential cycling this process is repeated, essentially building the

hydrous oxide from the base up. This concept will come back in Sec. 6.4.3, when the pH properties of EIROF are discussed. The maximum thickness of hydrous films seems to be limited by a decrease in hydration at greater depth.⁴⁰

Besides scientific interest, HIROFs have been studied for practical application, such as: electrocatalysts,^{33,42} chemical sensors,^{57,58} neurostimulators^{59,60} and supercapacitors.^{55,61}

For obvious reasons metallic iridium is needed as the substrate to form AIROFs. However, with 83 more abundant elements, iridium is a rare and costly element.^{62,63} Fully converting iridium thin films on foreign substrates would lower the iridium needed and partially reduce this problem. However, in 1987 Yoshino *et al.* presented a method to directly electrodeposit iridium oxide films (EIROF) on different substrates.³¹ Two years later an optimised procedure was published by Yamanaka.¹⁶ Electrodeposition will be discussed in some detail in the next section.

2.3.2 Electrodeposited iridium oxide films

Electrodeposition of iridium oxide films offers a flexibility in substrate choice that is lacking for AIROF preparation. More specifically it allows for the formation of HIROFs on transparent substrates, such as indium tin oxide (ITO). This led to research efforts into the use of iridium oxide in electrochromic displays,¹⁶ potentially in conjunction with WO_3 . HIROFs switch from colourless transparent to dark blue upon oxidation.^{31,64-67} WO_3 shows similar behaviour but in the opposite direction.⁶⁸ High contrast devices could therefore be created by coating one electrode with IrO_2 and the other with WO_3 .^{68,69}

Interest in iridium oxide for electrochromic applications has declined in favour of cheaper materials such as polyaniline, but Yamanaka's method and variations thereof remain the most common means for preparing EIROFs.^{16-18,70} Details on the method can be found in the experimental chapter. Alternative methods can also be found.^{31,71}

Although Yamanaka's method has been used for many years, there is no consensus on the actual species involved in the deposition. The role of all the solution constituents has not received much attention either. In the original publication an iridium oxalato complex was put forward as the active component.¹⁶ Oxalate was added to improve stability of the solution. Anodic deposition was proposed to proceed through the oxidation of oxalato complexes under formation of CO_2 . Later work by Elsen *et al.* showed oxalate is not required to form stable and active solutions.^{18,72}

Instead a loose polymeric network of hydrolysed iridium was suggested as the source of iridium oxide. The precipitation of hydrous oxides that occurs at neutral conditions favours this hypothesis.⁷³

The colour of the deposition solutions, deep blue to purple, is evidence of the presence of multinuclear iridium oxyhydroxides.^{74,75} The size of these species can, however, vary from dimers to nanoparticles.^{73,76} The synthesis of iridium oxide nanoparticles has been performed in solutions very similar to the one described by Yamanaka.^{73,76} The formation of nanoparticles will be further discussed in Ch. 5.

2.4 Colloidal iridium oxide

The formation of colloidal iridium oxide was described as early as 1908 by Wöhler *et al.*⁷⁷ Desideri and Pantani proposed colloidal matter as an explanation for their spectrophotometric results on alkaline iridium solutions.⁷⁸ In both cases a blue colour was associated with colloidal matter.

This blue colour originates from an absorption band at 580 nm. Castillo-Blum *et al.* showed this band is indeed associated with multinuclear iridium oxyhydroxide complexes.⁷⁵ Distinguishing dimers from polymeric complexes or hydrous oxide particles is not trivial, since all – even HIROFs – exhibit a similar absorption around 580 nm.^{29,67,73,75,76,79} However, the presence of a tail on the 580 nm extending to larger wavelengths has been related to scattering by particulate matter.⁷⁶

Harriman *et al.* showed how hydrated iridium oxide colloids can be prepared by forced hydrolysis of K_2IrCl_6 in presence of air.⁷³ Under deaerated conditions transparent suspensions of colloidal iridium were formed, which turned blue upon aeration. Suspensions were obtained using citric acid as the stabilising agent. The initial particle size ranged from 1 to 4 nm, which aggregated to form stable colloids around 100 nm in diameter. The formation of nanoparticles has since been shown under various conditions.^{29,44,58,76,80,81}

With three carboxyl groups, citric acid induces aggregation by bridging between particles, Fig. 2.1b.⁷⁶ Hoertz *et al.* showed that aggregation can be inhibited by using malonic and succinic acid, Fig 2.1c and d, which have only two carboxyl groups.⁷⁶

In a recent work by Zhao *et al.* alkaline solutions of K_2IrCl_6 were heated for 20 min at 90 °C and then treated with HNO_3 . When this last step was performed at 0 °C stable colloidal solutions of iridium were formed, in absence of any stabiliser.²⁹

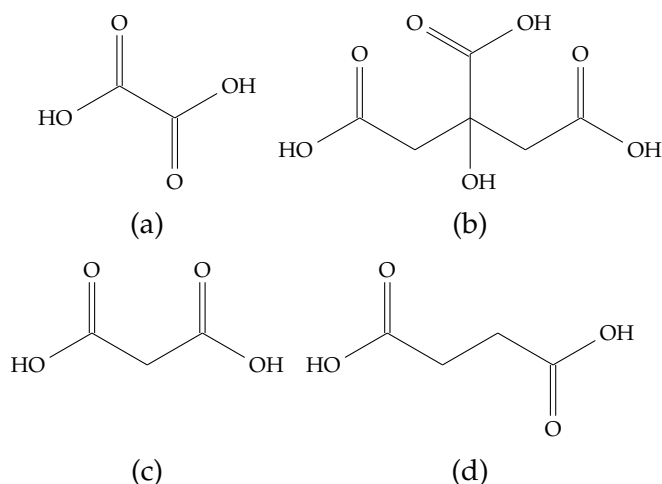


Figure 2.1: Structures of (a) oxalic, (b) citric, (c) malonic and (d) succinic acid

An elegant application of iridium oxide was presented by Kwon *et al.*, who showed how the excellent electrocatalytic properties of hydrous iridium oxide particles can be exploited to measure single particle diffusion.^{81,82} In these experiments a boron doped diamond (BDD) ultramicroelectrode was placed in a dilute suspension of iridium oxide nanoparticles. The electrode potential was then adjusted to within the oxygen evolution regime. Owing to the passive nature of BDD towards oxygen evolution a current can only be observed when one or more iridium oxide particles are adsorbed. Current steps could therefore be related to the diffusion of particles to the electrode.^{81,82}

2.5 pH sensing

2.5.1 General

For common pH measurements glass electrodes do an excellent job, but situations exist where they are less suitable, owing to chemical or practical issues. The analyte might be too corrosive towards glass (*e.g.* strongly alkaline and HF solutions), or the measurement volume too small (*e.g.* a living cell). Alternative pH sensors that are more chemically resistant or more easily miniaturised would then be required. Fortunately, several options exist, based on different physical changes with pH.

In most laboratories one can find pH paper that can be used to get a quick insight in solution pH, simply by looking at colour changes. Colorimetric

pH sensors are based on the same principle. One or more pH sensitive materials can be immobilised on a substrate, or the tip of an optical probe, which can be used to detect pH by measuring reflection, transmission, or luminescence.^{83–85}

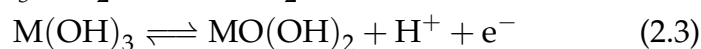
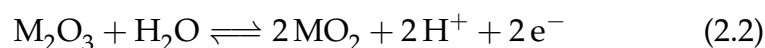
A very different approach is used in pH sensors based on ion sensitive field effect transistors (ISFET).^{86,87} These devices make use of the dependence of surface potential on pH and the physical properties of the semiconductor-electrolyte interface. An example of such a device, based on a ZnO wire, was presented by Heo *et al.*⁸⁷

Since this thesis work aimed at measuring local pH on rotating disc electrodes ISFET sensors were not considered. Colorimetric sensing might be possible, if the insulating area around the electrode material of an RDE is coated with a pH indicator. Instead, however, thin film potentiometric sensors in combination with rotating ring-disc electrodes were chosen for the experiments in this thesis. These sensors and their application will form the topics of the next two sections.

2.5.2 Metal oxide pH sensors

Unlike semiconductor pH sensors those based on conducting materials can be used in a direct potentiometric fashion. The experimental setup, therefore, only requires a reference and sensing electrode in combination with a voltmeter.

Two types of sensing systems can be identified: those based on an equilibrium between a metal and its oxide, Eq. 2.1, and those based on an equilibrium between two oxides of the same metal in different oxidation states, Eq. 2.2 and 2.3.⁸⁸



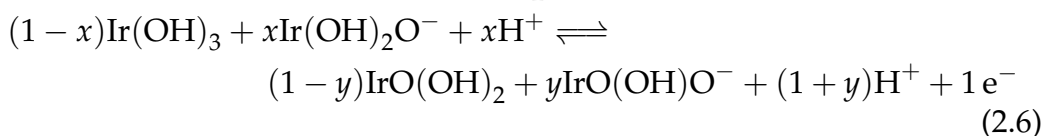
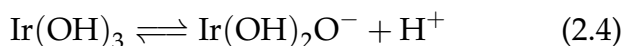
Sensors based on antimony or bismuth are of the first type.⁸⁸ Out of these two antimony pH electrodes are most widely used, particularly in medical applications.^{88,89} Disadvantages of antimony electrodes are that they are influenced by stirring and the chemical environment.⁹⁰ Also, reproducible sensors require highly crystalline antimony.⁹¹ Instead of the simple reaction shown in Eq. 2.1 it has been found that local corrosion cells play an important role in the sensing mechanism.⁸⁸

Fog *et al.* studied an extensive list of compounds for pH sensing: TiO_2 , RuO_2 , Ta_2O_5 , SnO_2 , IrO_2 , OsO_2 and PtO_2 .⁹² However, positive results from the literature and preliminary tests, in combination with facile electrodeposition (Sec. 2.3.2) made iridium oxide stand out as the most suitable material for the RRDE application.^{19,57,72,93–95}

Bismuth sensors were initially considered for the present experiments, after the work by Albery *et al.*⁹ However, bismuth was replaced with iridium oxide after a preliminary study with both materials. Iridium oxide pH sensors can be of the metal/oxide and the mixed oxide type, but only the latter was used in the present work.⁸⁸

As mentioned in Sec.2.2, the anhydrous and hydrous forms of iridium oxide differ in properties. This clearly comes to expression in their pH sensing behaviour. Anhydrous iridium oxide displays a classic Nernstian response (1 electron per proton) of 60 mV.^{26,37} In contrast, hydrous films exhibit a response greater than 60 mV, up to 90 mV.^{18,19}

Explanations for this 'super-Nernstian' behaviour have been sought in the acid base properties of the two oxides involved.^{19,57,96} According to Eq. 2.2 and 2.3 both hydrous and anhydrous materials should exhibit a 60 mV response.⁹⁶ However, rewriting Eq. 2.3 to include the acid base equilibria in Eq. 2.4 and 2.5, results in Eq. 2.6. According to this reaction equation the pH response depends on the relative acidity of the two oxides involved.



Considering the increased acidity with oxidation state of solution complexes and oxide surfaces, a response in excess of 60 mV would be expected.^{97,98} In this interpretation the response is merely higher than 60 mV, but in agreement with the Nernst equation, nonetheless the quotation marks will no longer be used. Further discussion of this topic can be found in Ch. 6.

In electrochemical experiments a background electrolyte is generally required. It is thus important that the pH sensor used is not sensitive to inert ions such as the alkali metal ions. Marzouk *et al.* found that EIROF are not influenced by Li^+ , Na^+ , K^+ , Mg^{2+} and Ca^{2+} ⁹⁹

Iridium oxide films are redox active themselves and might therefore interact with other redox species in solution. Olthuis *et al.* showed that in presence of oxygen AIROF show a slow drift (hours) towards the onset potential of oxygen reduction. More important to the relatively quick measurements required for the present work, are the finding by Carroll *et al.*. They found a complete blocking of the pH response of EIROF by hexacyanoferrate. Similar results were obtained for anhydrous iridium oxide by Fog *et al.*, who tested the influence of several compounds and ions on the pH response of various of pH sensing materials. H_2O_2 , Cl^- and K^+ were shown not to interfere. Other factors, such as storage medium, thickness and average oxidation state, can have an influence on the response of hydrous layers as well.^{18,57}

Zhang *et al.* applied AIROFs for local pH measurements in calcium phosphate electrodeposition.¹⁰⁰ The working electrode used in these experiments consisted of a grade 5 titanium disc, prepared with holes to fit iridium wires. AIROFs were formed on the tip of the wires, after which they could be used to monitor the near surface pH during deposition experiments.

Electrodeposition facilitates the formation of iridium oxide on substrates of various size and shapes. This has led to interesting studies, such as that by Carroll *et al.*,¹⁰¹ who presented a self calibrating EIROF based pH sensor in lab on a chip configuration. A pattern of micrometre sized gold electrodes was deposited on a silicon wafer, using standard lithographic techniques. Next, iridium oxide was electrodeposited on the gold electrodes to form an array of pH sensors. Potential conditioning was proven to be an effective means of calibrating this system. The combination of a multitude of parallel sensors and the possibility of *in situ* calibration, facilitates the use of such systems for long term pH monitoring.

2.6 RRDE – pH measurements

Ever since the publication of the seminal book Physicochemical hydrodynamics by Veniamin Levich, rotating electrodes have become a common tool in electrochemical laboratories. A rotating disc in a Newtonian liquid induces a well defined hydrodynamic flow, which can be used to control mass transport towards the disc's surface, Fig. 2.2. When an electrode is placed at the centre of the disc, a powerful tool is created for studying physical properties of electroactive substances (*e.g.* diffusion constants) and the reactions they undergo.

Placing a second electrode in the form of a concentric ring around the

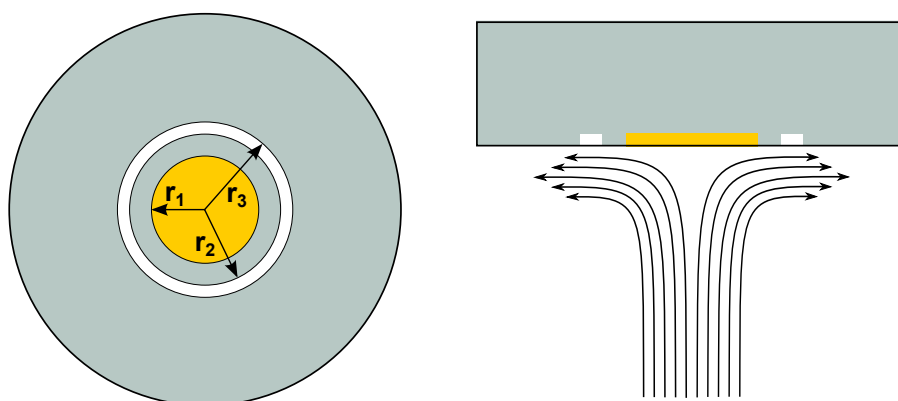


Figure 2.2: Schematic of a rotating ring-disc electrode (RRDE) and the hydrodynamic flow near an R(R)DE.

disc expands the rotating electrode to a rotating ring-disc electrode, Fig. 2.2. Most commonly this setup is used as a generator collector system, where the ring is used as an amperometric detector for species generated on the disc. Alternatively, the consumption of electroactive species can be detected in shielding experiments, in which the same reaction is performed on the disc and ring, but where the ring is kept under limiting current conditions and the disc potential is scanned. The reduced flux to the ring of the species under study, induced by consumption on the disc, is measured.

The foundation of the RRDE pH experiments described in the present chapter was found in an extensive series of papers on RRDE measurements by John Albery and co-workers, published between 1966¹⁰ and 1989.¹⁵ The last four papers of this series deal with the use of the RRDE in a potentiometric mode to allow *in situ* pH measurements during electrochemical experiments.^{9,13-15}

For this purpose the ring electrode was covered with a pH sensitive material, such as bismuth,^{9,13} thionine^{14,15} or in the present case iridium oxide. Changes in the ocp of the ring can then be related to changes in proton or hydroxide concentration near the surface.

Albery and co-workers used water oxidation and reduction as the test reactions.^{9,13} Since protons and hydroxide ions are respectively formed in these processes, local variations in pH occur, which were detected on the ring. The main interest in their work was detecting small pH changes, far below those expected for zinc oxide deposition. A work that is more related to the application for this thesis was published by Hessami *et al.*, who used

a RRDE for pH measurements with a platinum ring in the presence of hydrogen (RHE). With this system the electrochemical deposition of iron, nickel and iron-nickel oxides was studied.

RRDE measurements have several advantages over the use of a micro pH electrode. Under regular experimental conditions the diffusion layer thickness is in the order of microns*. Bringing a probe within such distance from the surface, would influence the measurements by disturbing the hydrodynamic flow and thus the mass transport. In addition, the concentration gradients perpendicular to the surface are steeper than those parallel to the surface,¹⁰² allowing more space between the disc and ring, than disc and probe. Finally, the experimental requirements are less demanding than for using microprobes, in particular taking into account the fact that the RRDE is already a common tool in electrochemical laboratories.

2.7 Zinc oxide

Throughout history zinc oxide has been used as a white pigment in, among others, paints, cosmetics and paper.⁶² Zinc oxide is a wide band gap semiconductor ($E_g = 3.37$ eV) and is considered non toxic, which has led to its use in sun screens.^{62,103} More technologically advanced applications have emerged as well. In addition to a wide band gap, ZnO has a high electron mobility and large exciton binding energy (60 meV),¹⁰³ making it an interesting material for opto-electronic applications such as, conductive windows,^{2,104} solar cells,^{105,106} LEDs,¹⁰⁷⁻¹⁰⁹ laser^{110,111} and transistors.^{112,113} Yet other applications are found in chemical sensing,^{87,114,115}

In this work, focus was on forming thin films of ZnO rods with diameters in the order of tens of nm, for application in, among others, white LEDs. Thin films can be prepared using a wide variety of methods. Vacuum and high temperature methods, like (metalorganic) chemical vapour deposition (CVD), sputtering, atomic layer deposition are commonly used. CVD is well suited to prepare aligned rods and wires.¹¹⁶⁻¹¹⁸ This technique has the advantage of allowing standard lithographic techniques to pattern substrates for directed growth. Patterning can be achieved either by masking parts of the substrate during growth or by patterning catalysts particles from which the rods grow (vapour liquid solid method).^{116,117} Also, doping of the ZnO with foreign elements is readily achieved. The high temperature that is

* $\delta = 1.61D^{1/3}\omega^{-1/2}\nu^{1/6}$, with $D = 1 \times 10^{-5}$ cm² s⁻¹ and $\nu = 0.01$ cm² s⁻¹ the diffusion layer thickness δ is 7 and 21 μ m for a rotation rate of 300 and 3000 rpm, respectively.

usually required ($\sim 900^\circ\text{C}$) is a disadvantage, since it restricts the substrate choice.¹¹⁶

Alternatively, wet chemical techniques, such as chemical bath deposition (CBD), hydrothermal growth and electrodeposition can be used. In these methods water is the most common solvent and reaction temperatures are generally below 100°C , lifting the demands on thermal resistance of the substrates. Somewhat higher temperatures up to 200°C are used under true hydrothermal conditions or using organic solvents.^{119–121}

Arguably the simplest deposition method is CBD as described by Vaysieres,¹²² where ZnO films are prepared by placing a substrate into a heated (90°C) solution of hexamine and $\text{Zn}(\text{NO}_3)_2$ for 1 to 10 hours.¹²² Although this method is simple, others such as electrodeposition are more versatile as will be discussed below.

The habit of forming rods is related to the ZnO crystal structure. Cubic forms exist (zincblende and rocksalt), but far more common is the hexagonally close packed wurtzite structure. Wurtzite ZnO can be described as an alternating stacking of hexagonally close packed oxygen and zinc planes, or as a hexagonal stacking of tetrahedral units of zinc coordinated by four oxygen atoms, Fig 2.3.

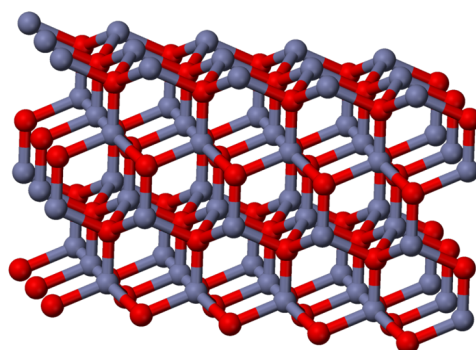


Figure 2.3: Wurtzite structure of zinc oxide¹²³

The non-centrosymmetric nature of wurtzite has important consequences for the growth habit of ZnO. Crystal growth is fastest in the zinc terminated $\{1000\}$ direction and slowest in the oxygen terminated $\{\bar{1}000\}$ direction. This rate difference has been ascribed to the interaction of zincate ($[\text{Zn}(\text{OH})_4]^{2-}$) with the solid. Landing on top of the zinc plane a zincate ion can interact simultaneously with 3 zinc atoms on the surface. In contrast rearrangements

or substitutions are necessary for zincate to bond to the oxygen terminated plane.

The intermediate growth rate in the $\{01\bar{1}0\}$ and $\{2\bar{1}\bar{1}0\}$ direction leads to the facile formation of rodshaped crystals. Other interesting consequences of the crystal structure are piezoelectric properties and the existence of a dipole along the c -axis in ZnO rods.^{124,125} Yang *et al.* triggered a research boost into zinc oxide rods by discovering their room temperature lasing properties.¹¹⁰

2.7.1 Solution chemistry

The solution chemistry of zinc is extensive. Fig. 2.4a shows a room temperature speciation diagram of zinc in aqueous solution taking into account water, hydroxide and chloride complexes (0.1 M Cl^- assumed). In Fig. 2.4b the speciation in the same solution is shown for a temperature of 80 °C, the temperature used in the deposition experiment in Ch. 8. The thermodynamic data used to calculate these diagrams were taken from Goux *et al.*⁴

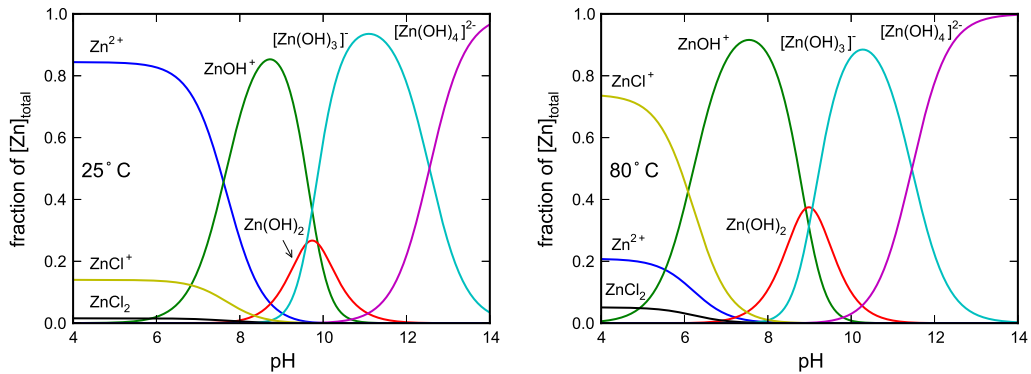


Figure 2.4: Speciation of ZnO in 0.1 M KCl at (a) 25 °C and (b) 80 °C.

By summing up the total concentration of zinc species at each pH the solubility of ZnO, was determined, as a function of pH. A similar calculation was then made for Zn(OH)_2 to allow comparing their relative stability at different pH. The results of these calculations made for 25 °C and 80 °C are summarised in Fig. 2.5.

Fig. 2.5 illustrates the strong pH dependence of the solubility of both ZnO and Zn(OH)_2 , spanning 6 orders of magnitude. Additionally, with increasing temperature the solubility curve shifts to lower pH. Consequently,

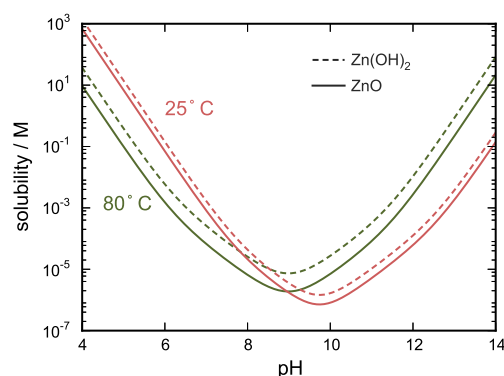


Figure 2.5: Solubility of ZnO and Zn(OH)₂ in 0.1 M KCl at 25 °C and 80 °C.

the solubility on the acidic side of the curve is reduced. Finally, ZnO is shown to be the more stable phase under all conditions represented by the figure.

2.7.2 ZnO electrodeposition

As discussed in the previous section the solubility of ZnO is strongly pH dependent, spanning several orders of magnitude. This property can be used to deposit ZnO electrochemically. The two most commonly used electrodeposition methods are based on nitrate and oxygen reduction in unbuffered near neutral solutions containing a zinc salt.^{1,2,5} Both reactions increase the near surface pH by releasing hydroxide ions and can thereby create a suitable environment for ZnO to precipitate onto the electrode. A less common, but effective alternative to the above mentioned reactions, is the reduction of hydrogen peroxide.⁶ Since, the deposition process itself is essentially a chemical precipitation reaction, it is sometimes referred to an electroprecipitation. However, throughout this work, the term electrodeposition will be used.

Taking into account the amphoteric nature of ZnO an approach from high pH, could be considered as well. Limmer *et al.* showed that proton release during ascorbate oxidation can indeed be used to deposit ZnO from alkaline solutions.³

Goux *et al.* performed potentiostatic deposition experiments from 22 °C to 89 °C on fluorine doped SnO₂ (FTO), using oxygen reduction. Below 34 °C the electrode was passivated by the deposit, which was attributed to the formation of amorphous Zn(OH)₂. At intermediate temperatures the

current traversed a minimum and a maximum before reaching a stable value. The minimum persisted for a shorter time with increasing temperature until it disappeared between 50 and 60 °C.⁴

According to Fig. 2.5 the formation of zinc hydroxide must be related to reaction kinetics, since ZnO is thermodynamically favoured even at room temperature. This was confirmed by Pauporte and Jirka, who showed that the low temperature insulating film can be slowly converted to ZnO by vigorously bubbling the electrolyte with oxygen.¹²⁶ Hence, room temperature growth is possible, but deposition at elevated temperature is still favourable with respect to time and morphology control.

Despite the improvement compared with chemical methods the substrate is still an important factor in ZnO deposition. Silicon shows little affinity towards ZnO deposition, while GaN facilitates the formation of highly aligned rods.¹²⁷⁻¹²⁹ Deposits on FTO can be tuned from very dense to free standing rods by an electrochemical pretreatment.^{5,130} Alternatively substrates can be seeded with ZnO to improve the deposits.¹³¹

Both for chemical and electrochemical growth specific adsorption can be used to control the morphology of ZnO.¹³²⁻¹³⁴ Elias *et al.* studied the influence of the anion in electrodeposition and found that the aspect ratio of the rods decreased in the order acetate, sulfate and chloride.¹³⁵ In a related study, the aspect ratio was shown to go through a maximum near 1 M for Cl⁻.^{136,137} Finally, high zinc concentrations lead to more smooth deposits, whereas rod formation is favoured at low concentrations.

3 Theory

3.1 Electrochemical techniques

3.1.1 Cyclic voltammetry

Cyclic voltammetry (CV) is an electrochemical technique where the potential on the working electrode is scanned linearly back and forth between predefined limits. The resulting current on the working electrode is measured as a function of the applied potential. Fig. 3.1a shows a typical potential input in CV.

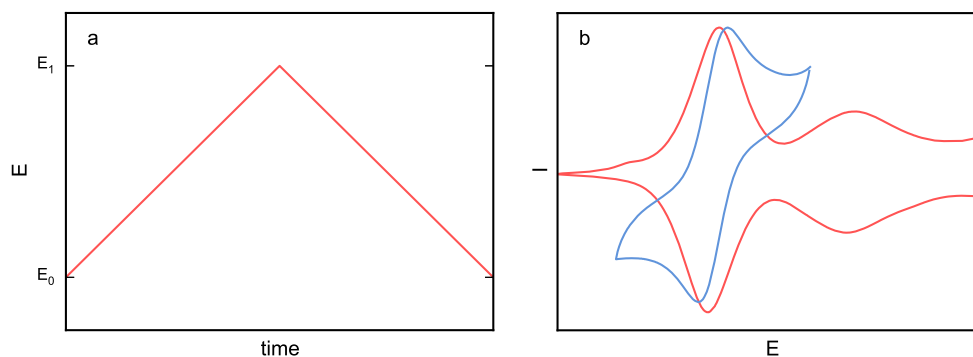


Figure 3.1: (a) Potential in time profile for cyclic voltammetry (b) (—) Cyclic voltammetry of $[\text{IrCl}_6]^{2-}/[\text{IrCl}_6]^{3-}$ and (—) a hydrated iridium oxide film.

CV can be used for different purposes. In Ch. 5 CV was used as an analytical technique to study solutions and in Ch. 6 and 7 it was used to prepare iridium oxide films by electrodeposition. CV is a convenient technique to get a qualitative overview of the electrochemical behaviour of systems, such as reversibility, the existence of coupled reactions, number

of electrons involved and the distinction of surface confined and solution reactions. However, it is not restricted to such use and quantitative data with respect to reaction kinetics and mass transport can also be obtained.^{138,139}

Voltammetry was employed to measure, both on solution and surface confined species. In the former the shape of the voltammogram is determined by the interplay between kinetics and mass transport. For purely surface confined systems, mass transport is not involved, which results in a different current potential relation. Two examples can be seen in Fig. 3.1b.

The voltammetry of a reversible redox couple confined to the electrode surface is characterised by a linear relation between the peak currents and the scan rate. In contrast, solution redox couples exhibit a linear relation with the square root of the sweep rate, owing to diffusion.

In the simplest model for a redox active surface film, a monolayer of reversible non-interacting redox couples is considered. In this model Langmuir adsorption isotherms can be combined with the Nernst equation to derive an analytical expression for the current potential relation.¹³⁸

However, surface confined systems, like the IrO₂ films studied, do not always obey Langmuir conditions. Many factors can play a role here. Interactions between the centres is likely, since we are dealing with charging and discharging of neighbouring species. For such systems alternative isotherms could be applied, for example the Frumkin isotherm.^{140,141} Variations in the chemical structure of the film can result in a distribution of standard potentials, also leading to a broadening of the CV peaks.¹⁴² An interesting example of the strength of the interactions between redox centres is presented in Sec. 6.5 of this thesis (Paper IV). A comprehensive overview of models for non-ideal surface confined systems, was given by Honeychurch *et al.*^{142,143}

Even for surface confined systems diffusion can play a role, when solution species are involved in for example charge compensation in the film. For the hydrous iridium oxide system, the redox transitions are accompanied by proton and hydroxide transport, which can lead to diffusion limitations, in particular at high sweep rates.¹⁴⁴⁻¹⁴⁶

An important issue with surface confined systems is the way the CV is measured. Many modern potentiostats apply a staircase instead of a real linear sweep. For solution reactions this is not necessarily an issue, because the current response to a staircase approaches that of a linear sweep as the step size is reduced, for $n\Delta E < 0.26$ mV the two are indistinguishable.^{147,148} However, for reversible surface confined systems linear sweep behaviour cannot be obtained by choosing proper step size and sampling delay time.¹⁴⁷

A solution can be to apply a low-pass filter to the input signal. Essentially this smears out the staircase and makes it resemble a linear scan, see Fig. 3.2 and 3.1a. Some potentiostats contain multiple filters with different cutoff frequencies. The right choice depends on the scan and sampling rate: too high a cutoff frequency has little effect on the staircase, Fig. 3.2a, but too low a frequency affects the switching point and creates an offset in the potential, Fig. 3.2c.¹⁴⁷ In the present work, filters were chosen on the basis of comparison with analogue sweeps.

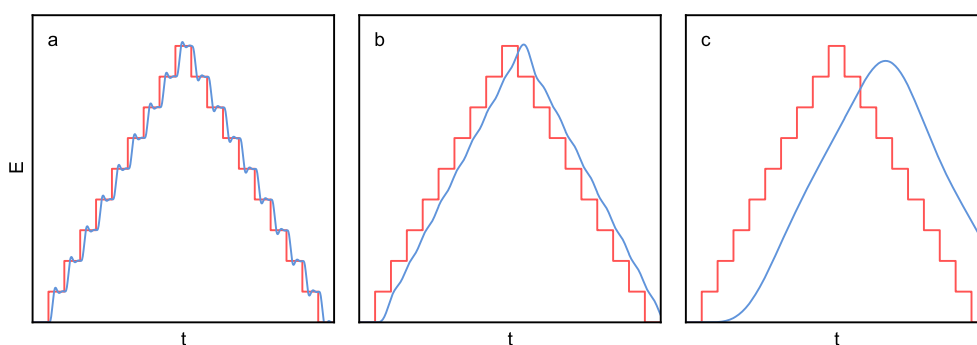


Figure 3.2: Staircase signal filtered through a low pass butterworth filter and the effect of a decreasing cutoff frequency (a) to (c)

3.1.2 Rotating electrodes

Electrode reactions often involve solution species, which need to find their way to the electrode surface to react. During such electrochemical reactions, reactants in the near surface area are consumed, depletion occurs and a diffusion layer forms. Hence, mass transport plays a crucial role in electrochemical experiments. At stationary electrodes the diffusion layer can grow unrestrictedly, slowing down diffusion as the electrode reaction proceeds.¹³⁸ Consequently, natural convection, induced by factors like local thermal fluctuations or vibrations caused by neighbouring equipment, becomes increasingly dominant, hindering a complete description of the mass transport.¹⁴⁹ Near stationary electrode mass transport can therefore only be described at short time scales.

The growth of the diffusion layer can be restricted using convective methods, such as impinging jet or flow cell configurations, and rotating electrodes. The last have been used in the present thesis. The underlying principle of rotating electrodes is the existence of a hydrodynamic boundary

layer at the electrode surface, induced by viscous drag of the electrolyte.^{11,138} Within roughly the first 5 % of this layer mass transport is entirely controlled by diffusion whereas outside this region efficient convective mixing maintains bulk concentrations.¹³⁸ Hence, under rotation a well defined diffusion layer exists at the electrode surface. In addition, the diffusion layer thickness is entirely controlled by physical constants of the system and the rotation rate.

The physical representation of convective flow induced by an infinitely large rotating disc was provided by von Karman and Cochran.^{138,150,151} Provided the hydrodynamic boundary layer thickness is significantly smaller than the dimensions of the electrode, the electrode can reasonably be considered infinitely large.¹³⁸ The hydrodynamics were combined with electrochemistry by Levich, to provide the mass transport equations underlying the rotating (ring-)disc electrode (R(R)DE).¹¹ Later, Albery *et al.* published a seminal series of papers and a monograph, presenting a new derivation of the transport equations for the RRDE system, as well as a wide selection of experimental studies.^{10,149,152} To extract detailed information about reaction kinetics, both analytical^{153–155} and numerical^{156–161} modelling have been used in the literature.

In the present work, the interest lies in the concentration of the reaction products in the near surface region. Surface concentrations and profiles in the disc region can be calculated for products in a similar manner as for reactants.¹³⁸ The next two sections give a summarised derivation of the equations used in Ch. 7 and 8. The procedures used, follow those described by Bard and Faulkner (Ch. 9).¹³⁸ To prevent cluttering the text with definitions, the symbols used in the equations are listed in the list of abbreviations and symbols at the beginning of this thesis.

Surface concentration

The hydrodynamic flow induced by an infinitely large rotating disc was given as a set of three infinite series, describing the flow in the radial, azimuthal and normal direction.^{11,150,151} Owing to the symmetry of the RDE system only the convection normal to the electrode, v_y , needs to be considered.^{7,11,138} In addition, at short distances from the surface only the first term in the series expansion needs to be taken into account, giving,

$$v_y = 0.51\omega^{\frac{3}{2}}\nu^{-\frac{1}{2}}y^2 \quad (3.1)$$

The convective diffusion equation describing mass transport to and from the electrode is,^{11,138,149}

$$v_y \frac{\partial C}{\partial y} = D \frac{\partial^2 C}{\partial y^2} \quad (3.2)$$

For a redox reaction,



the flux J of O and R^- at the surface is defined as,

$$J_O = -D_O \left(\frac{\partial C_O}{\partial y} \right)_{y=0} \quad \text{and} \quad J_R = -D_R \left(\frac{\partial C_R}{\partial y} \right)_{y=0} \quad (3.4)$$

which relate as,

$$qJ_O = -pJ_R \quad (3.5)$$

Hence, the concentration gradient of R at the surface can be written as,

$$\left(\frac{\partial C_R}{\partial y} \right)_{y=0} = -\frac{q D_R}{p D_O} \left(\frac{\partial C_O}{\partial y} \right)_{y=0} \quad (3.6)$$

Rearranging Eq. 3.2 with inclusion of Eq. 3.1 and integrating once results in,¹³⁸

$$C_R^* - C_R^0 = \left(\frac{\partial C_R}{\partial y} \right)_{y=0} \int_0^\infty \exp\left(\frac{-y^3}{3B_R}\right) dy \quad (3.7)$$

with,

$$B_R = \frac{D_R \omega^{-\frac{3}{2}} \nu^{\frac{1}{2}}}{0.51} \quad (3.8)$$

The integral on right hand side of Eq.3.7 can be rewritten as a Gamma function, to obtain,¹³⁸

$$C_R^* - C_R^0 = \left(\frac{\partial C_R}{\partial y} \right)_{y=0} (3B_R)^{\frac{1}{3}} \Gamma(4/3) \quad (3.9)$$

Using Eq. 3.6 this becomes,

$$C_R^* - C_R^0 = -\frac{q D_O}{p D_R} \left(\frac{\partial C_O}{\partial y} \right)_{y=0} (3B_R)^{\frac{1}{3}} \Gamma(4/3) \quad (3.10)$$

For a reduction reaction, the current is related to the surface gradient of the oxidised species as,¹³⁸

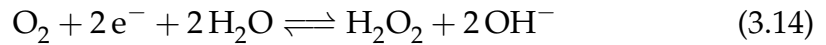
$$\frac{-i}{nFAD_O} = \left(\frac{\partial C_O}{\partial y} \right)_{y=0} \quad (3.11)$$

Hence, with Eq. 3.10 and 3.11 the surface concentration of R can be related to the current,

$$C_R^* - C_R^0 = \frac{q D_O}{p D_R} \frac{i}{nFAD_O} w^{-\frac{1}{2}} \nu^{\frac{1}{6}} D_R^{\frac{1}{3}} \left(\frac{3}{0.51} \right)^{\frac{1}{3}} \Gamma(4/3) \quad (3.12)$$

$$C_R^0 = C_R^* - 1.61 \frac{q}{p} \frac{i}{nFA} D_R^{-\frac{2}{3}} \nu^{\frac{1}{6}} w^{-\frac{1}{2}} \quad (3.13)$$

The reactions of interest for this project are water and oxygen reduction (Ch. 7 and 8), the latter of which can proceed through a 2 or 4 electron process. The relevant reaction equations are,



In all three reactions $\frac{q}{pn} = 1$, which in Eq. 3.13 gives,

$$C_R^0 = C_R^* - 1.61 \frac{\nu^{\frac{1}{6}} i}{FAD_R^{\frac{2}{3}} w^{\frac{1}{2}}} \quad (3.17)$$

Eq. 3.17 shows that C_R^0 changes linearly with the current and depends inversely on the square root of the rotation rate.

Near surface concentration profile

The concentration profile of the produced species near the electrode surface can be calculated from Eq. 3.7 by changing the upper integration limit,¹³⁸

$$C_R(y) - C_R^0 = \left(\frac{\partial C_R}{\partial y} \right)_{y=0} \int_0^y \exp\left(\frac{-y^3}{3B_R}\right) dy \quad (3.18)$$

With Eq. 3.6 and 3.11 the previous equation can be written as,

$$C_R(y) = C_R^0 + \frac{q}{p} \frac{i}{nFAD_R} \int_0^y \exp\left(\frac{-y^3}{3B_R}\right) dy \quad (3.19)$$

As in the previous section, this equation can be simplified for oxygen reduction, using $p = 1$ and $q = n = 4$ or 2 ,

$$C_R(y) = C_R^0 + \frac{i}{FAD_R} \int_0^y \exp\left(\frac{-y^3}{3B_R}\right) dy \quad (3.20)$$

Filling in Eq. 3.17 for C_R^0 gives,

$$C_R(y) = C_R^* - \frac{i}{FA} \left(\frac{1.61\nu^{\frac{1}{6}}}{D_R^{\frac{2}{3}}\omega^{\frac{1}{2}}} - \frac{1}{D_R} \int_0^y \exp\left(\frac{-y^3}{3B_R}\right) dy \right) \quad (3.21)$$

By integrating for a range of y values, concentration profiles of C_R in the diffusion layer can be obtained. The example profiles in Fig. 3.3 show that both the diffusion layer thickness and deviations from the bulk concentrations of O and R increase with decreasing rotation rate.

Rotating ring-disc electrode

Most commonly the ring-disc is used in a generator collector mode, where reaction products, formed electrochemically on the disc, are detected amperometrically on the ring. In the experiments in Paper III, a variation was used, where the ring was allowed to float and its open circuit potential was measured. There is an important difference between the two methods in terms of the mathematical description of the system. While the mass transport equations are the same, the boundary conditions at the ring vary. The surface of an ring-disc electrode can be divided into three regions: disc, gap and ring, see Fig. 2.2. These regions are represented by their radii, r_1 , r_2

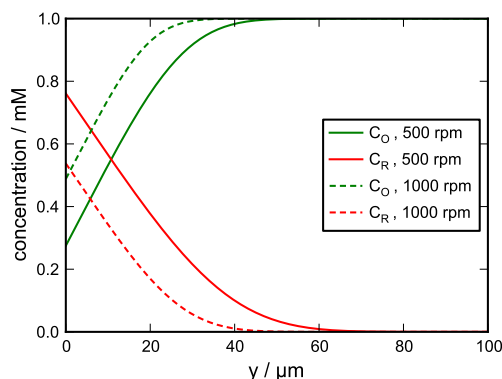


Figure 3.3: Concentration profile of O_2 and OH^- for reduction of O_2 at 1 mA cm^{-2} and rotation at 500 rpm, from a 1 mM O_2 solution at neutral pH.

and r_3 . In amperometric mode these all have different boundary conditions, given below.^{7,138} On the disc,

$$D_R \left(\frac{\partial C_R}{\partial y} \right)_{y=0} = -D_O \left(\frac{\partial C_O}{\partial y} \right)_{y=0} \quad (3.22)$$

$$\left(\frac{\partial C_R}{\partial y} \right)_{y=0} = \frac{-i_D}{nFAD_R} = \frac{-i_D}{\pi r_1^2 nFD_R} \quad (3.23)$$

in the gap,

$$\left(\frac{\partial C_R}{\partial y} \right)_{y=0} = 0 \quad (3.24)$$

at the ring,

$$C_R(y=0) = 0 \quad (3.25)$$

When the ring is used in potentiometric mode it is assumed that only a negligible amount of product is exchanged to bring about the potential change used for detection. Under this assumption, the zero flux condition in the gap region also applies to the ring. Essentially, one cannot speak of a collection efficiency, like for the generator collector system, since no collection takes place. Instead, a detection efficiency can be defined, based on the radial concentration profile at the surface outside the boundaries of the disc.^{9,102}

Albery *et al.* provided the necessary equations.⁹ For radii, r , greater than r_1 the ratio of the concentration difference between bulk and surface in region inside and outside the disc area is given by,⁹

$$\frac{C^0(r) - C^*}{C_D^0 - C^*} = 1 - F \left(\left(\frac{r}{r_1} \right)^3 - 1 \right) \quad (3.26)$$

where the function F is defines as,

$$F(\theta) = \frac{\sqrt{3}}{4\pi} \ln \left\{ \frac{\left(1 + \theta^{\frac{1}{3}}\right)^3}{1 + \theta} \right\} + \frac{3}{2\pi} \arctan \left(\frac{2\theta^{\frac{1}{3}} - 1}{3^{\frac{1}{2}}} \right) + \frac{1}{4} \quad (3.27)$$

The RRDE efficiency under potentiometric conditions is given by,

$$N_D = 1 - \frac{1}{6}F \left[\frac{r_2^3}{r_1} - 1 \right] - \frac{2}{3}F \left[\left(\frac{r_2 + r_3}{2r_1} \right)^3 - 1 \right] - \frac{1}{6}F \left[\left(\frac{r_3}{r_1} \right)^3 - 1 \right] \quad (3.28)$$

3.2 Dynamic light scattering

Dynamic light scattering (DLS) was used in Ch. 5 for analysis of the iridium oxide deposition solutions. Light scattering occurs in media that contain inhomogeneities with respect to refractive index, such as particulate matter or emulsion droplets in a solvent. In dynamic light scattering the scattered intensity is measured as a function of time at a fixed angle.

Due to Brownian motion of the scattering entities the scattered intensity fluctuates in time. By applying an autocorrelation function to the signal a measure of the correlation length can be obtained, which relates to the average diffusion coefficient of the scattering entities. Under the assumption of spherical matter the Stokes-Einstein equation, Eq. 3.29, can then be used to relate the diffusion coefficient to the particle radius.¹⁶²

$$D = \frac{k_B T}{6\pi\eta R_H} \quad (3.29)$$

A drawback of the light scattering techniques is that the scattering intensity is highly sensitive to the dimensions of the scattering particle (volume squared), in the case of a spherical particle there is a R^6 dependence. As a consequence, the radius of polydispersed solutions is biased towards larger particles,¹⁶²

3.3 Electron microscopy and energy dispersive X-ray spectroscopy

Two electron microscopy techniques were used for characterising samples. Scanning and transmission electron microscopy (SEM and TEM, respectively). Furthermore, energy dispersive X-ray spectroscopy (EDX) was used for elemental analysis of surfaces. Since EDX and SEM were done in the same equipment these will be treated in a single section.

3.3.1 SEM & EDX

As can be inferred from the name, SEM involves the scanning of sample surfaces with an electron beam to obtain surface information and construct images.

The acceleration voltage used in SEM typically lies in the range of 1 to 25 kV. When an electron beam hits a surface several physical processes occur, leading to the emission of electrons and X-rays from the sample. Two categories of electrons can be distinguished. First, backscattered electrons: electrons from the beam that found their way back out of the sample after (multiple) scattering events. Second, secondary electrons: electrons from the sample, that gained sufficient kinetic energy due to inelastic scattering of beam electrons to be ejected from the sample.¹⁶³

In practice the only distinction that can be made between electron originating from different process, is by their energy range. Electrons detected at less than 50 eV are considered secondary electrons and everything above backscattered. As the beam voltage is decreased the relative amount of secondary electrons in the signal increases. For the work described in this thesis, only secondary electrons are considered.

As mentioned above, X-rays emission can also be an outcome of the interaction of the beam with the sample. In an inelastic scattering event, an electron from the beam can transfer sufficient energy to an inner core electron to be expelled. This leaves the atom in an excited and ionised state. Relaxation of this state can lead to the expulsion of a second electron (Auger) or to the emission of an X-ray photon, the latter of which are detected in an EDX measurement. Because the X-ray photon is a result of relaxation from core electrons, their energies give information about the elemental nature of the specimen.¹⁶³

3.3.2 TEM

In transmission electron microscopy, the electron beam is passed through the sample and the transmitted beam is detected. Interaction of the electron beam with the specimen, *e.g.* scattering and absorption, is used for imaging. The energy of the electron beam is generally much higher than in SEM. For the TEM measurements performed for this thesis work, a beam voltage of 200 kV was used, which is a factor 20 to 100 higher than what was used for scanning electron microscopy. Since the beam needs to pass through the specimen, the maximum specimen thickness is restricted to roughly 100 nm.

4 Experimental

4.1 Electrochemical equipment

The main body of the project entails electrochemical methods for preparation, characterisation and analysis. Here an overview is given of the setups and equipment used throughout this thesis.

4.1.1 Potentiostats

- EG&G Princeton Applied Research potentiostat/galvanostat model 273A, Corrware
- Gamry Reference 600TM, Gamry Analyst 5.60 Potentiostat/Galvanostat/ZRA
- Autolab, px1000, NOVA 1.7
- Solartron 1287A, Corrware.

4.1.2 Cells and electrode setup

Regular single compartment glass electrochemical cells were used, with single and double walls. The latter were used in experiments performed at elevated temperature, since they allow temperature control using a thermostatic bath. For room temperature experiments both types were used.

Experiments were carried out with different electrode setups. All electrodeposition and voltammetry measurements were done in a conventional three electrode setup with a working, reference and counter electrode. Open circuit potential (ocp) measurements were carried out in a two electrode setup with only a indicator and reference electrode. For the RRDE-pH experiments, the disc, counter and reference electrode were used in a standard

three electrode setup. In addition the ring and reference were connected to the px1000 module to allow ocp measurements on the ring.

4.1.3 Electrodes

Reference All experiments were performed using double junction Ag/AgCl (sat'd KCl) reference electrodes ($E = 197\text{ mV vs NHE}$). The outer junction was always filled with the background electrolyte used in the experiments. The Ag/AgCl electrode was prepared by oxidation of a silver wire in 0.1 M KCl for 30 minutes, under galvanostatic conditions at $\sim 0.4\text{ mA cm}^{-2}$.¹⁶⁴ Prior to the oxidation step, the silver wire was cleaned in 15 M NH_3 and then in 3 M HNO_3 , in between and after it was rinsed with Milli-Q water.¹⁶⁴

Counter A platinum mesh was used as the counter electrode in all electrochemical experiments described in this thesis.

Working Several working/indicator electrodes were used. The RDEs all had a radius of 1.5 mm and were embedded in epoxy (EpoFix, Struers) or PEEK. The electrode materials used were gold, platinum and titanium. The RRDEs were either gold/gold or gold/titanium in epoxy, with a disc radius of 1.5 mm and a ring with an inner and outer radius of 1.8 and 2.5 mm, respectively. For ocp measurements in Ch. 5 a Pt rod was used as the indicator electrode in a two electrode setup. All electrodes will be specified at the appropriate locations in the text.

Before use the working electrodes were polished to a mirror shine on a polishing cloth (DP-DUR, Struers and MD-Chem), with diamond paste (Struers 6, 3, 1 and $0.25\text{ }\mu\text{m}$). After polishing the electrodes were rinsed with Milli-Q water ($18.2\text{ M}\Omega$ Millipore Milli-Q-Academic) and sonicated in Milli-Q water. RRDEs were not sonicated, because of issues with leaking.

4.2 UV-Vis spectroscopy

UV-Vis spectroscopy was measured on a Cary 50 Bio UV-Visible spectrophotometer controlled by the Cary WinUV software, using Hellma Quartz cuvettes with a 10 mm path length.

4.3 Electron microscopy and energy dispersive X-ray spectroscopy

Field Emission Scanning Electron Microscopy (FE-SEM) and energy dispersive X-ray spectroscopy (EDX), was performed on a Leo Ultra 55 FE-SEM,

equipped with an Oxford Inca EDX system. In addition a JEOL JSM-6301F FE-SEM was used for imaging. Throughout this work FE-SEM will be referred to as SEM.

Sample preparation was performed in several ways, depending on the studied material. For measurements on electrodeposited films of both iridium and zinc oxide, the RDE or RRDE was mounted directly in the SEM. While positioning the sample for imaging a low voltage (e.g. 1 kV) was used to prevent charging of insulating parts of the electrode. Once the sample was in position higher voltages could be used. Measurements on surface morphology were generally performed at a working distance of 2 to 4 mm using the in-lens detector. Imaging on chemically grown ZnO was done on the JEOL SEM, at a working distance of 15 mm and an acceleration voltage of 15 kV. The Si or SiC wafers used as substrates were mounted in the microscope on carbon tabs.

Transmission Electron Microscopy (TEM) was carried out on a FEI Tecnai G2, using an acceleration voltage of 200 kV. Samples were prepared on 3 mm alvac steel discs. The discs contained a small hole, with a sufficiently thin edge at which imaging could be performed.

Iridium oxide samples for TEM imaging were prepared in two ways. One was prepared by direct electrodeposition onto the substrate at a constant current of 16 mA cm^{-2} for 2 min. The second was prepared by a simple drop and dry method, where a drop of a dialysed (against Milli-Q) deposition solution was dropped onto the substrate, followed by carefully drying over a hotplate, which was set to 120°C . EDX measurements on these samples were done in the SEM, using a holder for TEM samples.

4.4 Dynamic light scattering

Dynamic light scattering (DLS), was measured on a Malvern Zetasize Nano ZS. The incident beam was a 632.8 nm HeNe laser and the detection angle 173° .

4.5 Iridium oxide deposition

4.5.1 Preparation of the IrO_2 deposition solution

The solution for electrodeposition was prepared according to Yamanaka,¹⁶ however the order of addition of oxalic acid and H_2O_2 was reversed following Marzouk.¹⁷ First, 0.15 g IrCl_4 (Premion 56.77% Ir, Alfa Aesar) was dissolved in 100 ml Milli-Q water and stirred for 30 minutes using a magnetic stirrer. Then, oxalic acid, 0.5 g anhydrous or 0.65 g (Merck, pro analyse),

was added, followed by 10 minutes of stirring before adding 1 ml H₂O₂ (30 %, Fluka traceselect ultra). After another 10 minutes of stirring the pH was slowly raised to 10.5 by stepwise addition of sodium carbonate (Merck, pro analysis). For deposition solutions used in the RRDE-pH experiments, Na₂CO₃ was replaced with K₂CO₃, Ch. 7.

After preparation the solution was aged at room temperature for a minimum of two days, or heat treated. In the heat treatment, the solution was heated to 90 °C for 15 minutes and subsequently cooled down to room temperature in an ice bath.¹⁷ Both procedures were used in the experiments described in this thesis, no difference was noted for depositions from heat treated and non heat treated solutions.

4.5.2 Electrodeposition of iridium oxide

Deposition of iridium oxide by CV was carried out at 1 V s⁻¹ with a stationary electrode. On gold electrodes the potential was cycled 600 times between -500 and 650 mV (vs Ag/AgCl), Ch 6. For depositions on the titanium ring of the RRDEs, the limits were -200 and 750 mV and the number of cycles 300, Ch. 7.

4.6 Zinc oxide deposition

Chemical bath deposition (CBD) of ZnO was done from equimolar solutions of 25 mM hexamine (HMT) and Zn(NO₃)₂ in a beaker covered with a watch glass. A substrate was placed in the solution and heated for up to 2 h at 90 °C. Afterwards the substrate was rinsed with demineralised water and dried in air.

The substrates were silicon wafers, with the exception of one set of experiments where SiC was used. For deposition on gold a 5 nm chromium film was evaporated on the Si using CVD, followed by 50 nm of gold.

Zinc oxide was electrodeposited at 80 °C from oxygen saturated aqueous solutions of 0.1 mM ZnCl₂ and 0.1 M KCl. The electrolyte was heated using a thermostatic bath and double walled electrochemical cell. Oxygen (AGA) was bubbled for a minimum of 20 minutes prior to the deposition experiments. Depositions were performed on gold RDEs at 1000 rpm under galvanostatic conditions.

5 Iridium oxide deposition

In this chapter experimental results related to the electrodeposition of iridium oxide are presented and discussed. The aim is to summarise the work presented in Paper I and place it into a wider context. Therefore, additional results and literature background are given where suitable.

5.1 Introduction

As described in Sec. 2.3.2 various methods exist to electrodeposit iridium oxide. For this thesis work a deposition solution was chosen that was first described by Yamanaka and modified by Marzouk.^{16,17} In literature this solution, or a modification thereof, is the most widely used, but despite being commonly applied not much research has been devoted to the solution itself.

In the original work the active component, during iridium oxide deposition, was proposed to be an iridium oxalato complex.¹⁶ Elsen *et al.* proposed a polymeric network of hydrolysed iridium oxide as the precursor to the iridium oxide films.^{18,72} While working towards the application of iridium oxide for pH measurements, the question of the active component in the deposition solution resulted in new branch in the present project. This work is summarised in the present chapter and published in Paper I.

5.2 Solution preparation

To prepare a deposition solution, first 0.15 g IrCl_4 was dissolved for 30 min under stirring. Next, 1 ml H_2O_2 and 0.5 g anhydrous oxalic acid were added

with 10 minutes stirring in between and after. Then, the pH was raised to 10.5 by adding Na_2CO_3 . Finally, the solution was either kept stirring for 2 days at room temperature or heated at 90°C for 15 minutes and cooled to room temperature in an ice bath.^{16,17}

To gain insight in the events occurring during preparation of the deposition solution, open circuit potential (ocp), UV-Vis and cyclic voltammetry (CV) were measured after each addition. The results of these measurements are summarised in Fig. 5.1

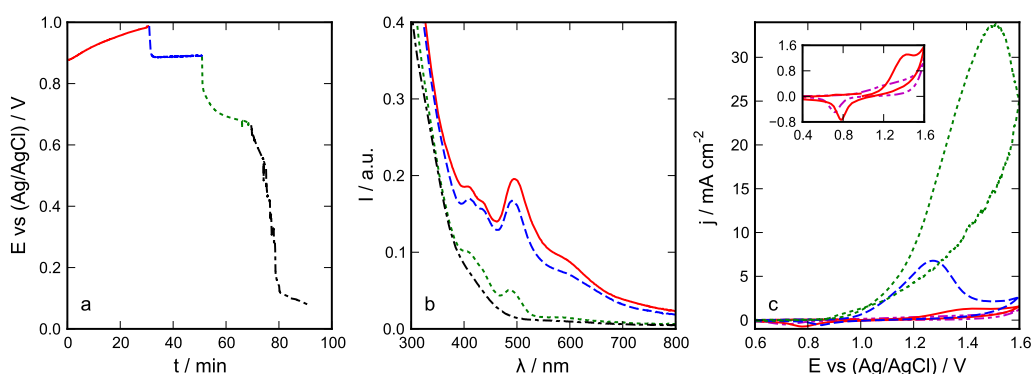


Figure 5.1: (a) ocp, (b) UV-Vis and (c) CV (50 mV/s) of an iridium oxide deposition solution after different steps during its preparation. The lines represent measurements in the solution after addition of NaClO_4 (---), IrCl_4 (—), oxalic acid (— —), hydrogen peroxide (····), and carbonate (— · —). Note that not all lines are present in each subfigure.

The UV-Vis spectrum of the IrCl_4 solution, red line in Fig. 5.1b shows peaks at approximately 413, 433, 491 and 591 nm, indicative of the presence of $[\text{IrCl}_6]^{2-}$.¹⁶⁵ For comparison, a solution of IrCl_4 in concentrated HCl was prepared and monitored with UV-Vis spectroscopy (not shown), the aforementioned peaks became more dominant and after 1 week the spectrum closely resembled that of pure $[\text{IrCl}_6]^{2-}$.¹⁶⁵ Cyclic voltammetry was measured in 0.1 M HCl. Fig. 5.2b shows the resulting scans measured at 10 to 400 mV s^{-1} . The reversible couple centred around 750 mV matches well with the CV of $[\text{IrCl}_6]^{2-}$.¹⁶⁶ In Fig. 5.2a it can be seen that a similar couple around 700 mV is present in the IrCl_4 solution. The concentration of $[\text{IrCl}_6]^{2-}$, calculated from the peak currents fit well with the iridium ratio in the starting material.

Fig. 5.1 indicates that adding oxalic acid induced no major changes in the solution, since only a minor decrease in ocp and UV-Vis intensities was detected, in addition a small pH reduction was observed (2.5 to 1.2–1.4). The effect on the spectrum and ocp could both indicate a reduction from Ir(IV) to Ir(III): the absorbance of Ir(III) species is much weaker than for Ir(IV).¹⁶⁵ This fits with the fact that oxalato ligands Ir(IV) complexes slowly reduce the central metal ion to Ir(III).¹⁶⁷ In the CV a new irreversible couple showed up. If this anodic peak originates from the oxidation of an iridium oxalato complex (maximum 4.5 mM), an unreasonably high diffusion coefficient in the order of $1 \times 10^{-3} \text{ cm}^2 \text{ s}^{-1}$ would be required. A more likely origin is the oxidation of oxalate itself, which, on gold, occurs in this potential range, Fig. 5.3.

Hydrogen peroxide had a pronounced effect in all different measurements. From the ocp and UV-Vis it was clear that a reduction to Ir(III) occurred. This reduction was also reflected in a colour change to pale yellow, indicative of Ir(III) complexes. In the voltammetry the hydrogen peroxide oxidation obfuscated any information related to iridium species.

The role of oxalate is not entirely clear from these experiments, but based on the UV-Vis spectra and CV (Fig. 5.3) it seems unlikely an oxalato complex is crucial for depositing from this solution.

After raising pH to 10.5 with Na_2CO_3 the ocp fell to 70 mV, furthermore the $[\text{IrCl}_6]^{2-}$ intensity in the UV-Vis spectra was quenched entirely, Fig 5.1. At this pH, base hydrolysis occurs, eventually forming $[\text{Ir}(\text{OH})_6]^{2-}$ and in addition, spontaneous reduction to Ir(III) starts. The standard potential of the

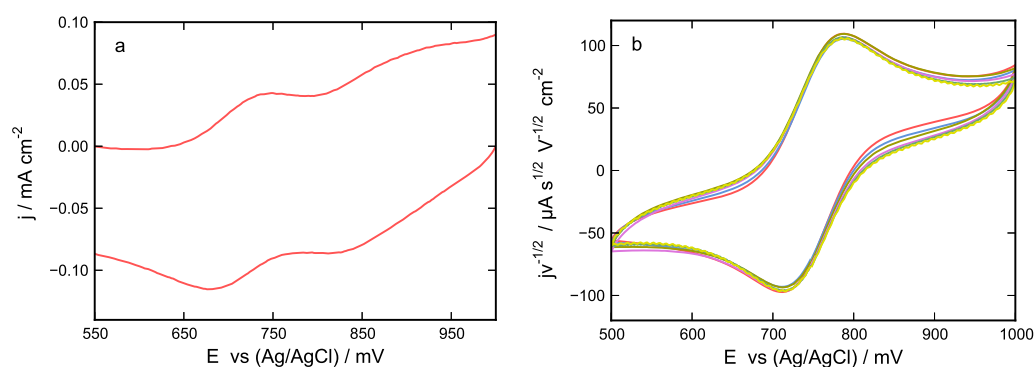


Figure 5.2: Cyclic voltammetry of (a) IrCl_4 at 50 mV s^{-1} and (b) $[\text{IrCl}_6]^{2-}$, scan rate is $10\text{--}400 \text{ mV s}^{-1}$

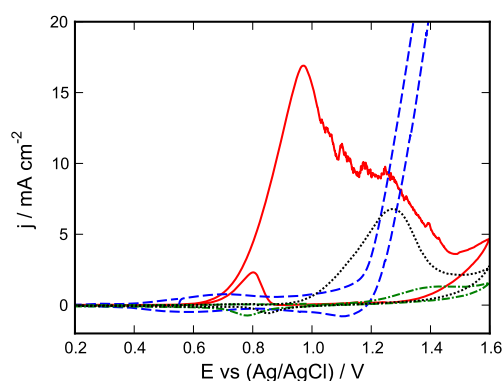


Figure 5.3: Cyclic voltammetry ($v = 50 \text{ mV s}^{-1}$) of oxalate oxidation on (—) gold, (---) IrO_2 , (.....) gold, with IrCl_4 in solution. (-.-) Background cyclic voltammetry on gold without oxalate.

$[\text{Ir}(\text{OH})_6]^{2-/3-}$ redox couple (-0.56 V) is significantly lower than that of the aquo-halo complexes in acidic environment (e.g. $E^\circ = 0.87 \text{ V}$ for $[\text{IrCl}_6]^{2-/3-}$). Therefore, under alkaline conditions H_2O_2 will take the role of an oxidising agent, which is further enhanced by the presence of carbonate.¹⁶⁸ The role of peroxide will be further discussed within the context of the solution development.

5.3 Solution aging

Freshly prepared solutions need to age before they can be used for depositing. During this aging step an absorption at 580 nm develops, as the solutions turn from green/brown to deep blue/purple. Petit and Plichon used the absorbance at 580 nm as a measure to determine whether the solution was ready for deposition.¹⁶⁹ At room temperature aging takes at least two days. However, as mentioned in Sec. 5.2 a heating step was used, which reduced the time required to 15 minutes.¹⁷

The development of a solution at room temperature is illustrated by the UV-Vis spectra in Fig. 5.4a. The blue colouration of the solution coincides with the increasing absorption around 580 nm . It has been described in the literature, that the speed with which the blue colour develops is doubled by the presence of hydrogen peroxide.¹⁷ This indicates, H_2O_2 promotes the formation of Ir(IV) complexes or oxyhydroxides, which are associated with the blue colour⁷³⁻⁷⁵

In time the intensity of the tail on the high wavelength side of this peak

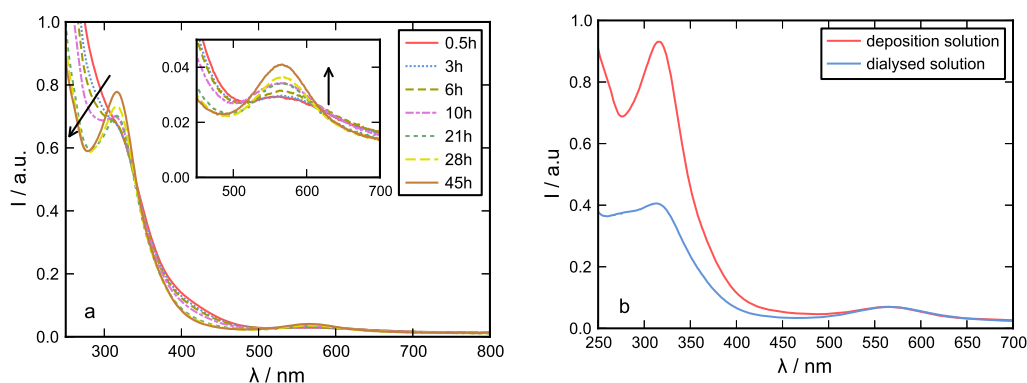


Figure 5.4: (a) UV-Vis spectra of aging deposition solution and (b) deposition solution and dialysed solution

also increased. This tail has been related to scattering by particles, as will be discussed in the next section. Interesting to note is that solutions prepared under nitrogen atmosphere, do not show the absorption at 580 nm and remain yellow brown. No significant differences were observed in the cyclic voltammetry for solutions prepared in presence and absence of oxygen. More details can be found in Paper I

5.4 Iridium oxide nanoparticles

As mentioned in Sec. 2.3.2, the active component in the Yamanaka solution has been assumed an oxalato complex.¹⁶ Elsen *et al.* showed that oxalate is not required to obtain stable deposition solutions and suggested a polymeric network of iridium oxyhydroxide as the active component. This is a reasonable suggestion considering that such hydrous oxides are known to form under neutral and alkaline conditions. An example is the black precipitate that Baur and Plichon observed.⁷¹ Polycondensation of iridium hydroxide complexes can lead to anything from dimers, large polymeric structures and particles. Distinguishing these spectroscopically is not straightforward, since all show a similar characteristic absorption at 580 nm.^{67,73,75,76,79} However, the high wavelength tail on this absorption is indicative of scattering by particles.⁷⁶

The synthesis of iridium oxide nanoparticles was discussed in Sec. 2.4. Comparing methods of nanoparticle synthesis with the preparation of the iridium oxide deposition solution, the presence of nanoparticles in the latter is likely. Both involve alkaline solutions of hydrolysed iridium salts

containing a stabilising agent. Malonic and succinic acid, both similar to oxalic acid, were used by Hoertz *et al.* to stabilise colloidal solutions of particles with sizes around 20 nm.

Experiments to confirm the presence of nanoparticles were undertaken after comparing literature on deposition and nanoparticle synthesis and observing the absorption tail in the UV-Vis spectra, Fig 5.4. Dynamic light scattering (DLS), scanning electron microscopy (SEM) and transmission electron microscopy (TEM) were used for this purpose.

Samples were prepared from the deposition solution as is, either by using a drop and dry method or by electrodeposition. In addition a solution was dialysed against Milli-Q water to remove all dissolved matter. Removal of iridium would inhibit the growth of particles through further condensation of solution species and removal of salts like sodium carbonate lowers the ionic strength, which improves the stability of colloidal systems through electrostatic repulsion.¹⁶²

Dialysis at room temperature led to some precipitation, so the experiments were performed in a refrigerator at 2 °C.⁷⁶ The reduced temperature inhibited aggregation and clear samples of neutral pH were prepared. Owing to osmosis, the samples were diluted approximately once during the dialysis. A quantitative comparison of spectra before and after was therefore not possible. However, it was clear that a lot of absorbing material was removed, since after dialysis the absorbance had decreased by roughly two orders of magnitude.

Fig. 5.4b shows spectra before and after dialysis. For comparison, these spectra were scaled on the 580 nm absorption. Clearly, the peak at 316 nm, associated with $[\text{Ir}(\text{OH})_6]^{2-}$, had decreased relative to the one at 580 nm. The presence of absorbing species after dialysis indicates these were too large to be removed, possibly particles.

DLS was measured on an old, fresh and dialysed solution. In the old solution a polydispersed distribution of particles was detected with diameters from 100 to 500 nm. The fresh solution yielded no measurable scattering intensity. In the dialysed solution a double distribution was found, centred at 20 and 100 nm (Supporting Info Paper I). The number density only shows the peak at 20 nm. The discrepancy between fresh and dialysed samples could be a result from aggregation during the dialysis.

In the work by Harriman,⁷³ nanoparticles in the size of 1 to 4 nm were accompanied by aggregates up to 100 nm in the size range detected in the present experiments. With malonic and succinic acid iridium oxide particles

of 2 nm were formed, with aggregates of 10 to 20 nm.⁷⁶ If the particle size in the present solution is similar, they would be too small to detect in the DLS setup that was used. Therefore, electron microscopy was used for further experiments.

5.5 Electron microscopy

First, SEM imaging was performed on an EIROF, deposited on titanium, and on a sample prepared by drying three drops of the deposition solution on a gold coated silicon wafer. Besides imaging, the elemental contents of the sample were determined by energy dispersive X-ray analysis (EDX).

Fig. 5.5 shows SEM images of an EIROF deposited on a grade 5 titanium electrode (by CV, Ch. 7). The images were taken at a low acceleration voltage of 1 kV, to reduce the penetration depth of the beam and to enhance the surface details. Smooth films were obtained in the electrodeposition process, Fig. 5.5a. At higher magnification, shown in Fig. 5.5b, a degree of roughness is visible that resembles a particulate structure, not present in the underlying substrate.

The titanium substrate was chosen, because in contrast with gold the titanium spectra does not overlap with that of iridium. Fig. 5.6 summarises the EDX results, measured at 15 kV. The amount of oxygen greatly exceeds the amount of iridium, which can be explained by the presence of a titanium oxide.

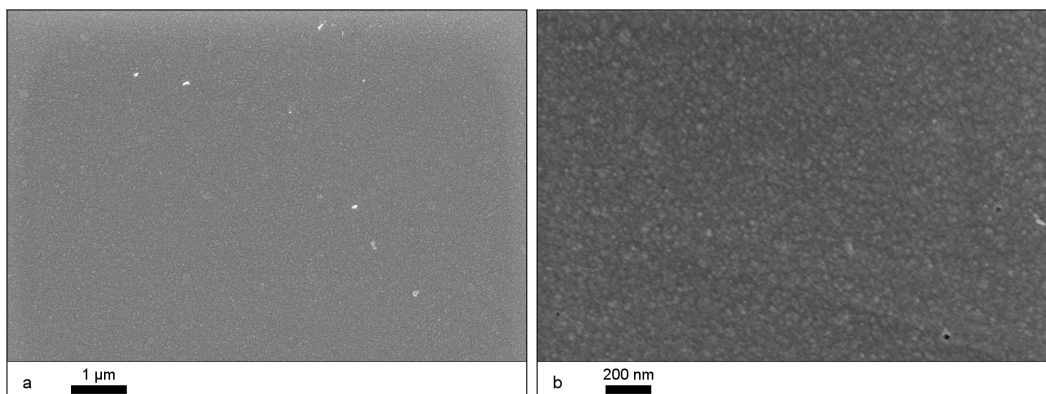


Figure 5.5: SEM images of an EIROF, deposited by CV on titanium (Ch. 7), at two different magnifications.

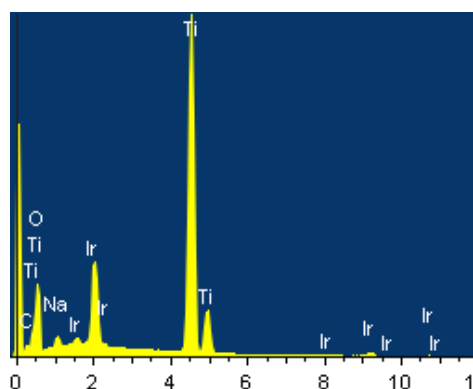


Figure 5.6: EDX spectrum (15 kV) of iridium oxide on titanium

Since SEM did not provide sufficient resolution, TEM was used to obtain images at higher magnification. The substrates used to prepare TEM samples were 3 mm Allvac 718 steel discs with a small hole in the centre. The tapered edge around this hole was used for imaging, as close to the edge the steel was sufficiently transparent. TEM images in Fig 5.7 show that the bare substrates are smooth and featureless.

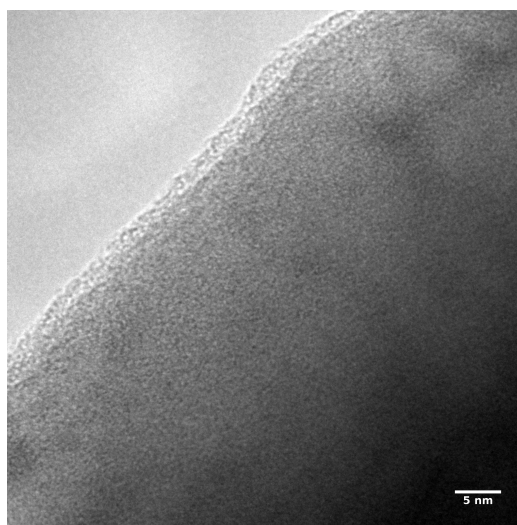


Figure 5.7: TEM images of the Allvac 718, used as the substrate for TEM samples.

Fig. 5.8 and 5.9 show samples containing iridium oxide that were prepared by electrodeposition and from the dialysed solution (Sec. 5.4), respectively. Electrodeposition was done at -16 mA cm^{-2} for 2 minutes. The

sample, used for Fig. 5.9 was prepared by placing a drop of the dialysed solution on the substrate, followed by careful drying over a hotplate, repeated 3 times.

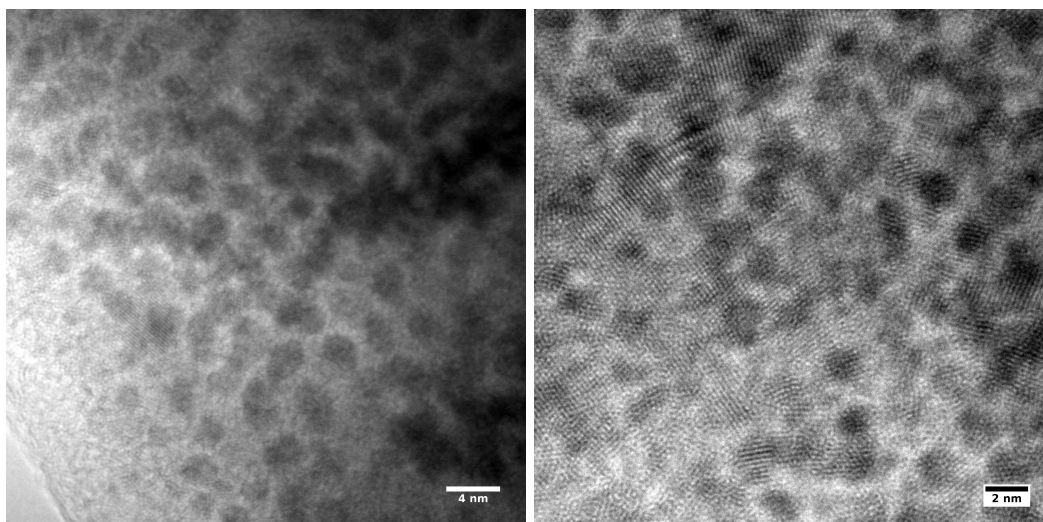


Figure 5.8: TEM images of electrodeposited iridium oxide on Allvac 718, at two magnifications.

Particles with diameters in the order of 2.5 to 3.5 nm were found in both cases. From the lattice fringes in the most clearly separated particles a d-spacing was obtained from 2.22 to 2.26 Å. This is in good agreement with the spacing of 2.24 and 2.26 nm for the (111) and (200) planes of IrO_2 , respectively.^{170,171}

Further confirmation of the chemical nature of the particles observed in TEM was obtained by measuring EDX in the SEM. Although the particles themselves were not visible in SEM, a distribution of iridium was found on the surface of both samples. Since these samples are thin, penetration depth is not an issue and an acceleration voltage of 25 kV was used.

EDX spectra were measured using a 30 and 120 μm aperture. The resulting SEM figures and EDX spectra are shown in Fig. 5.10. Note that the SEM images were enhanced somewhat by adjusting their brightness and contrast. The larger aperture improved the X-ray signal, but also reduced the resolution. However, since the measurements concern an ensemble of particles this was not considered a problem. The yellow arrows in the SEM images indicate the spot of the EDX spectra shown below. For Fig. 5.10b it was attempted to get as close to the edge as possible to reduce

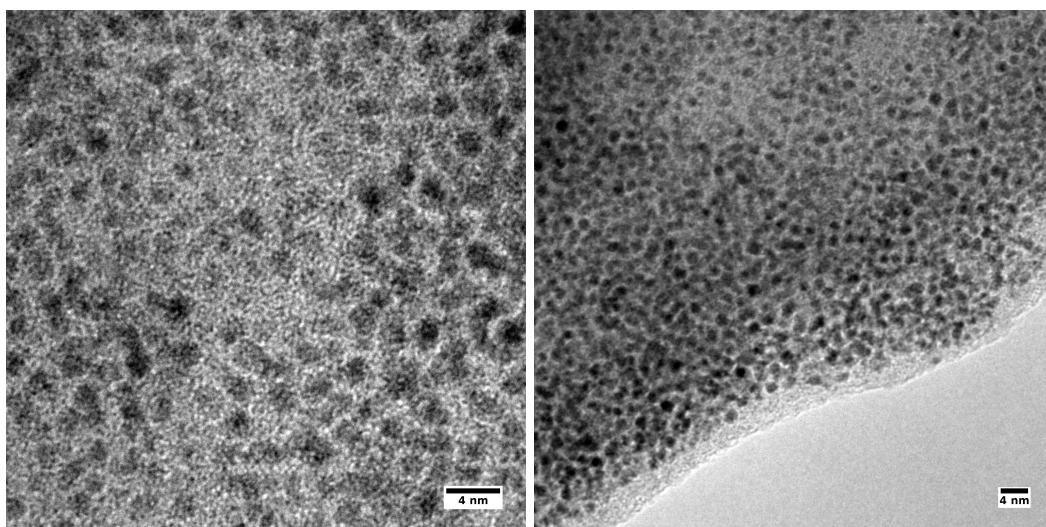


Figure 5.9: TEM images of iridium oxide on Allvac 718 prepared from a dialysed deposition solution, at two magnifications.

the signal from the substrate. Compared with the measurements on the electrodeposited film, the oxygen content is much lower, but still there is a large contribution from the substrate. The EDX spectra agree with those of bare Allvac 718, with the exception of iridium, which is not present in the substrate material.¹⁷²

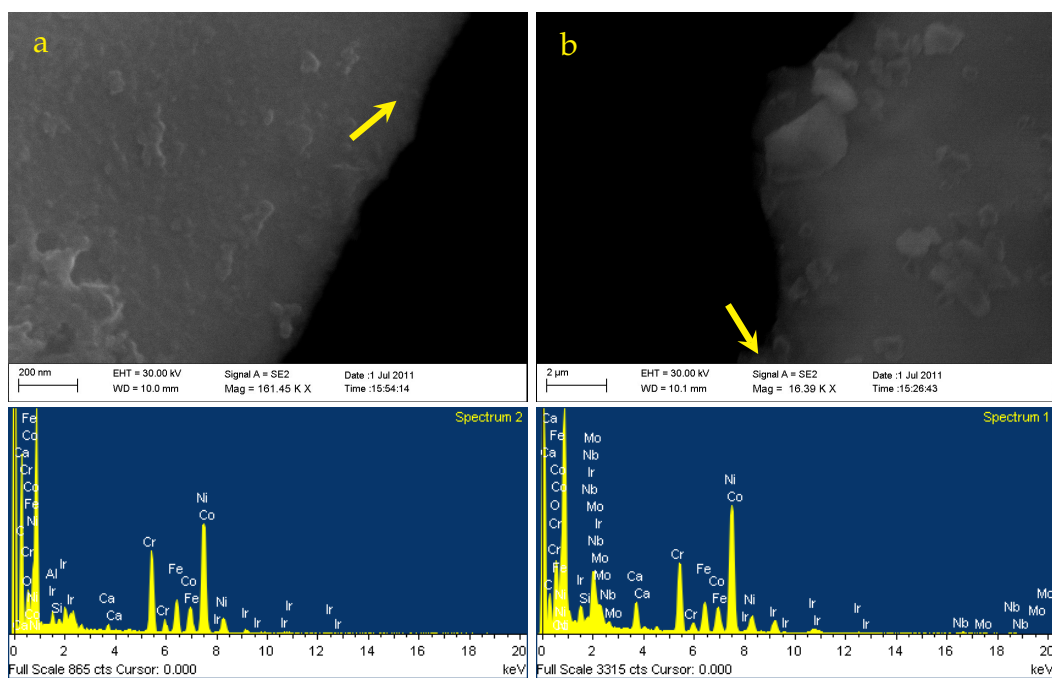


Figure 5.10: SEM and EDX (25 kV) of a TEM sample with IrO₂ (a) 30 μm and (b) 120 μm aperture.

5.6 Conclusions

In this chapter the iridium oxide deposition solution was investigated. Crystalline IrO₂ nanoparticles were found in the solution and were found to be, non-exclusively, involved in the IrO₂ deposition.

The oxidation of an oxalato complex, as has previously been suggested, is an unlikely path towards iridium oxide films, considering the low activity of oxalate oxidation on EIROFs and its inhibition in the presence of iridium in solution.

During the solution preparation hydrogen peroxide first, under acidic conditions, takes the role of a reducing agent and reduces Ir(IV) to Ir(III). During the development of the deposition solution, at pH 10.5, it acts as an oxidising agent, facilitating the formation of Ir(IV) oxide nanoparticles and very likely Ir(IV) oxyhydroxides.

6 pH sensing properties of hydrous iridium oxide

The pH sensing properties of electrodeposited iridium oxide films form the topic of this chapter. Focus lies on the relation between pH sensing and the oxidation state of the films. The contents presented here are a selection from Paper II, with a few extensions.

6.1 Introduction

The aim of this thesis project was to measure near surface pH with rotating ring-disc electrodes. Electrochemically deposited iridium oxide films (EIROF) were proposed as the pH sensing material on the ring. However, before starting these experiments a good understanding of the pH sensing properties of EIROFs was required.

Factors, such as storage medium, thickness and average oxidation state, have previously been shown to influence the response of hydrous layers.^{18,57} In this chapter, the relation between the average oxidation state and the pH sensing properties will be discussed in some detail, both in terms of new experiments (Paper II)¹⁷³ and density functional theory (DFT) calculations (Paper IV).¹⁷⁴

6.2 Film preparation

The EIROF deposition solution was the main topic of the previous chapter; its preparation was described in Sec. 4.5 and in more detail in Sec. 5.2.

The first films were deposited galvanostatically on platinum, gold and titanium.¹⁶ Tests with standard buffers showed good pH sensing properties, irrespective of the substrate, Paper II. However, on platinum the adhesion of the films was poor compared with gold and titanium. Platinum was therefore not used in further experiments.

The reproducibility of galvanostatic deposition was poor and the resulting films soft and easily damaged. Yamanaka described a heat treatment at 100 °C to obtain more sturdy films,¹⁶ but such a treatment was not possible in the present experiments, since it could cause cracks between the insulating and conducting parts of the electrodes. Instead, potentiostatic deposition, cyclic voltammetry and pulse plating were tested to improve the films.

Potentiostatic deposition proved more reproducible than galvanostatic, but the films remained soft. Elsen *et al.* observed that films produced with cyclic voltammetry and pulse plating are more compact and durable.¹⁸ Indeed, these methods both gave superior results, with respect to reproducibility and sturdiness. Between CV and pulse plating, cyclic voltammetry was chosen as the default method, because the voltammetric curves could conveniently be used to monitor the deposition process, Fig 6.1. The deposition procedure used throughout this chapter consisted of 600 cycles between the limits of -500 to 650 mV at 1 V s^{-1} , based on the work by Elsen *et al.*¹⁸ The resulting films were electrochromic, transparent in reduced form and blue/black after oxidation. The morphology of the films on gold was identical to those on titanium, shown in Fig. 5.5, an example on can be found in Paper I.

6.3 pH measurements

The first pH measurements were performed using standard buffers.¹⁷³ Once it was established that the films functioned properly, more detailed experiments were done using a universal buffer solution. This buffer was first described by Britton and Robinson¹⁷⁵ and consists of an equimolar solution of 0.04 M boric, acetic and phosphoric acid. Owing to the even spacing of the five pKa values associated with these compounds, Table 6.1, this buffer has a reasonably constant buffer capacity. Titration curves are therefore almost linear in the range pH 2 to 12,¹⁷⁵ an example is shown in Paper II.

The pH sensing properties of EIROFs were determined by monitoring their ocp in universal buffer solutions, while it was titrated with 1 M KOH.

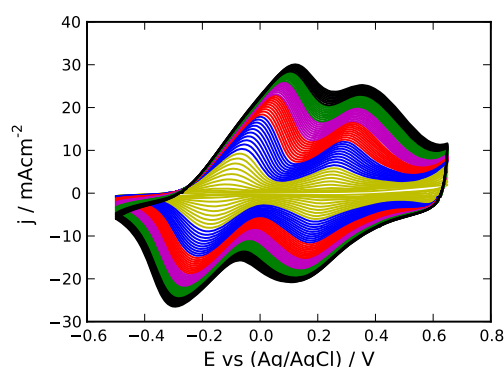


Figure 6.1: Cyclic voltammetry of iridium oxide during deposition on gold at 1 V s^{-1} . For clarity, only one in ten cycles is shown. The electrolyte was the deposition solution described in Sec. 4.5

Table 6.1: pK_a values in the Britton & Robinson buffer solution^{175,176}

compound	pK_a
H_3PO_4	2.16, 7.21, 12.32
$\text{C}_2\text{O}_2\text{H}_4$	4.76
H_3BO_3	9.27, > 14

Simultaneously the buffer pH was followed with a regular glass electrode. From these measurements closely spaced pH-ocp data were collected.

Fig. 6.2a shows the progression of the ocp of an EIROF during three different titration experiments. The annotations over the curve indicate the pH values measured with the glass electrode and the numbers in the legend will be discussed in Sec. 6.4. All EIROFs showed a fast response over the entire measured pH range. From Fig. 6.2a it can also be seen that there was a significant shift between the curves. The ocp at the start of the experiments varied from approximately 580 to 970 mV. To quantify the differences between the individual measurements more clearly, the ocp at the end of each step (Fig 6.2a) was plotted against the solution pH, Fig. 6.2b (open symbols). Linear fits to these curves (for $\text{pH} > 4$) showed that the intercept at $\text{pH} = 0$ varied from 855 to 1177 mV. In addition the pH sensitivity, defined as the slope $\frac{dE_{oc}}{dpH}$, was found to vary from 75 to 83 mV .

To gain understanding into this irreproducibility, titration experiments were performed where CV was measured after each KOH addition. A

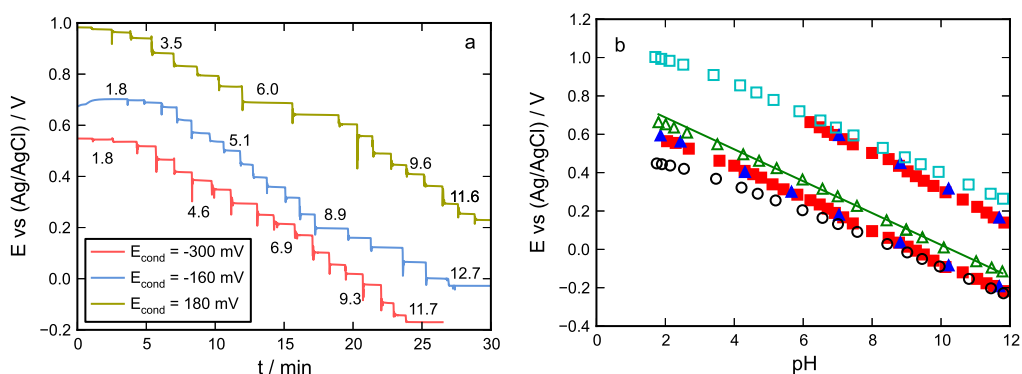


Figure 6.2: (a) Open circuit potential of an EIROF on gold in a universal buffer as it is titrated with KOH from pH 2 to 12. (b)(filled symbols) Equilibrium potentials of the Ir(III)/Ir(IV) and Ir(IV)/Ir(V) couples as a function of pH, calculated from voltammetric peak positions. (open symbols) ocp of EIROFS, as described in (a), as a function of pH in universal buffer solutions measured in independent titration experiments.

selection of the CV curves is shown in Fig. 6.3a. Two redox couples are visible, commonly ascribed to an Ir(III)/Ir(IV) and Ir(IV)/Ir(V) transition.¹⁷⁷ The dependence of the equilibrium potential on pH was determined for both couples by averaging the anodic and cathodic peak potentials in each CV. In Fig. 6.2b the resulting potentials are plotted against the solution pH (filled symbols). In contrast to the results from ocp measurements, the CV measurements were highly reproducible, with respect to both the slope and intercept. For pH > 4 the pH sensitivity for the first and second redox couple in the CV was -81 and -92 mV and the intercept potential 755 and 1246 mV, respectively.

In the introduction to this chapter it was mentioned that storage, thickness and oxidation state are factors that can influence the sensing properties. In the present work all films were stored in Milli-Q water when not in use and were deposited in the same fashion. Therefore storage and thickness were not considered first as the cause for the shifts in the ocp-pH characteristics. Additionally, the high reproducibility of the CV measurements indicated that the electrochemical nature of the different films was the same.

The fact that the intercept potentials measured through ocp lie in between those measured for the two couples in the CV, hints at a mixed oxidation state, as the origin of the variation in pH dependence. For a film in a

relatively reduced state the first couple would dominate, giving a lower slope and intercept, and vice versa for films in an oxidised state. Such behaviour has been observed before by Olthuis *et al.* for AIROFs and will be further explored in the next section.⁵⁷

6.4 Oxidation state

6.4.1 Experiments and results

The experiments described in this section were inspired by a study by Olthuis *et al.*⁵⁷ In this study AIROFs were subjected to a potential conditioning in 0.5 M H₂SO₄, prior to determining their pH-ocp characteristic in a universal buffer. With increasing oxidation state the AIROFs were found to show a higher pH sensitivity, approaching a limiting value at the highest oxidation states investigated.⁵⁷

In the present experiments EIROFs were used in place of AIROFs and conditioning was done in 0.1 M KOH instead of sulfuric acid. The choice for KOH over H₂SO₄ was made because it allows traversing both redox couples in the film. As can be seen from the cyclic voltammograms in Fig. 6.3a at low pH only the first couple is clearly separated from the oxygen evolution reaction (OER). However, owing to the super-Nernstian response of EIROFs (like AIROFs) the CV essentially outruns the stability window of water. Hence, at high pH the second couple separates from the OER, Fig. 6.3a.

The conditioning entailed fixing the electrode potential for 2 minutes. The potentials tested were chosen from -0.8 V to 0.4 V, spanning both redox couples in 0.1 M KOH, Fig. 6.3b.

The response curves shown in Fig. 6.2a were measured as a part of these oxidation state experiments. The three lines correspond to conditioning potentials of -300 , -160 and 180 mV. The rate and stability of the response in Fig. 6.2a are representative for all titration experiments performed.

pH-ocp characteristics were prepared as described on Sec. 6.3. The sensitivity and intercept were then determined by linear regression for pH 6 and higher. Including data points at lower pH resulted in the same trends, but less pronounced. The reason for this is that the sensitivity decreases somewhat at low pH values pulling the fits closer together, Fig 6.2b. The results are summarised in Fig. 6.4, which shows the sensitivity and intercept as a function of the conditioning potential. A CV in 0.1 M KOH was added to the graph to help correlating the conditioning potential to the redox processes in the film.

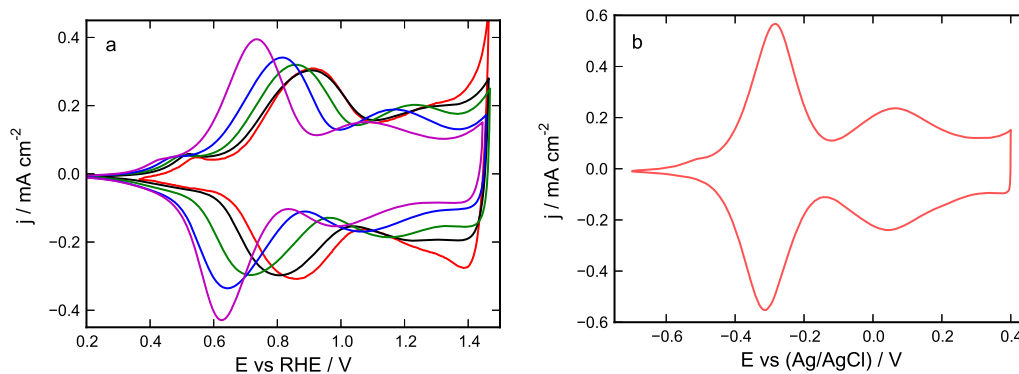


Figure 6.3: Cyclic voltammetry of an EIROF on gold in (a) universal buffer at pH 12 to 2 (left to right) with the potential relative to the reversible hydrogen electrode and (b) 0.1 M KOH, 10 mV s^{-1}

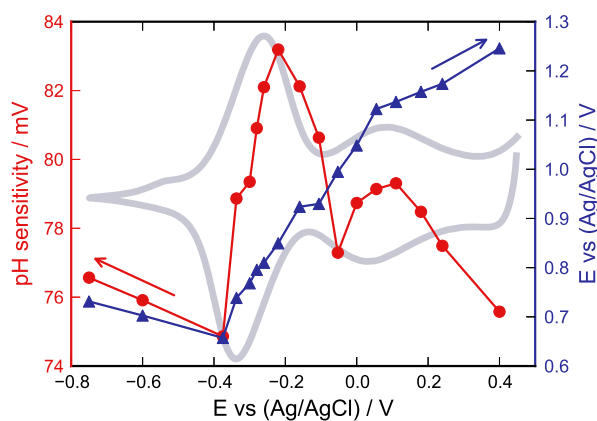


Figure 6.4: pH dependence of an EIROF prepared by CV on gold, as a function of the conditioning potential. The slope is represented by the red circles, quantified on the left axis. The blue triangles represent the standard potential, calculated by extrapolation to pH 0. Conditioning was performed in 0.1 M KOH, in which the CV shown in the figure was measured as well.

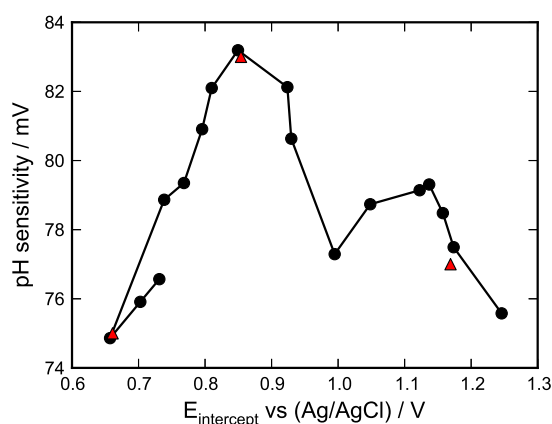


Figure 6.5: EIROF pH sensitivity as a function of the intercept of the titration curves at pH 0.

The present experiments revealed a more complicated relation between oxidation state and pH sensing properties, than was found earlier.⁵⁷ The sensitivity ranged from 74 to 83 mV, but did not level off. Instead it followed the cyclic voltammogram and showed maxima of 83 and 79 mV near the equilibrium potentials of the first and second redox couple, respectively. The first maximum matches well with the slope of the first equilibrium potential, obtained from CV, Fig 6.2b.

For values near the first redox couple, -400 mV to 80 mV, the intercept increased linearly with the conditioning potential with a slope of 1.0. Near the second couple a linear dependence was also observed but with a slope of merely 0.3.

In Fig. 6.5 the pH sensitivity is plotted as function of the intercept. In addition to the data from Fig. 6.4 three points from earlier experiments were added. These did not involve conditioning, but do show the reproducibility of the correlation between oxidation state and sensitivity.

To explain the relation between oxidation state and sensitivity Olthuis considered a mixed potential between different iridium oxyhydroxide species:⁵⁷ essentially an extension of the explanation for the super-Nernstian response that was discussed in Sec. 2.5.2.,¹⁹ Similar to aqua and hydroxide complexes an increase in oxidation state of the cation in oxides commonly leads to an increase in acidity.^{97,98} This would result in a higher sensitivity, as explained in Sec. 2.5.2 and summarised by Eq. 2.6. The sensitivity of the HIROF would then gradually shift to higher values as its oxidation state

increases.

Results from conditioning experiments in acid fit well within this explanation, however the maxima in sensitivity observed in the present experiments are in contradiction with a gradual move from a low to a high sensitivity redox state.⁵⁷ In addition, the separation of the two redox couples of almost half a volt is too large for a mixed region where Ir(III), Ir(IV) and Ir(V) coexist in appreciable quantities.

Two possibilities were considered to explain the results in Fig. 6.3. First, despite the mixed potential argument not holding, the role of the acid base properties of the films was further explored. Second, a mixed system of hydrous and anhydrous oxides was considered. In the next two sections these ideas will be presented.

6.4.2 Acid base argument

The surface pKa of an oxide can be related to its point of zero charge (pzc). In turn, the pzc can be estimated from the geometric mean of the atomic Mulliken electronegativities (χ_M) of the surface species.¹⁷⁸ Using this method pzc values were calculated for a variety of possible iridium oxide surface species, using atomic electronegativities from Butler and Giney.¹⁷⁹ A summary of the results is provided in Table 6.2.

Although the exact composition of the EIROFs is not known and some of the species in Table 6.2 might not exist as such, the general trends are interesting. For anhydrous species, a relation between pzc and oxidation state is indeed observed, albeit minor. On the basis of these calculations no major changes in surface acid base properties would be expected upon oxidation.

The calculated value For χ_{IrO_2} is 6.75 eV, corresponding to a pzc of 0.54. In comparison, Ardizzone *et al.* calculated a pzc value of 0.5¹⁸⁰ by relating the pzc to solid state parameters using Parks's equation,⁹⁸ as refined by Yoon.¹⁸¹ Experimental values of the pzc are scattered. Kosmulski reported a pzc of 3.3 and < 3 for two different iridium oxide samples.¹⁸² Similarly Ardizzone *et al.* reported the pzc as below 4.¹⁸⁰ Using probe beam deflection Kötzt *et al.* showed that the electrochemical transitions in AIROFs involve protons below pH 4 and hydroxyl ions above pH 4,¹⁴⁴ thereby also pointing at a pzc around pH 4.

In the present titration experiments the sensitivity decreased somewhat below pH 4, Fig 6.2b. On a RHE scale this decrease shows up as a maximum, Fig. 6.6, which remains in position regardless of the oxidation state of the

Table 6.2: Mulliken electronegativities (χ) and pzc, calculated by taking the geometric mean of atomic electronegativities.¹⁷⁹ When known, experimental values are given as well.

Oxide	Ox. No.	χ	pzc	pzc exp. val.
IrO ₃	VI	6.89	-0.52	
IrO ₂ (OH) ₂	VI	7.09	-1.91	
IrO(OH) ₄	VI	7.15	-2.36	
Ir(OH) ₆	VI	7.18	-2.60	
Ir ₂ O ₅	V	6.85	-0.23	
IrO ₂ (OH)	V	6.98	-1.16	
IrO(OH) ₃	V	7.10	-1.99	
Ir(OH) ₅	V	7.15	-2.38	
IrO ₂	IV	6.75	0.54	<3.9/<3 <2/3.3
IrO(OH) ₂	IV	7.02	-1.39	
Ir(OH) ₄	IV	7.11	-2.06	
Ir ₂ O ₃	III	6.60	1.60	5.3-5.5 partially reduced
IrOOH	III	6.85	-0.22	
Ir(OH) ₃	III	7.04	-1.56	

film. The location of this feature coincides with the pzc values reported in literature and the change in electrochemical reaction mechanism.^{144,180,182}

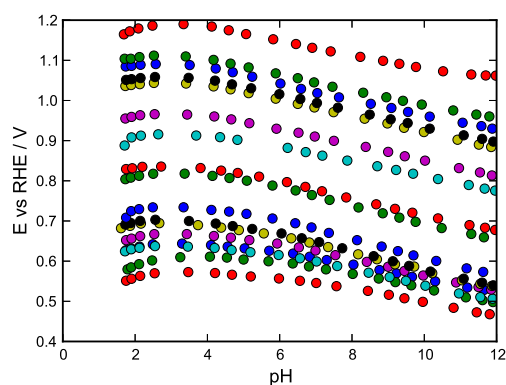


Figure 6.6: Titration curves of EIROF conditioned at different potentials. Fig. 6.4 and 6.5 were prepared from these data. The curves shift upward with increasingly positive conditioning potential.

Altogether, the calculations, titration curves and literature observations point at changes in pzc and thus acid base properties, as an unlikely cause for the variation of the pH sensitivity with oxidation state. Even more when taking into account that the data in Fig. 6.4 was generated from fits between pH 6 and 12, thus not including the pH region of the pzc.

6.4.3 Anhydrous vs hydrous contributions

The second hypothesis for explaining the results in Fig. 6.4 was based on the presence of hydrous and anhydrous phases in the EIROFs. This hypothesis was built on results from earlier studies on AIROFs and anhydrous IrO₂.^{19,37,56}

By averaging the anodic and cathodic peak potentials in cyclic voltammograms of AIROFs measured at different pH, Burke *et al.* found a pH sensitivity of 90 mV. From ocp measurements however, a sensitivity of merely 72 to 78 mV was found. In the present work similar results were obtained for EIROFs, as presented in Fig. 6.2b. In the same work by Burke *et al.* SIROFs showed an ocp sensitivity of merely 64 mV.¹⁹ In an earlier study on thermally prepared IrO₂ Ardizzone *et al.* measured a response of 59 mV, provided the system was allowed to equilibrate for a long time at each pH step.³⁷

Iridium oxide films always contain a mix of hydrous and anhydrous material, in a ratio that strongly depends on the nature of the material. Even a thermally prepared iridium oxide film will contain some hydrated material due to surface hydrolysis. AIROFs, although strongly hydrated, contain a thin anhydrous oxide layer at the interface between the hydrated oxide and the parent metal, Sec. 2.3.1.⁵⁶ SIROFs form an intermediate between hydrous and anhydrous. Hence, all three systems contain some hydrous and anhydrous material, with very different pH sensing properties. The resulting response is an average of contributions from both, with the pH sensitivity increasing with increasing degree of hydration in the order of thermally prepared IrO₂, SIROF and AIROF.^{37,40}

The slow approach of the anhydrous film to a limiting 59 mV response, observed by Ardizzone *et al.*, might be caused by a small contribution from the hydrolysed surface.³⁷ As the bulk of the oxide slowly equilibrates, its contribution grows compared with the fast responding hydrolysed surface groups, until it completely dominates.

A similar explanation can be given for the different ocp and CV response of hydrated films. The voltammetry of HIROFs shows clear redox features, Fig. 6.3. In contrast, the CV of anhydrous films mostly resembles that of a

purely capacitive system.^{183,184} Essentially the pH dependent CV consists of a 'feature rich' hydrous and a 'featureless' anhydrous part shifting at different rates, with only the former being clearly visible. The response observed from CV will thus exclusively come from the hydrous part of the film. However, through the ocp, an average of the two contributions is measured and the total response is dragged down by the anhydrous contribution.

At this point the question may be raised, whether there are indications of anhydrous iridium oxide in EIROFs. The original work by Yamanaka mentions crystalline matter in the deposits, prepared both anodically and cathodically.¹⁶ Furthermore, TEM images of a deposited iridium oxide film presented in the previous chapter, Fig. 5.9, show nanoparticles with clear lattice fringes, indicating crystallinity. The fringes correspond to a d-spacing of 2.22 to 2.26 Å, matching the (111) and (200) planes of IrO₂.^{170,171} It can therefore be concluded that similar to AIROFs, EIROFs contain some amount of anhydrous IrO₂. The pH sensing behaviour will thus be determined by a mixed contribution from both a hydrous and anhydrous part of the film.

This mixed contribution hypothesis can fully explain the results from Fig. 6.4 in terms of the relative redox buffer capacities of the two constituents in the film. Because the voltammetry of anhydrous iridium oxide resembles a purely capacitive system,²⁶ the redox buffer capacity of the anhydrous part is expected to be independent of the conditioning potential. In contrast, hydrous iridium oxide shows prominent features in the form of two sets of peaks, indicating that the redox buffer capacity strongly depends on the potential.

At the potentials where a 1:1 ratio is expected for Ir(III):Ir(IV) or Ir(IV):Ir(V) the hydrous component is most dominant, resulting in maxima in the pH sensitivity, Fig. 6.4. Away from these potentials, the redox buffer capacity of the hydrous oxide decreases, the anhydrous contribution becomes relatively larger and the pH sensitivity goes down. Hence, a pH sensitivity is expected that follows the cyclic voltammetry, in agreement with the experimental results.

The lower maximum at the second redox couple can also be explained within this framework. The intercept curve in Fig. 6.4 exhibits a slope of merely 0.3 in the vicinity of the second redox couple, compared with 1.0 around the first. For reasons discussed in Sec. 6.5 the film cannot fully adapt to the potential applied, like it was able to in the region of the first couple. The apparent smaller amount of active hydrous redox sites results in a lower dominance of the hydrous over the anhydrous component and

thus a lower maximum sensitivity.

6.5 Electrochemical properties and DFT

In the previous section, the pH sensing properties of EIROFs were shown to depend on the oxidation state of the film. Furthermore, Fig. 6.4 showed that the intercept of pH calibration curves, as a function of the oxidation state of the film, exhibits two linear regimes. In the potential range near the Ir(III)/Ir(IV) couple a slope of 1 was observed, while in the vicinity of the Ir(IV)/Ir(V) transition it is merely 0.3.

These findings imply that not all iridium sites are available for further oxidation to Ir(V). Similar conclusions can be drawn from the shape of the CV of EIROFs, which shows both redox transitions, but always with more charge on the first than on the second couple. This is most easily seen in alkaline solution, where the Ir(IV)/Ir(V) transition and OER are well separated, Fig. 6.8a.

In the literature it has been well established that the two redox couples in the CV correspond to Ir(III)/Ir(IV) and Ir(IV)/Ir(V), on the basis of X-ray absorption spectroscopy and UV photoelectron spectroscopy experiments.^{96,177,185} The question why the second couple carries less charge than the first will be addressed in this section, using results from experiments and DFT calculations.

A DFT study on the reaction mechanism of the OER on various transition metal oxides was conducted in another thesis project in the same research group as the present work.¹⁸⁶ In that work a binuclear OER mechanism was proposed and validated for oxides of, among others, Fe, Co, Mn and Cr.^{187,188} Applying this binuclear model to iridium oxide could give insight into the question of the uneven charges on the two redox couples in HIROFs. Since iridium oxide is both a transition metal oxide and an excellent OER catalyst, a collaboration on this issue was commenced. All the DFT work in this section was carried out by Michael Busch in collaboration with Itai Panas.

In this section a brief overview of the calculations and their results will be given. Focus lies on the results and how they can be used to interpret the experimental findings. For more details on the methods used for the calculations the reader is referred to Paper IV.

6.5.1 Models and mechanisms

The first model system was a 1-dimensional 2 monolayer thick $\text{MgO}_x(\text{OH})_y$ rig, where two adjacent magnesium ions were replaced with iridium,

Fig. 6.7a. This model was extended by placing two such rigs perpendicular to each other, with 14 Å separation, Fig. 6.7b. The binuclear iridium sites were used to model iridium oxide. Periodic rigs were separated by a 7 Å vacuum. The validity of the crossed rig was confirmed by comparing the energy profile with previous calculations on the single rig system.¹⁸⁹

In the binuclear mechanism the onset of oxygen starts with the oxidation of neighbouring Ir(IV)-OH sites to Ir(V)=O.¹⁸⁷ The role of the electrocatalyst is to render the two adjacent [TM=O/TM-O•] sites (TM = Transition Metal) sufficiently unstable, to form a peroxo bridge. The presence of this peroxo bridge initiates the catalyst recovery and release of oxygen through a series of chemical steps.

A competing, mononuclear, mechanism has also been described in the literature.^{190,191} In this mechanism only radical character on the [TM=O/TM-O•] site is required. In Paper IV the relation between the mono- and binuclear mechanism is discussed in detail.

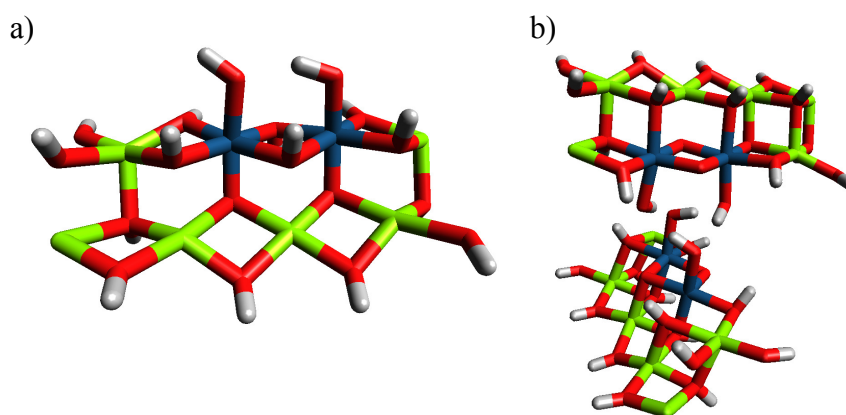


Figure 6.7: The employed model systems (a) Single rig system, and (b) Crossed rig system.

6.5.2 Results

The Ir(III)/Ir(IV) couple, the first redox feature in Fig. 6.8a, is attributed to the oxidation of an adsorbed water to hydroxide moiety, *i.e.* 2 Ir(III)-OH₂ are oxidised to 2 Ir(IV)-OH, Fig. 6.9a. This step was not modelled explicitly. In the next step, at the second peak, an oxo-hydroxo (Ir(IV)Ir(V)) or di-oxo (Ir(V)Ir(V)) intermediate could be formed. However, ensemble effects are expected to suppress the possibility of two adjacent Ir(V)=O moieties, leading to the oxidation of only a part of the surface hydroxide

groups. This is supported experimentally by the lower charge observed for the second couple in the cyclic voltammetry, Fig. 6.8a, as well as the suppressed increase in the intercept at high conditioning potentials, Fig. 6.4.

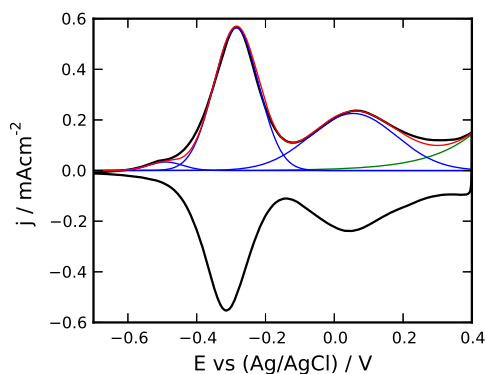


Figure 6.8: Cyclic voltammograms ($v = 10 \text{ mV s}^{-1}$) of an EIROF (a) in 0.1 M KOH. The anodic scan was fitted using 3 Gaussians transitions (prepeak + 2 IrO_x transitions) and one exponential function (OER)

Assuming a binuclear mechanism,¹⁸⁷ the onset of oxygen evolution is found when neighbouring Ir(IV)-OH become oxidised to Ir(V)=O . The thus formed di-oxo species displays two weak double bonds and may readily form the crucial μ -peroxo intermediate, Fig. 6.9c. $[\text{Ir(IV)-OH Ir(V)=O}]$ displays only one such weak bond and does not support the OER according to the binuclear mechanism. The appearance of an $\text{Ir(IV)Ir(IV)/Ir(IV)Ir(V)}$ oxidation process preceding the OER therefore supports the binuclear mechanism.

For the mononuclear OER mechanism Lundberg *et al.* proposed that a requirement for an efficient O–O bond formation is the appearance of radical character at the TM=O/TM-O^\bullet moiety.¹⁹² Thus, this property may be used as a descriptor for the onset of OER in the mononuclear mechanism paradigm. Radical character on the mixed Ir(IV)/Ir(V) HIROF system could not entirely be ruled out by the calculations at the GGA level of theory. However, the radical character on mixed Ir(IV)/Ir(V) oxides may be quenched by hydrogen bonding, in which case the mononuclear OER path is not feasible.

The possibility that the radical character at an Ir(V)=O site would be quenched by neighbouring Ir(IV)-OH sites was investigated using the crossed rig model, Fig. 6.7b. This crossed rig system facilitates inclusion of

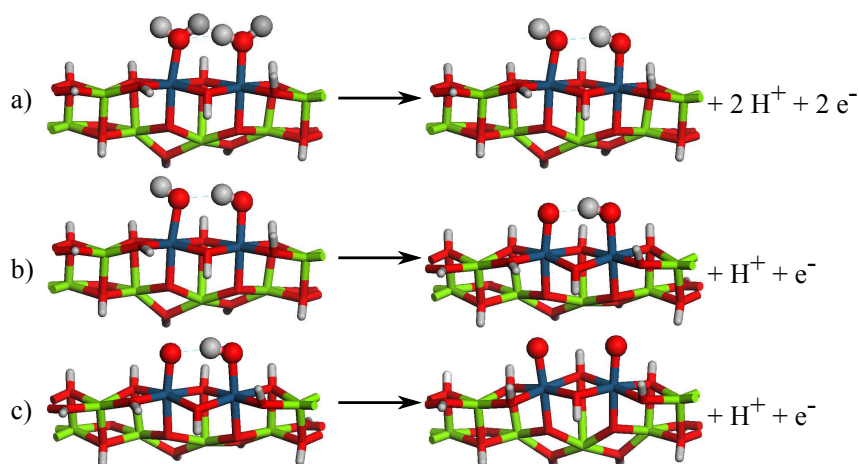


Figure 6.9: The electrochemical steps used to model the OER at HIROF. The electrochemical reactions proceed through oxidation of adsorbed water to hydroxo moieties (A; not modelled explicitly). The dihydroxo intermediate is oxidised to a oxo-hydroxo intermediate (b). In the final electrochemical step the remaining hydroxo moieties are oxidised to oxo species (c).

ensemble effects without changing the overall model. The configuration was chosen, such that it reflects the flexibility of HIROF and allows for hydrogen bonding between the layers. Strong hydrogen bonding between the layers was indeed found for all structures containing hydroxo moieties. Upon subsequent removal of e^-/H^+ couples from Ir(IV)-O^\bullet , moieties with mostly strong radical character at the oxygen were again obtained at the GGA level of theory, thus supporting the findings obtained for the single-rig system. For the single rig system the Ir-O^\bullet was found unstable towards quenching of the oxygen radical character by hydrogen bonding and it is likely that such an effect exists also in the crossed rig configuration. Support for the existence of such an instability towards removal of the radical character on the oxy group was obtained for the $[(\text{Ir(IV)-OH})(\text{Ir(V)=O})_3]$, see Paper IV.

6.5.3 Interpretation of iridium oxide CV

Within the paradigm of the binuclear OER mechanism, the voltammetry of iridium oxide can be explained as follows. The second redox couple in the CV represents the transition of part of the film from Ir(IV) to Ir(V) oxide. At this intermediate state, the Ir(V)=O moieties are stabilised by hydrogen bonding with adjacent Ir(IV)-O^\bullet moieties, inhibiting the OER.

Because of the super-Nernstian and nernstian shifting of the iridium

oxide CV and the OER, respectively, the position of the OER relative to the iridium oxide CV, depends on pH. In acid the second redox couple and the OER overlap strongly, while under alkaline conditions they are well separated. Comparing the OER itself as a function of pH is difficult, due to the overlap. However, fittings of the CV, as shown in Fig. 6.8a, implied no great changes in overpotential, in agreement with earlier findings.¹⁹³

On the reduction scan the current near the anodic switching point increases with decreasing pH, indicating that more Ir(V) oxide is formed, Fig. 6.3a. This can be explained as follows. Under alkaline conditions the bare interactions between Ir(V) sites effectively prohibit further oxidation beyond said 1:1 ratio. Upon lowering pH, the screening of Ir(V) sites, owing to hydrogen bonding between $[\text{Ir(V)=O} \leftrightarrow \text{Ir(V)-OH}]$ and Ir(IV)-OH sites, allows for increased surface concentration of Ir(V) sites beyond 1:1. According to this argument protons redirect the binuclear OER to Ir(V) oxide formation.

6.6 Conclusions

The pH sensing behaviour of electrodeposited iridium oxide films was investigated, with emphasis on the influence of the oxidation state. A series of titration curves was measured for EIROF in a universal buffer, for different oxidation states of the films. The oxidation state was varied by potential conditioning in 0.1 M KOH. For all tested conditioning potentials the pH response was super-Nernstian, but it varied from 75 mV to 83 mV.

Two maxima were observed in the pH sensitivity as a function of the conditioning potential. The size and position of the maxima matched well to the CV of EIROF in 0.1 M KOH. These results were explained in terms of contributions from hydrous and anhydrous iridium oxide in the films.

The titration curves shifted positive with increasingly positive conditioning potential. This was quantified by comparing the potential at pH 0, obtained by linear regression. For conditioning potentials near the Ir(III)/Ir(IV) couple the curves shifted with a slope of 1. Near the second couple, however, the slope was merely 0.3, indicating that only part of the film could be further oxidised to Ir(V).

The inability of HIROF to completely adapt to potentials beyond the Ir(III)/Ir(IV) couple was explained within the context of the mechanism for the oxygen evolution reaction. DFT calculations provided evidence for a binuclear oxygen evolution pathway. Ensemble effects were shown to inhibit complete oxidation to Ir(V) oxide, leading to the interpretation that

the second redox feature in the HIROF CV is an oxidation step from Ir(IV) oxide to a mixed Ir(IV)Ir(V) oxide. Further oxidation, with formation of Ir(V)Ir(V) sites, leads to oxygen evolution and Ir(V) oxide depending on pH. In acid solution the Ir(V)Ir(V) site is stabilised by hydrogen bonding, in agreement with the experimental observation of a larger reduction peak as pH is lowered.

7 RRDE pH measurements with iridium oxide

Local pH measurements with a rotating ring-disc electrode are the subject of this chapter. The experiments discussed here were published in Paper III, some additional details, regarding the experimental setup, are also given.

7.1 Introduction

In the previous chapters the deposition and pH sensing properties of electrodeposited iridium oxide films were discussed. The present chapter deals with the use of EIROFs for near surface pH measurements with a rotating ring-disc electrode (RRDE).

Water and oxygen reduction were chosen as test cases, the first because of its experimental simplicity and the second as a step towards the main goal of this thesis, measuring local pH during ZnO electrodeposition. This process is based on the precipitation of ZnO driven by electrochemically induced changes in near surface pH.^{2,5} In the present work, depositions were carried out at 80 °C from mildly acidic zinc chloride solutions by increasing the pH near the electrode surface by reducing oxygen. Besides this central role in ZnO deposition, the ORR also shows two separate reaction pathways on gold, involving 2 and 4 electrons. A somewhat complicated system like the ORR makes for a more rigorous test case.

The experimental results from the RRDE-pH measurements on both water and oxygen reduction were published in Paper III. The present chapter

focuses on the oxygen reduction experiments. Important findings from the water reduction measurements will be mentioned and discussed, for more detailed results the reader is referred to Paper III.

Before moving on to the RRDE experiments, the influence of hydrogen peroxide on the pH sensing behaviour of EIROFs is discussed. This is important because H_2O_2 is produced in the 2 electron ORR and its interference with the pH measurements needed to be ruled out. The experiments on H_2O_2 were published in Paper II, but since they were performed explicitly in preparation of the RRDE-pH measurements, their presentation was moved to Sec. 7.2 of the present chapter.

7.2 EIROF pH sensing properties and H_2O_2

pH measurements with EIROFs rely on the pH dependence of the ocp. However, interaction of the EIROF with redox active solution species could influence the ocp as well, leading to erroneous interpretation of measurements. For example, it has been shown that hexacyanoferrate, can control the ocp of EIROF and effectively block the pH response.¹⁰¹

One of the possible products of the ORR on gold is hydrogen peroxide. Small amounts of hydrogen peroxide will not influence the solution pH, but as a redox active compound, it might influence the EIROF's ocp. Therefore, the influence of hydrogen peroxide on an EIROF deposited on gold was tested, prior to the RRDE experiments.

In the previous chapter, Sec. 6.4, the relation between oxidation state and pH sensing properties was demonstrated. Here, oxidation state was also considered a potentially important parameter. Therefore, two experiments were performed where the EIROF was conditioned at the equilibrium potential of the Ir(III)/Ir(IV) or Ir(IV)/Ir(V) couple, Fig. 6.4. In practice, the conditioning was performed in 0.1 M KOH for 2 minutes at -256 mV and 71 mV.

After conditioning, the electrode was placed in a standard buffer of pH 7 and an ocp measurement was started. Next, aliquots of hydrogen peroxide were added to the solution, while monitoring the ocp, Fig. 7.1a. When the EIROF was conditioned at -256 mV (green line) the ocp changed by merely 4 mV during the experiment, thus no significant influence of H_2O_2 was found. In contrast, when the EIROF was conditioned at 71 mV the ocp responded strongly to H_2O_2 additions (blue line). H_2O_2 reduced the film to the same state as was achieved by conditioning at -256 mV. The effect is illustrated by the two curves in Fig. 7.1a approaching each other.

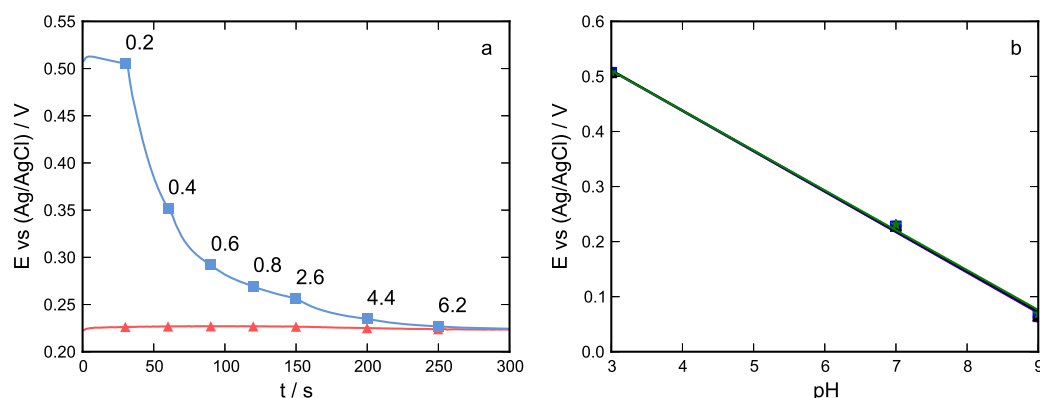


Figure 7.1: (a) Potential response of an EIROF, conditioned in 0.1 M KOH at ■ 71 mV and ▲ -256 mV, to additions of H₂O₂. The annotations specify the H₂O₂ concentration in mM. (b) pH response measured in standard buffers containing 0 to 0.6 mM H₂O₂, for an EIROF conditioned at -256 mV in 0.1 M KOH .

The impact of H₂O₂ was further tested by measuring calibration curves in standard buffers containing an increasing amount of H₂O₂. The upper limit was chosen on the basis of the expected maximum hydrogen peroxide concentration during the RRDE experiments. Albery *et al.*⁹ showed that low rotation rates give optimal results in potentiometric RRDE experiments. At a rotation rate of 500 rpm, the surface concentration of H₂O₂ amounts to approximately 0.5 mM. Since only part of the product from the disc reaches the ring, the surface concentration there will be even lower.

Taking into account the results from Fig. 7.1a the EIROF was conditioned at -256 mV, prior to the measurements. Fig. 7.1b shows the calibration curves measured in the presence of 0 mM to 0.6 mM H₂O₂. Under the chosen conditions no influence of H₂O₂ was revealed.

The results in this section show the importance of bringing the EIROF in a suitable oxidation state prior to pH measurements in the presence of hydrogen peroxide. Most likely this can be extended to other redox active species, depending on their concentration. Suitable conditioning can be achieved, passively, by equilibration in the presence of interfering species or, actively, by potential conditioning. Therefore, H₂O₂ can be prevented to interfere with the EIROF pH sensing properties during the RRDE experiments.

7.3 RRDE preparation

The geometry of a RRDE is defined by the disc radius and the inner and outer radii of the ring, r_0 , r_1 and r_2 , respectively. The RRDEs used for this chapter consisted of a gold disc and titanium ring, with $r_0 = 1.5$ mm, $r_1 = 1.75$ mm, $r_2 = 2.75$ mm. Titanium was chosen for the ring material, because of its adhesive properties as a substrate for EIROFs.

EIROFs were prepared, as described in Sec. 4.5.2. The number of cycles was reduced from 600 to 300 to limit the film thickness and improve the response times. In accordance with the electrochemical activity of iridium oxide films on titanium, the potential limits were adjusted compared with the depositions on gold in the previous chapter. The anodic processes start roughly 400 mV later on titanium than on gold, see Fig. 6.1 and 7.2. This turned out to have important consequences for the present experiments as will be discussed in Sec. 7.5.2. The films on gold and titanium look identical in SEM, an example of a film on Ti is shown in Fig. 5.5.

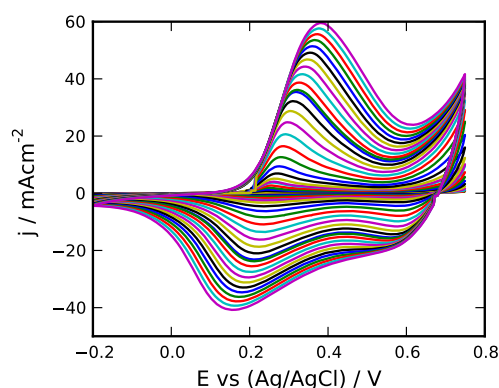


Figure 7.2: Cyclic voltammetry of iridium oxide during deposition on titanium at 1 V s^{-1} . For clarity, only one in ten cycles is shown. The electrolyte was the deposition solution described in Sec. 4.5

Freshly deposited EIROFs are unsuitable for pH measurements because they exhibit a drift in ocp at constant pH. This can be resolved by soaking the electrode in water for several hours or preferably overnight. On titanium the initial drift seemed more pronounced than on gold, but this was not explicitly tested. The EIROFs used in this chapter were always soaked overnight before using them.

Before, after and in between RRDE experiments the electrolyte's pH was measured with a glass electrode and the EIROF's pH response was determined using standard buffers of pH 3, 7 and 9. All the RRDE experiments in this chapter were performed in a deaerated 0.1 M NaClO₄ electrolyte, purged with nitrogen for at least half an hour.

7.4 Correction of the ring potentials

Miksis *et al.*¹⁹⁴ described how currents on the disc induces an addition potential drop at the ring, and vice versa. The disc currents used in the RRDE pH experiments were high enough to take this into consideration.¹⁰² The effects were calculated for the primary current distribution and described in terms of primary resistances.¹⁰² Eq. 7.1 and 7.2 were obtained and provide means to correct, in the present case, the ring potential for the disc current.

$$\frac{\Phi}{\Phi_0} = \kappa r_2 R_{rd} \frac{4r_0}{r_2} \quad (7.1)$$

$$\Phi_0 = \frac{I_{tot}}{4\kappa r_0} \quad (7.2)$$

Where, Φ_0 is the potential at the disc, Φ potential at infinite distance, κ conductivity, R_{rd} ohmic resistance between disc and ring. For the electrodes used, $\kappa r_2 R_{rd}$ in Eq. 7.1 equals 0.21, as tabulated by Miksis *et al.*,¹⁹⁴ $r_0 = 0.15$ cm (disc radius), $r_2 = 0.275$ cm (outer ring radius) and $\kappa = 9.84$ mS cm⁻¹.¹⁹⁴

Before determining the pH at the ring, the measured ring potential was always corrected for potential drop induced by the disc current. For current densities of -1 to -3 mA cm⁻², the ring potentials shift negative by 5 to 16 mV, corresponding to 0.1 to 0.2 pH units.

7.5 RRDE-pH current step experiments

In the current step experiments the disc was stepped to a fixed current, while the ocp of the ring was followed. Galvanostatic conditions were chosen because the pH is directly related to the disc current density, Sec. 3.1.2.⁹

7.5.1 Experimental

The experimentally used current densities were chosen, such to span the range of pH 9 to 12 at the disc surface, for rotation at 300 rpm. Currents corresponding to pH 9 and 12 were calculated using Levich's model under

non limiting current conditions, Sec. 3.1.2. Because of the logarithmic dependence of the pH on the disc current, the values in between were chosen roughly linear on a log scale. Altogether this resulted in the following list of current densities: -0.03 , -0.1 , -0.3 , -1 and -3 mA cm^{-2} . In the first set of experiments on water reduction an additional step at -10 mA cm^{-2} was attempted, but hydrogen evolution disturbed the experiments significantly. Hence, this step was removed from the list.

At higher rotation rates reaction products are more efficiently removed from the electrode surface. The concentration differences between bulk and the diffusion layer are therefore larger at lower rotation rates, Fig. 3.3. For the reactions studied presently, this means a smaller pH increase for higher rotation speeds. To test this experimentally the rotation rate of the electrode was varied during each measurement, in the order 300, 1500, 600 and 1200 rpm.

Equilibrium of the EIROF with the bulk solution was ensured by placing the electrode in the oxygen saturated electrolyte 1 hour before starting the measurements. Further details on the procedures can be found in Paper III.

7.5.2 Results and discussion

The limiting current density for a rotating disc electrode can be calculated from the Levich equation,¹³⁸

$$j = 0.62nFD^{\frac{2}{3}}\nu^{-\frac{1}{6}}\omega^{\frac{1}{2}}c \quad (7.3)$$

with the number of electrons n , Faraday constant F , kinematic viscosity of electrolyte ν , rotation rate ω , diffusion coefficient D and concentration of the electroactive species c .

For a 0.1 M NaClO_4 solution the following physical constants apply: $D_{\text{O}_2} = 2.01 \times 10^{-5} \text{ cm}^2 \text{ s}^{-1}$, $\nu_{\text{H}_2\text{O}} = 8.9 \times 10^{-3} \text{ cm}^2 \text{ s}^{-1}$ and $c_{\text{O}_2} = 1.22 \text{ mM}$.¹³⁸ The oxygen solubility was corrected for the presence of 0.1 M NaClO_4 using a Setschenow salt parameter of 0.160 and a solubility in pure water of 1.266 mM .¹⁹⁵

The 2 electron ORR dominates under all reaction conditions tested, except for the step to -3 mA cm^{-2} at 300 and 600 rpm. At 300 rpm the limiting current density for the 4 electron process equals -2.7 mA cm^{-2} and hence, hydrogen evolution is involved at -3 mA cm^{-2} . For 600 rpm the limiting current density for the 2 electron process is -1.9 mA cm^{-2} and the 4 electron process must be involved to maintain -3 mA cm^{-2} . A similar assessment can be made from Fig. 7.5, which shows a set of linear

sweep voltammograms (at 300 and 900 rpm) measured in the same oxygen saturated solution.

Fig. 7.3 shows the ring response to the current steps and the changes in rotation rate. The slopes and intercepts defining the pH sensing properties of the ring are given in Table 7.1. These values were obtained from linear fits to the calibration curves measured before and after each step experiment. This table illustrates the high stability of the pH sensing properties during the experiments, with respect to both the sensitivity and intercept. This contrasts with the water reduction experiments, where the intercept shifted negative by 200 mV. At the end of water reduction series the oxidation state of the film corresponded to the region between -200 mV and -133 mV in Fig. 7.2. For the ORR series this was -37 mV, still far from the region of maximum redox activity. This is reflected in the relatively low sensitivity of 65.7 mV, Fig. 6.4 and Sec. 6.4.3.

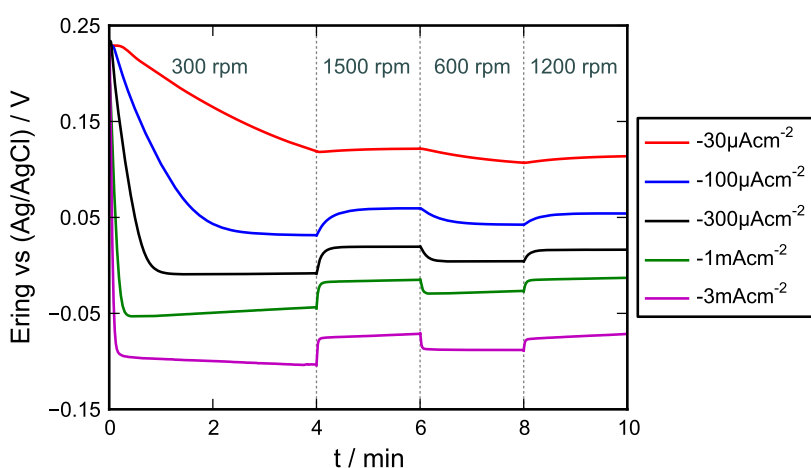


Figure 7.3: Ring potential during a series of current steps on the disc, in oxygen saturated 0.1 M NaClO_4 . The rotation rate was changed in the order 300, 1500, 600, 1200 rpm, each for 2 minutes except 300 rpm for 4 minutes.

An explanation for the difference in EIROF stability was sought in the changes in local redox environment after starting the measurements. For the water reduction experiments the electrolyte did not contain any bulk redox species. However, during a measurement the EIROF experienced a reducing environment owing to H_2 formation. The situation is different for the ORR experiments, where the electrolyte contained an oxidising agent in the form of oxygen, to which the EIROF was conditioned by equilibration.

Even under limiting current conditions, the concentration at the ring of the species reacting at the disc, will not be zero. The shielding factor of an RRDE is geometrically determined and gives the decrease in limiting current at the ring, for zero and limiting current conditions at the disc.¹³⁸

The shielding factor for RRDEs of the geometry used for the RRDE-pH experiments is 0.45. Hence, under limiting current conditions at the disc, the flow of oxygen to the ring is still about half of that under zero current conditions. The oxygen that reacted at the disc is replaced with H_2O_2 , which was shown to have little influence on the pH sensing properties. Only during the measurements at -3 mA cm^{-2} at 300 rpm would hydrogen be formed. Its influence at the ring however, would be inhibited by the presence of oxygen from the bulk.

Interestingly the potential of the electrode in the present experiments was very similar to that in the H_2O_2 experiments, Sec. 7.2. Comparing the calibration curves measured in the presence of peroxide and in the present experiments, the difference is about 53 mV.

Table 7.1: Linear fit results for the calibrations curves measured in standard buffers in between the O_2 step experiments, a represents the slope, b the intercept at $\text{pH}=0$

j / mA cm^{-2}	pre		post	
	a / mV	b / mV	a / mV	b / mV
-0.03	-65.7	664.0	-65.8	661.5
-0.10	-65.7	641.9	-65.7	640.9
-0.30	-65.6	639.1	-65.7	641.9
-1.00	-65.7	640.9	-65.7	664.0
-3.00	-65.8	661.5	-65.5	652.4

Fig. 7.4 clearly shows how the response time decreases with the current density. For the measurement at $-30 \mu\text{A cm}^{-2}$ no stable reading could be obtained within the first four minutes of the measurement. In contrast, at -3 mA cm^{-2} the initial response occurs within seconds. This effect is also visible at each of the changes in rotation speed.

Majda *et al.* discussed the response time of iridium oxide based potentiometric sensors in terms of their finite capacitance and mass transport effects.^{8,18,196} To establish equilibrium with the solution the EIROF needs to exchange hydroxide ions or protons. At neutral pH neither species is abundantly available and during equilibration depletion occurs at the EIROF

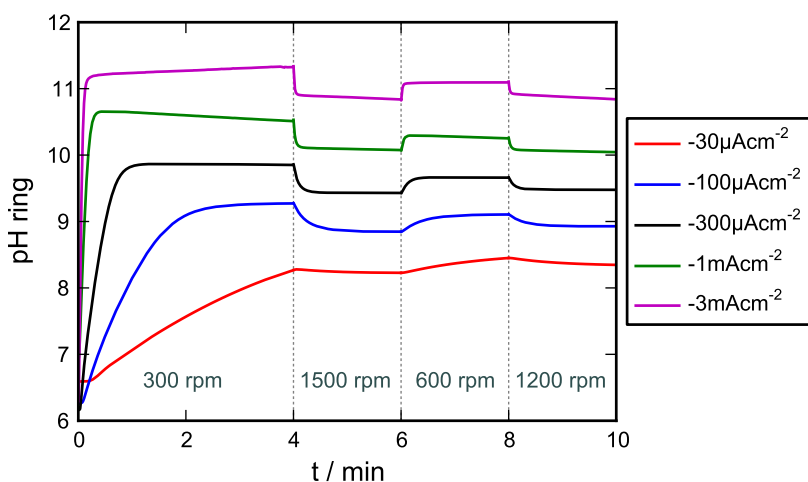


Figure 7.4: Ring pH as calculated from the ring potential and the calibration curves, in Table 7.1 and Fig. 7.3

surface. Hence, mass transport becomes a factor in the equilibration process, resulting in a lower response rate. At higher pH the response rate improves because hydroxide ions are sufficiently available in the near surface area and mass transport is no longer a limiting factor. This effect is enhanced by the porous nature of the EIROF, since the amount of solution species required for equilibration increases with the (internal) surface area.

By decreasing the volume of the film, either through its thickness or area, the response time might be improved. The film thickness can be controlled by the number of cycles, as well as the potential limits during deposition. The area of the EIROF can be reduced by changing the RRDE geometry to a thinner ring-disc gap and a thinner ring. A thinner gap would however have the disadvantage of increasing the influence of the disc current on the ring potential, Sec. 7.4.^{102,194}

7.6 RRDE-pH Linear sweep voltammetry

7.6.1 Experimental

Ideally the RRDE-pH system should allow real time measurements, to track changes in near surface conditions, as they occur. Therefore, in addition to the current step experiments a series of linear sweep voltammetry (LSV) was measured. Again, experiments were performed both on water and oxygen reduction in unbuffered 0.1 M NaClO₄, but focus lies on the ORR.

LSV was measured at 5 mV s^{-1} down to -1.75 V , starting at -0.1 V and 0.2 V for water and oxygen reduction, respectively. The rotation rates tested were, 300, 600, 900 and 1500 rpm. Prior to each sweep the disc was cleaned by oxidising and reducing it twice. Right before and after each sweep the electrode was allowed to equilibrate for 10 min (3000 rpm). Further details can be found in the experimental section of Paper III.

7.6.2 Results and discussion

The results from the LSV experiments, measured at 300 and 900 rpm are shown in Fig. 7.5. The ring potentials were corrected for the potential drop induced by the disc current (as described in Sec. 7.4) and converted to pH using calibration curves ($a = 69 \text{ mV}$, $b = 761 \text{ mV}$). Fig. 7.5 shows the disc current and ring pH as a function of the potential, on the left and right ordinate, respectively. To show the relation between current and pH more clearly, pH was plotted as increasing in the negative direction.

In addition to the experimental pH, the theoretical surface pH at the disc is included in Fig. 7.5. These values were calculated using the disc current and Levich's model for non limiting current conditions, Sec. 3.1.2.¹³⁸

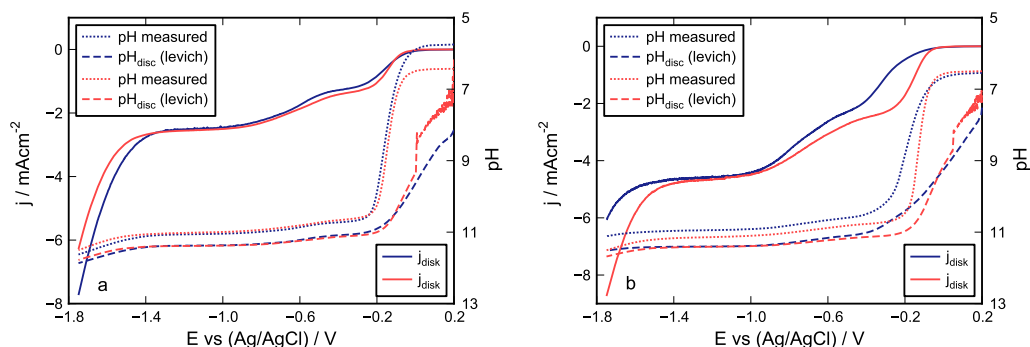


Figure 7.5: Linear sweeps in O_2 saturated 0.1 M KCl , with rotation at (a) 300 and (b) 900 rpm. The solid lines represent the disc current, dashed lines the theoretical surface pH, dotted lines the measured pH on the ring.

For the theoretical curves in Fig. 7.5 a bulk pH of pH 7 was assumed. As a result minimal current densities at the start of the sweep show up as large changes in pH. This coincides with the region of slow response of the EIROF and results in a large discrepancy between the measured and calculated pH. As the scan progresses the current density and pH increase and the EIROF's response rate improves. Between -0.1 V and -0.2 V the

experimental curves catch up with the theoretical ones. The difference between experimental and theoretical pH in the plateau regions can be attributed to the efficiency of the system.

For amperometric RRDE experiments the collection efficiency of the RRDE is defined as the ratio between product concentration on the disc and product concentration detected on the ring. The collection efficiency can either be measured experimentally using a standard system (*i.e.* hexacyanoferrate), or calculated from the three radii defining the electrode geometry. For potentiometric experiments a geometrically defined detection efficiency exists as well, but it differs from the traditional collection efficiency, see Sec. 3.1.2.⁹ Furthermore, since the pH depends logarithmically on the hydroxide concentration the efficiency shows itself as a constant offset instead of a ratio. In the present experiments the geometry of the RRDE should lead to a pH at the ring that is 0.6 units below that at the disc.⁹

The LSV in Fig. 7.5 already shows that the measured relation between disc current and ring pH is not linear. The lagging and catching up of the ring response, discussed above, is more clearly visualised in a plot of $\log |j_{disc}|$ against the ring pH, Fig. 7.6b.

Ideally the ring response should be linear with the logarithm of the disc current. Furthermore, the slope should be unity for a 1 electron per hydroxide process. However, in Fig. 7.6b, the ring pH initially seems independent of the disc current, until approximately -0.01 mA cm^{-2} . As the current density further increases, the response starts to exceed unity around -0.1 mA cm^{-2} . Finally close to 1 mA cm^{-2} a linear regime is reached. The slope however is around 0.8, indicating the ring measurements are overestimating the pH changes. Similar results were obtained from the current step experiments. Both are summarised in Table 7.2. The origin of this phenomenon is attributed non-ideal behaviour of the experimental setup. However, a full explanation would be an interesting track for future work.

7.7 Practical considerations

As mentioned at the start of this chapter, the final purpose of the experiments described here was to measure on the electrodeposition of zinc oxide. An important complication in such experiments is the temperature required for the experiments. Regular ZnO depositions are performed at 80°C , which puts high demands on the electrodes used. Differences in thermal expansion of the electrode and case material can cause cracks between the case and the electrode.

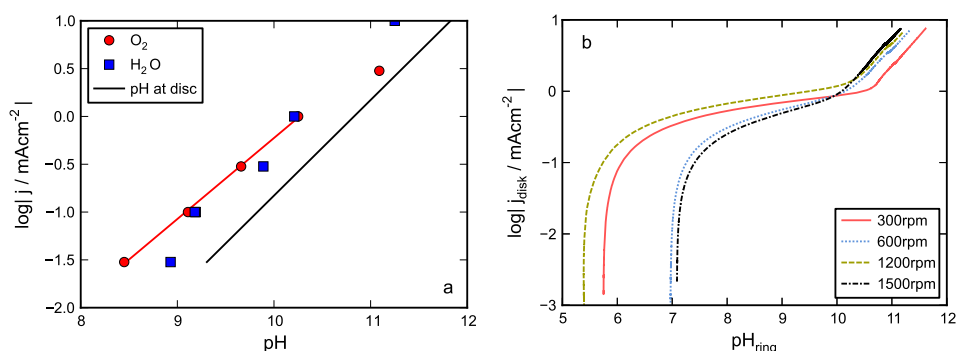


Figure 7.6: (a) pH measured on the ring as a function of the logarithm of the disc current, at a rotation rate of 600 rpm. (b) Logarithm of the disc current density as a function of the ring pH, for linear sweep experiments in oxygen saturated 0.1 M NaClO_4 .

Table 7.2: fits of $\log(j) - \text{pH}$, for O_2 reduction. Only the points up to 1mA were used in the fits.

w/rpm	steps		LSV	
	a	b	a	b
300	0.81	-8.5	0.84	8.9
600	0.85	-8.7	0.79	7.9
1200	0.89	-8.7	0.79	8.0
1500	0.82	-8.2	0.84	8.5

The RDEs used in this thesis were home made. A 3 mm wide cylinder of the electrode material was glued to a cylindrical brass holder with silver epoxy. This piece was then either pressed into a PEEK body or cast in epoxy (Epofix, Struers). After curing the epoxy was worked into an approximately 1.3 cm wide cylinder. RRDEs were prepared in epoxy in a similar fashion, but around the brass piece containing the disc a second brass cylinder was placed that supported the ring. These were centred and cast in epoxy.

When cracks exist between the epoxy and metal a liquid contact can form between iridium oxide film and the brass support. In this situation the iridium oxide can be reduced at the expense of the brass. As a result ocp measurements in buffer solutions do not result in stable readings, but

drift towards a single potential value, regardless of pH.

The assumption of crack formations was confirmed in various ways. First, after some use an oxide became visible on the brass inside the epoxy. Second, after removing IrO₂ films by polishing, small peaks remained visible in the CV. Third, charging current on clean electrodes also increased up to a factor 100. Finally, the presence of iridium oxide in between the metal and epoxy was confirmed with EDX.

Attempts were made to use different epoxy resins to prepare electrodes that can withstand a higher temperature, but unfortunately this did not succeed. Therefore the application of EIROFs in the study of zinc oxide electrodeposition remains an experimental challenge.

Also in room temperature experiments leaking electrodes provided a challenge. The best results in electrode preparation were obtained after roughening the metal surface with SiC paper and treating it with, 3-glycidoxypropyltrimethoxysilane in pentane.¹⁹⁷ This compound functions as a linker between the metal and epoxy, improving the sealing.

7.8 Conclusions

Electrodeposited iridium oxide was successfully used as pH sensor in a RRDE setup to measure pH *in situ* near the electrode surface. The pH increase during water and oxygen reduction were monitored and compared to theoretical values. To ensure that hydrogen peroxide, formed in the ORR, would not interfere with the pH response its influence on EIROFs was tested separately.

Care must be taken that the EIROF is brought into an oxidation state matching the chemical environment of the analyte. However, after a suitable potential conditioning no influence of H₂O₂ was observed. For use in the presence of different redox species (and concentrations), tests will be necessary. But these results do show that with suitable conditioning pH measurements with EIROF can be performed in redox active solutions.

Under near neutral conditionings the response time of the EIROF was too low, to allow potentiodynamic measurements. This has been attributed to the finite capacitance of the EIROF and the amount of protons or hydroxide ions necessary to equilibrate the film with the solution. Under near neutral conditions the concentration of either species is sufficiently low for mass transport to slow down the response.¹⁸ Reducing the capacitance of the film would improve the response under these conditions.

The titanium ring used as the EIROF substrate did not allow proper

conditioning at low potential, hindering measurements in a reducing environment. The choice for titanium was made because of better adhesion of the films, but gold would have been advantageous with respect to conditioning.

The measured pH was slightly higher than expected from calculations. More work is necessary to understand this behaviour. Meanwhile, practical application of the RRDE-pH method does not need to be hindered by this issue, since it can be circumvented by calibration of the RRDE with a known redox system.

8 Zinc oxide deposition

This final paper based chapter presents the work on ZnO deposition that initiated the studies presented in the previous 3 chapters. The chapter is based on Paper V.

8.1 Introduction

This PhD project started out with the intent of investigating the deposition of zinc oxide rods. This was initiated as a new research track within a then ongoing work that focussed on ZnO for application in, among others, LEDs. Initially, chemical growth methods were investigated, but soon attention shifted to electrochemical deposition. This chapter starts with a few results from chemical growth of ZnO rods to provide an impression of the deposits that can be obtained. Next, experiments on the electrodeposition of ZnO will be presented, with focus on the influence of current density on the deposits.

8.2 Chemical growth

Several methods exist to deposit zinc oxide rods. In this work hydrothermal growth, chemical bath deposition and electrodeposition were used. In both non-electrochemical methods silicon wafers, sometimes coated with gold, were heated in aqueous zinc solution for up to two hours at 90-95 °C.¹²² Hydrothermal growth was performed in closed bottles in an oven using a 0.1 M solution of ZnCl₂ adjusted to pH 10 with ammonia.¹⁹⁸ CBD was carried out from an equimolar solution of 25 mM Zn(NO₃)₂ and hexamine

(HMT) in a watch glass covered beaker on a hotplate. Both methods gave similar results.

A crucial factor determining the morphology of the deposits was the substrate and treatment thereof. On bare silicon or gold only scarce distributions of relatively large structures were obtained, Fig. 8.1. However, dense arrays of small ZnO rods were obtained on these otherwise unsuitable substrates by seeding their surface with ZnO.

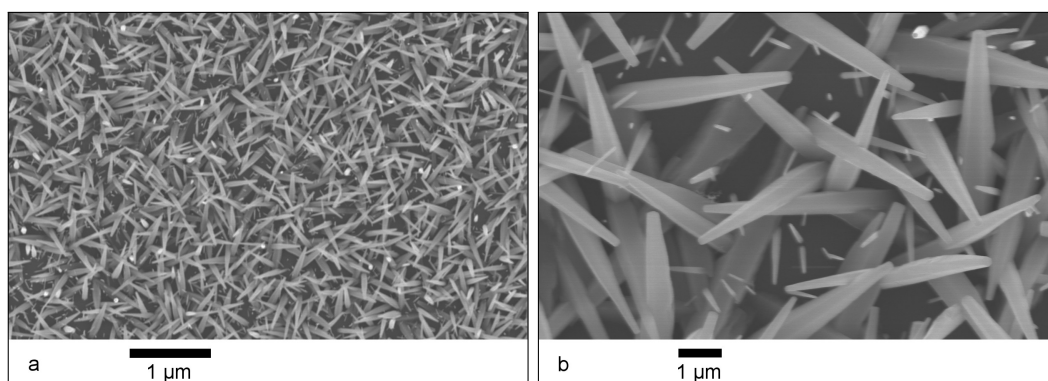


Figure 8.1: SEM images (15 kV) of ZnO prepared by chemical bath deposition on Au without seeding, at different magnification.

Two methods for seeding are commonly used, both described by Greene *et al.*^{199,200} The first involves colloidal ZnO from solution that is dried onto the substrate surface.¹⁹⁹ Seeding with colloids has the advantage of being a room temperature method, suitable for temperature sensitive substrates. A drawback however, is the poor alignment of the resulting rods. This issue is solved with the second method.²⁰⁰ Here, the substrate is first covered with a 5 mM solution of zinc acetate in absolute ethanol. Then it is rinsed with ethanol and heated to 250-300 °C to decompose zinc acetate particles deposited in the first step. This procedure is repeated 3 to 5 times. Results for both CBD and hydrothermal growth on silicon, seeded using method 2, can be seen in Fig. 8.2.

Even after seeding the role of the substrate is not completely subdued. Fig. 8.3b shows how growth on SiC, which has a lattice matches that of ZnO, yields similarly small but better aligned rods. Without seeding, growth on SiC yielded only a scarce distribution of large, micron sized, thick rods that were lying mostly flat on the surface, Fig 8.3a.

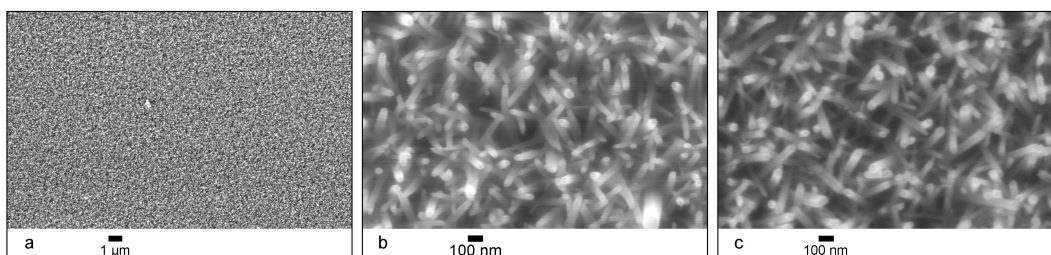


Figure 8.2: SEM images (15 kV) of ZnO, grown on seeded by (a) and (b) chemical bath deposition and (c) hydrothermal growth.

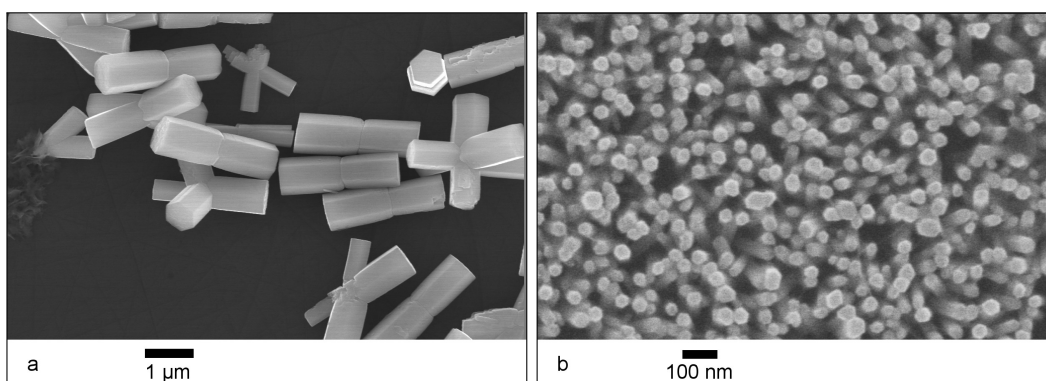


Figure 8.3: SEM images (15 kV) of ZnO deposited by chemical bath deposition on (a) bare and (b) seeded (ZnO) SiC.

Simplicity is a great advantage of both CBD and hydrothermal growth. Using a seeding procedure materials varying from silicon, metals or even polymers will suffice as a substrate for ZnO growth.^{199,200}

8.3 Electrodeposition

More direct control of the size and density of the deposits can be acquired using electrochemistry. On gold the nucleation density is much greater using electrodeposition than either of the two chemical methods just described. Consequently, small ZnO structures can be formed routinely without the need for seeding. The role of the substrate, however, is not entirely eliminated. For example, electrodeposition on bare silicon is more challenging than on gold.¹²⁷

The chemical foundation of this electrochemical growth method lies in the strong dependence of the solubility of ZnO on pH, discussed in Sec. 2.7.1. At room temperature it decreases from a molar to micromolar level upon changing pH from 6 to 9–10.⁵ In the electrodeposition of ZnO the deposition reaction itself is not of an electrochemical nature. Instead, an electrochemical reaction is used to induce hydrolysis and precipitation.

The deposition current density and surface pH are directly related, therefore a series of experiments was performed to determine how the morphology of the ZnO deposit depends on the current density. Depositions were carried out at 80 °C on gold RDEs (1000 rpm) under galvanostatic conditions for 45 min. The electrolyte consisted of 0.1 mM ZnCl₂ and 0.1 M KCl and was saturated with oxygen prior to starting the experiments. The deposition current density was varied from -0.03 mA cm^{-2} to -2.82 mA cm^{-2} . After finishing the deposition the electrodes were rinsed with Milli-Q water and allowed to dry.

8.3.1 Morphology

A series of high and low magnification SEM images was recorded (2 to 5 kV) to obtain information on the morphology of the deposits, Fig. 8.4 and 8.5. The SEM results from the experiment at -0.03 mA cm^{-2} are not included because no deposit was found.

The size and coverage density of the ZnO structures were measured using the ImageJ software.²⁰¹ Data on the diameters was obtained by measuring roughly 100 structures and the coverage was determined by counting areas containing approximately 300 structures. For the deposits obtained at -0.07 mA cm^{-2} and -0.14 mA cm^{-2} less structures were analysed as for those obtained at higher current densities, because of the low coverage. No coverage density was determined for these deposits because the values would strongly depend on the spots chosen for analysis. At higher current densities the electrode was uniformly covered, allowing information from small areas to be extrapolated to the entire surface. The results are summarised in Table 8.1,

Fig.8.4a and b show that at -0.07 mA cm^{-2} and -0.14 mA cm^{-2} the distribution of ZnO on the surface was nonuniform. The ZnO structures were mainly found around irregularities on the surface, indicating nucleation was not well facilitated, Fig 8.6b.

At -0.07 mA cm^{-2} large and very coarse ZnO structures were formed, seemingly made up from hexagonal platelets. The overall shape was hexagonal to some degree, but not well defined. Their interior was very smooth

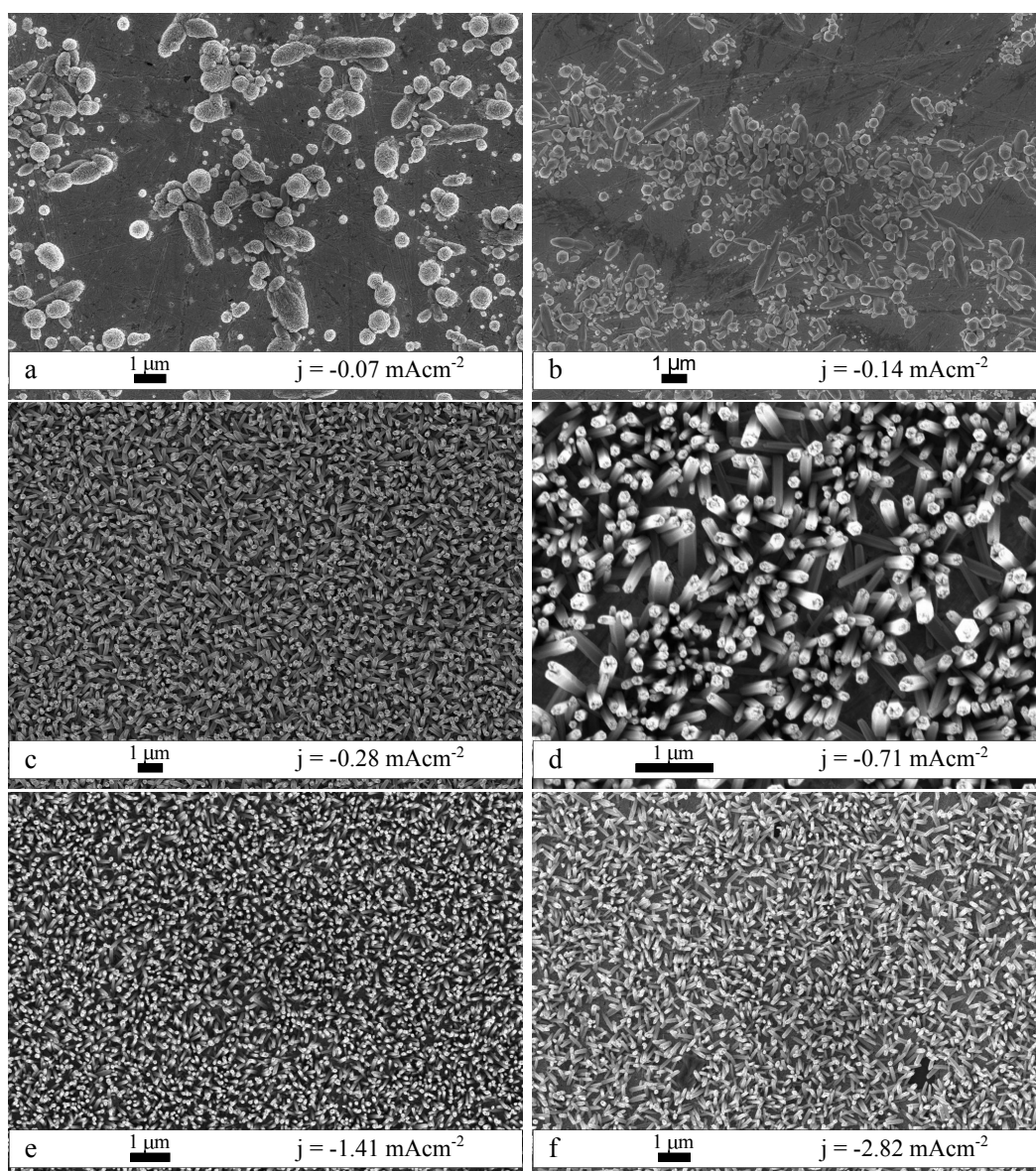


Figure 8.4: ZnO grown electrodeposited on gold at a constant current density of (a) -0.07 (b) -0.14 (c) -0.28 (d) -0.71 (e) -1.41 and (f) -2.82 mA cm^{-2}

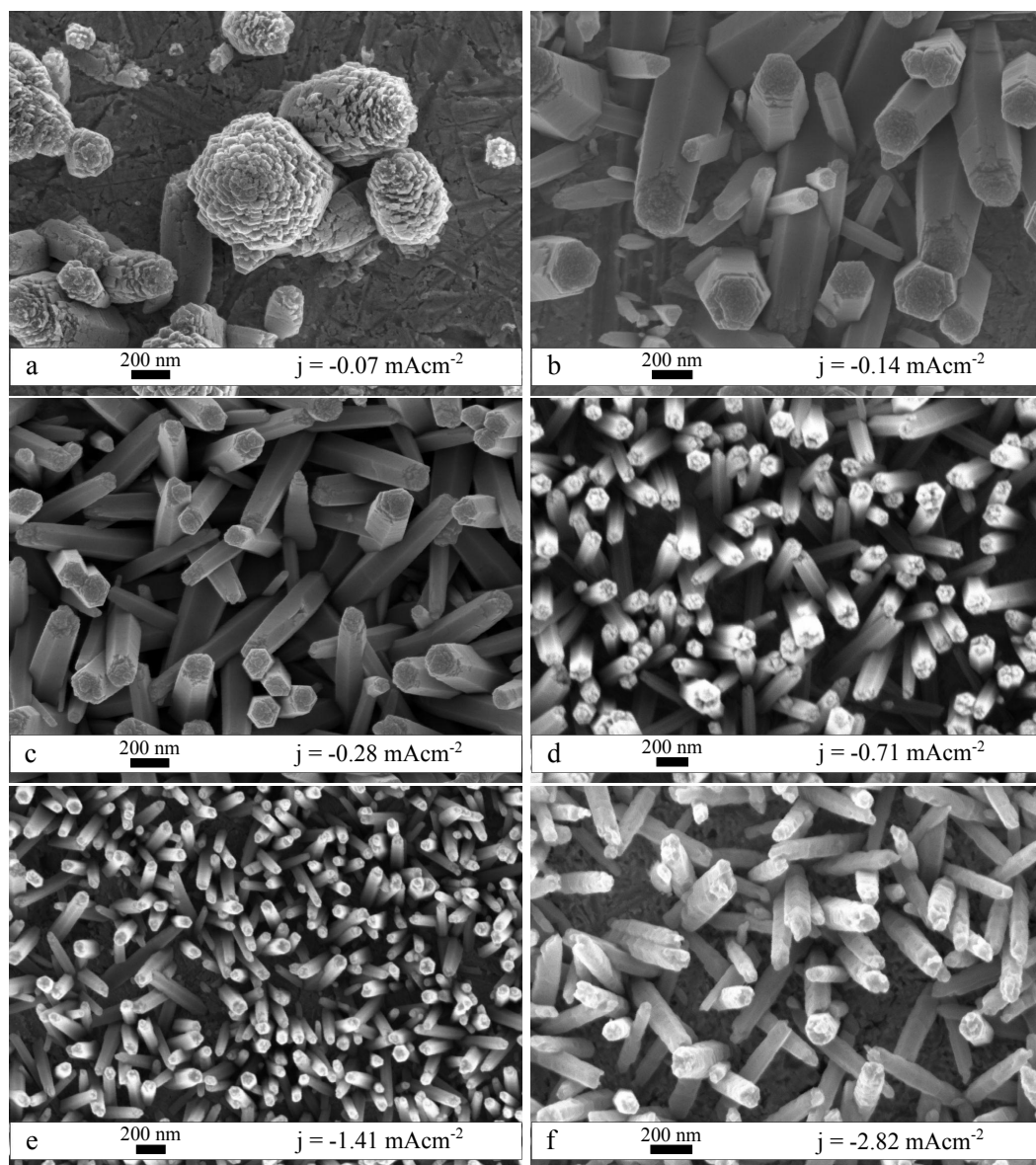


Figure 8.5: ZnO grown electrodeposited on gold at a constant current density of (a) -0.07 (b) -0.14 (c) -0.28 (d) -0.71 (e) -1.41 and (f) -2.82 mA cm^{-2}

Table 8.1: Diameters (average, minimum, maximum and standard deviation) and coverage density of ZnO grown at different current density, determined from Fig. 8.4 and 8.5.

j mA cm^{-2}	d nm	d_{\min} nm	d_{\max} nm	σ nm	density μm^{-2}
-0.07	537	213	1158	188	
-0.14	182	81	520	35	
-0.28	121	44	241	36	11
-0.71	122	63	193	24	20
-1.41	82	42	128	18	36
-2.82	96	50	198	22	19

compared with the surface, Fig 8.6b. At -0.14 mA cm^{-2} clearly hexagonal rods were formed and a large reduction in size was found. The size distribution was wide for both experiments.

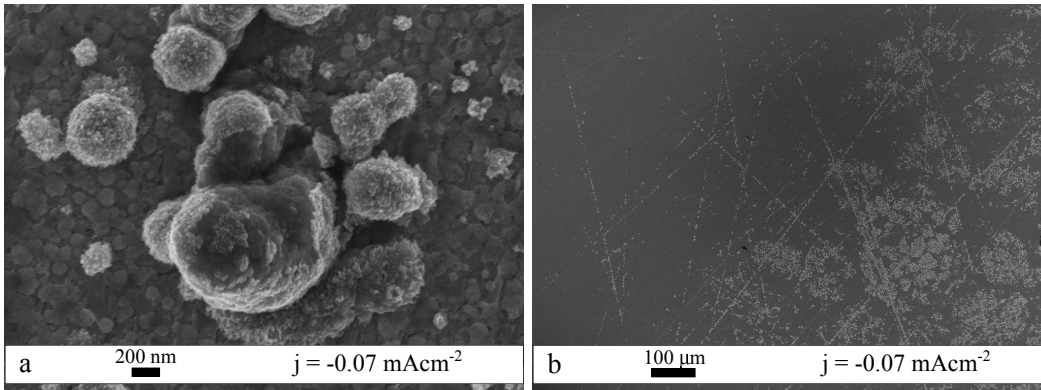


Figure 8.6: SEM images (5 kV) of ZnO deposited under the same conditions as Fig. 8.5a. (a) High magnification showing the smooth interior compared with the coarse exterior (b) Low magnification, showing the poor nucleation density at -0.07 mA cm^{-2} .

From -0.28 mA cm^{-2} up to -1.41 mA cm^{-2} smooth hexagonal ZnO rods were obtained. Furthermore, the deposit became increasingly dense, the rod size decreased and the size distribution became more narrow. At the highest current density tested, -2.82 mA cm^{-2} , the rod distribution became more

scarce again and the size and size distribution both increased. Additionally the rods looked to have started to dissolve.²⁰²

8.3.2 Deposition curves

The oxygen reduction reaction (ORR) was used to increase the surface pH and force ZnO deposition. On gold the ORR can involve 2 or 4 electron, Eq 8.1 and 8.2. At low overpotential the reduction stops at hydrogen peroxide, whereas at higher overpotential further reduction to hydroxide can proceed.



The limiting current density for an electrochemical reaction on a rotating disc electrode (RDE) is given by the Levich equation, Eq. 7.3.¹³⁸ At 80 °C the relevant physical constants, to calculate the limiting current density, are different from room temperature. The diffusion constants of oxygen, hydroxide ions and zinc ions are $5.31 \times 10^{-5} \text{ cm}^2 \text{ s}^{-1}$, $12.2 \times 10^{-5} \text{ cm}^2 \text{ s}^{-1}$, $2.5 \times 10^{-5} \text{ cm}^2 \text{ s}^{-1}$.^{203,204} The kinematic viscosity of water ν is reduced from $8.9 \times 10^{-3} \text{ cm}^2 \text{ s}^{-1}$ at 25 °C to $3.64 \times 10^{-3} \text{ cm}^2 \text{ s}^{-1}$ at 80 °C.¹⁷⁶ The oxygen solubility is merely 0.8 mM compared with 1.27 mM at room temperature.^{5,176}

Under these conditions the limiting current density, according to the Levich equation, equals 3.5 and 7.1 mA cm^{-2} for the 2 and 4 electron reaction, respectively. These values lie well within the limits of the values used for deposition. However, Goux *et al.* showed that the presence of zinc in solution strongly inhibits the ORR on ZnO electrodes.²⁰⁵

In the deposition curves in Fig. 8.7 the potential reaches its lowest value near -1.2 V . Under the present experimental condition the reduction of Zn^{2+} to metallic zinc can occur from -0.9 V vs NHE.¹³⁸ Furthermore, zinc stripping has been reported after scans to -1.0 V (vs SCE) under similar conditions.¹³⁵ It is therefore likely that zinc deposition took place at -2.82 mA cm^{-2} and even hydrogen evolution cannot be excluded.

For current densities more negative than -0.28 mA cm^{-2} the potential went through a minimum during the first minutes of the deposition. In potentiostatic deposition this feature was represented by a slowly increasing current density at the start of the deposition (not shown). The origin of this feature can be discussed in terms of the morphology of the deposits.

The formation of ZnO rods during electrodeposition has been proposed to be influenced by the relative diffusion rates of Zn^{2+} and OH^- .^{206,207}

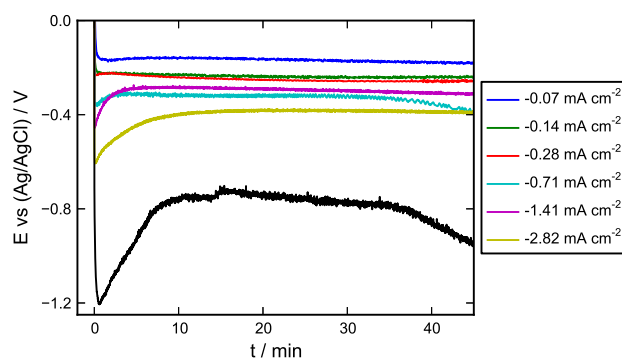


Figure 8.7: Potentiometric curves for ZnO deposition from 0.1 M KCl and 0.1 mM ZnCl₂ at 80 °C

As mentioned above, diffusion is about 5 times slower for zinc than for hydroxide ions. Diffusion of oxygen is approximately twice as fast as for zinc and in addition only one oxygen molecule is required for every two zinc ions. After the start of ZnO rod formation the surface would, therefore, be depleted of zinc and ZnO growth would mainly occur at the rod tips. Hence, in the interior of the rod forest less zinc would be available than at the start of the experiment. As a result, the ORR is less inhibited and the deposition current density can be maintained at less negative potentials.

8.3.3 Surface pH

Similar to the previous chapter, calculations were made to get an indication of the surface pH. Surface pH profiles were calculated using the theory described in Sec. 3.1.2 and more specifically Eq. 3.21.

Owing to enhanced diffusion and the lower autoprotolysis constant of water, the surface pH at 80 °C is lower than at room temperature, also the diffusion layer is more compact. For the calculations two cases were considered. First, near surface pH profiles, similar to Fig. 3.3, were calculated for the conditions used in the deposition experiments, not including ZnCl₂. The resulting profiles are shown in Fig. 8.8a. The grey horizontal line corresponds to the pH at which a ZnO solubility of 0.1 mM is reached.

Next, speciation calculations were performed for 0.1 mM ZnCl₂ in 0.1 M KCl at 80 °C for a range of starting pH values, using the SolGasWater software²⁰⁸ and thermodynamic data from Goux *et al.*⁴ The starting and final pH, obtained from these calculations, were used to calculate new surface pH profiles. This was done by taking the pH values in Fig. 8.8a

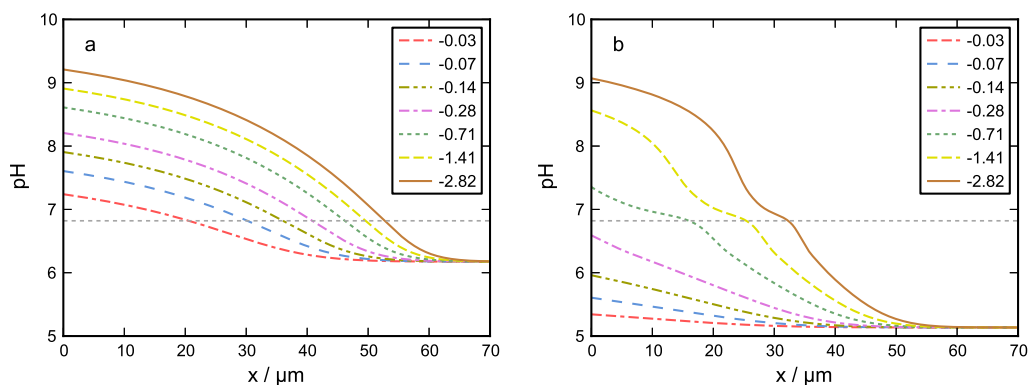


Figure 8.8: (a) Near surface pH at 80 °C, the profile was calculated according to the Levich model.¹³⁸ The numbers in the legend specify the current density in mA cm^{-2} . (b) pH profile in the diffusion layer after correction for the presence of ZnCl_2 .

as the starting values, and replacing them with the final values from the speciation calculations. The profiles, thus obtained, are shown in Fig. 8.8b. These profiles represent the pH near the surface under the experimental conditions used and assuming that no mass transport takes place.

According to Fig. 8.8b, at -0.28 mA cm^{-2} the solubility limit is almost reached. However, in the experiments deposition took place even at -0.07 mA cm^{-2} . Comparing Fig 8.8a and b the influence of zinc on the pH is largest for near neutral conditions. In addition, mass transport of oxygen is far from limiting at these current densities, *i.e.* there is still a concentration of oxygen at the surface. Fig. 8.4a and 8.5a show that the electrodes were not perfectly smooth. Hence, at the edges of scratches and pits, the current density can be enhanced, which could lead to suitable conditions for ZnO to precipitate. The tendency of the deposit to follow scratches can be seen in Fig. 8.6b.

At -0.28 mA cm^{-2} uniform coverage of rods was found. This current density is on the borderline for precipitation under the assumption of uniform zinc distribution, Fig. 8.8b. However, the experimental results clearly demonstrate that the zinc buffering capacity is smaller than expected, *i.e.* the zinc concentration at the surface is not constant and the pH can increase more than expected from Fig. 8.8b. For current densities down to -1.41 mA cm^{-2} the number of rods increases, which coincides with a reduced size of the individual rods. This would be due to the distribution of

the same amount of ZnO over more structures. As was shown by Peterson *et al.*²⁰⁹ there is a delicate balance between concentration and pH that impacts the efficiency of the growth. For electrodeposition this balance is between concentration and current density. Clearly at 2.82 mA cm^{-2} the optimum is passed, compare Fig. 8.5e and f.

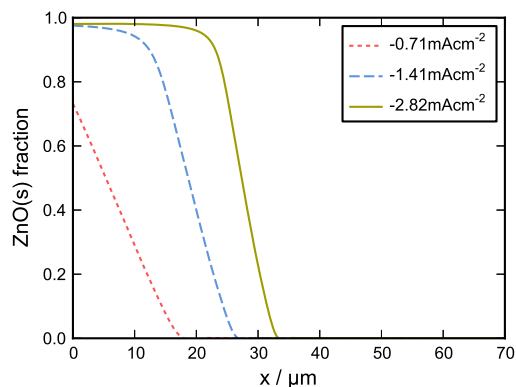


Figure 8.9: Solid ZnO fraction as a function of distance from the electrode surface according to the speciation, corresponding with Fig.8.8b

Initial thoughts on the poor quality of the ZnO rods grown at -2.82 mA cm^{-2} went to a possible overshoot in the pH. However, according to Fig. 8.8a this is not likely at 80°C . An alternative explanation is that at this current density homogeneous precipitation can occur away from the surface. For example, for -2.82 mA cm^{-2} approximately 50% of the zinc should precipitate at $30 \mu\text{m}$ from the surface, Fig 8.9. At $20 \mu\text{m}$ 98% of the zinc should be in the form of ZnO, locally depleting the solution from zinc, inducing dissolution of the rods.

8.4 Conclusions

ZnO rods were grown electrochemically from potassium chloride solutions at 80°C . The rod size and number of rods per unit area depends on the current density, at a given zinc concentration in solution. The current density and zinc concentration both influence the surface pH, responsible for the precipitation of ZnO on the electrode surface. An optimum in density was found at -1.41 mA cm^{-2} , for deposition from 0.1 M KCl , 0.1 mM ZnCl_2 at 1000 rpm . Past optimum conditions were explained on the basis of dissolution of ZnO, due to local depletion of dissolved zinc.

The potentiometric deposition curves exhibited a peak at the start of the depositions. This shape was explained in terms of relative diffusion rates of Zn^{2+} , O_2 and OH^- and the rod shaped morphology of the ZnO structures.

9 Conclusions and future work

In this chapter the conclusions from this thesis and the accompanying papers are presented. The chapter is concluded with a few suggestions for future work.

Starting as a tool iridium oxide turned into the central topic of this thesis. In order of appearance the EIROF related studies involved the deposition medium, pH sensing, electrochemical properties, and applications in RRDE-pH experiments.

Crystalline iridium oxide nanoparticles were found in TEM on EIROF samples and samples prepared from a dialysed deposition solution. It is likely though that non-particulate, multinuclear, iridium species also have a role in the deposition of EIROF. The oxidation of an oxalato complex as the deposition reaction, as has been suggested before, is unlikely. No oxidation of oxalate was detected on EIROFs and on gold this reaction was suppressed by iridium in solution. However, oxalate could have a role in stabilising iridium oxide nanoparticles in the solution.

Hydrogen peroxide was found to have a dual function in the preparation of the deposition solution. Initially under acidic conditions it acts as a reducing agent, but at a later stage under alkaline conditions, it functions as an oxidising agent. Carbonate was proposed to stabilise the system by minimising local pH fluctuations that could induce spontaneous precipitation of hydrous iridium oxide.

Experiments with EIROF deposited on gold, showed that the pH sensitivity of EIROF varies with the average oxidation state in a manner resembling the cyclic voltammogram. Maximum sensitivity was found after potential

conditioning near the first redox couple in the CV: a potential region of maximum redox buffer capacity. A second lower maximum was observed for conditioning potentials near the second couple, which also shows lower peak currents compared with the first. The relation between pH sensitivity and oxidation state was discussed in terms of mixed contributions from hydrous and anhydrous iridium oxide in the films.

The correlation between EIROF potential at pH 0 and the conditioning potential showed that beyond the first redox couple only about one third of the iridium sites is available for further oxidation. This effect was further addressed in the context of a recently formulated binuclear mechanism for the OER. The lower slope is interpreted as partial oxidation of Ir(IV), limited by nearest neighbour repulsion of the resulting Ir(V) sites. Thus, this redox process is divided into two steps: one preceding and one overlapping the oxygen evolution reaction (OER). It illustrates how hydrogen bonding suppresses the binuclear OER, implicitly favouring Ir(V) oxide formation above the thermodynamic onset potential for the OER at low pH.

Since, EIROFs are redox active, their interaction with redox species in solution could hinder pH measurements. Measurements on the influence of H_2O_2 on EIROF confirmed that this can indeed happen. However, for low concentrations the effect can be minimised by conditioning the electrode at a suitable potential. This can either be achieved actively, with a potentiostat, or passively, by equilibrating the electrode with the analyte prior to measurements.

The relation between oxidation state and pH sensitivities has two important consequences. First, as shown for H_2O_2 , the sensor can be optimised for specific solutions. Second, if a drift occurs in long term measurements the sensor can be “reset” to a well defined state, by fixing its potential at a known pH.

After studying their pH sensing behaviour, EIROF were successfully used in RRDE experiments to measure near surface pH during water and oxygen reduction. For this purpose titanium/gold RRDEs were used with EIROF electrodeposited on the ring. In terms of adhesion, titanium is an excellent substrate, however the EIROF/Ti system lacks electrochemical activity at low potentials. Compared with gold substrates, this reduces the pH sensitivity at low potentials and limits the potential range available for conditioning. Hence, depending on the application different substrates are favoured.

During the RRDE measurements, the pH sensing properties of the EIROF were more stable during the experiments on oxygen reduction than on water

reduction. This was explained by the more constant redox environment prior to and during the ORR experiments. In steady state measurements the response time of the EIROF was shown to be large at near neutral to mildly alkaline conditions. In LSV measurements this slow response resulted in a lag in the pH measured at the ring, relative to the disc current. In unbuffered solutions the concentration of hydroxide at intermediate pH is too low to immediately provide sufficient hydroxide to the film to reach an equilibrium. Mass transport, therefore, becomes a limiting factor for the response. Hence, for low disc current densities steady state measurements are recommended.

For both water and oxygen reduction the surface pH measured, indicated that slightly more than one hydroxide ion was formed per electron. The origin of this observation was not identified, but it is most likely related to non-ideal behaviour of the RRDE. However, calibration with a known redox system would facilitate the study of new reactions, so application is possible.

Finally, conclusions from the experiments that initiated the interest in near surface pH and iridium oxide *i.e.* electrodeposition of zinc oxide. Experimental results on the influence of current density on zinc oxide rod deposition on gold RDEs show a delicate relationship between current density and ZnO morphology. This was discussed within the context of complex formation in solution, solubility and surface pH. An optimum in coverage and a minimum diameter and size distribution was found at -1.41 mA cm^{-2} , for deposition from 0.1 M KCl, 0.1 mM ZnCl₂ at 1000 rpm.

9.1 Future work

The aim of this thesis was to measure near surface pH during electrochemical reactions. This idea got started with a question regarding the surface conditions during zinc oxide deposition. However, the concept of near surface pH measurements can be considered in much broader perspective than only the deposition of zinc oxide. Within the subject of electrodeposition, other compounds, such as iron, nickel and cobalt oxide or combination thereof, could be considered.

Other electrochemical systems, where protons are formed or consumed are of interest as well, such as corrosion, oxygen reduction hypochlorite oxidation and reduction, biomolecules etc. To study the reaction mechanism for such reactions, *in situ* pH measurements close to the electrode surface are invaluable.

Before RRDE-pH measurements can become a generally applicable tool, optimisation is still required. The main issue is the response time at small deviations from neutral pH. This problem could be solved in several ways. The mass transport limitations could, at least partly, be lifted by reducing the active volume of the film. This can be achieved, either by reducing the thickness of the film, or the dimensions of the ring.

A thinner ring would have the additional advantage of sampling a narrower region across the disc, improving the accuracy. A thinner disc-ring gap, would also be beneficial by reducing the area of the ring, but it would enhance the potential effects at the ring caused by the disc current.¹⁰² Since these potential effects are related to the disc current, this could be solved by replacing the disc with a ring, forming a rotating ring-ring electrode.²¹⁰ This would also give new challenges with regards to electrode construction.

Finally, alternative methods could be considered. The combination of RDEs with colorimetric or fluorescent pH sensing compounds might be an interesting concept. RDE would then be prepared with a, redox inactive, pH sensing material on the insulating parts of the electrode. Gradients in colour or fluorescence could then be measured during electrochemical experiments, to obtain information about the near surface pH.

Measurements at elevated temperatures are more demanding for the RRDE. The construction of electrodes that are sufficiently leak proof, even under heating, has proved challenging. Considering that even commercial high temperature RRDEs in PEEK are at a beta stage, there is work left to be done in this area.

Acknowledgements

Obviously, many people helped me out during my Ph.D., with advice, a push, a distraction and many other ways. Here I would like to express my gratitude to all those people.

A special thanks to Elisabet, for taking me into the electrochemistry group and for picking up the task of becoming my supervisor, when the position “became available”.

I am also grateful to the platform Nanoparticles in Interactive Environments for making it possible to do my Ph.D. in Gothenburg and for picking a great group of colleagues. The adventures we had in the Far East, are among the best memories from my time in Gothenburg.

All past and present members of the electrochemistry group, it was really good working with all of you. Thanks for all the discussions, support, after work, etc. . . .

Bea, you helped me out a lot when I first got started as a Ph.D. student in Gothenburg and you found me a place to live during my final weeks. Thank you.

Esa, thanks for all the technical support and especially for making all my electrodes, often at very/too short notice.

Lennart, thank you for being my examiner and for many enjoyable afternoons teaching the old fashioned craftsmanship of inorganic chemistry.

Peter and Krzysztof, it was really nice having you as my group mates during my first years in Sweden.

Itai and Qiu-Hong, I enjoyed all our lively discussions about science, politics, Esscher, Esscher, more Esscher and other topics.

Thanks to the people who helped me out with experiments: Moheb, Jenny, Jaenette, for the DLS measurements and Leif and Nikolina, for the TEM measurements.

A shout out, to my fellow rink rats, The Mighty Ducks, for many intense and fun ice hockey games. Too bad in Belgium, hockey is mostly played, wearing shoes.

Annick, thanks for giving me the opportunity to work on new challenges in Brussels, while wrapping up my Ph.D.

To all my friends and colleagues in Brussels, thx for the “occasional” reminder to go home and work (or not to).

And last but not least, my family: Mom, Dad, Vivianne, Tom, and Milo. Thank you, for always being there for me.

Bibliography

- [1] Peulon, S.; Lincot, D. *Advanced Materials* **1996**, *8*, 166–169.
- [2] Izaki, M.; Omi, T. *Applied Physics Letters* **1996**, *68*, 2439–2440.
- [3] Limmer, S.; Kulp, E.; Switzer, J. *Langmuir* **2006**, *22*, 10535–10539.
- [4] Goux, A.; Pauporte, T.; Chivot, J.; Lincot, D. *Electrochimica Acta* **2005**, *50*, 2239–2248.
- [5] Peulon, S.; Lincot, D. *Journal of the Electrochemical Society* **1998**, *145*, 864–874.
- [6] Pauporté, T.; Lincot, D. *Journal of the Electrochemical Society* **2001**, *148*, C310–C314.
- [7] Yu. V. P.; Filinovskii, V. In *The Rotating Disc Electrode*; Wroblowa, H., Conway, B., Eds.; Consultants Bureau New York, 1976.
- [8] Slowinska, K.; Majda, M. *Journal of Solid State Electrochemistry* **2004**, *8*, 763–771hydrous oxi.
- [9] Albery, W.; Calvo, E. *Journal of the Chemical Society, Faraday Transactions I* **1983**, *79*, 2583–2596.
- [10] Albery, W. *Transactions of the Faraday Society* **1966**, *62*, 1915–1919.
- [11] Levich, V. *Physicochemical hydrodynamics*; Prentice Hall, 1962.
- [12] Wroblowa, H. S.; Chi-Pan, Y.; Razumney, G. *Journal of Electroanalytical Chemistry and Interfacial Electrochemistry* **1976**, *69*, 195–201.

- [13] Albery, W.; Mount, A. *Journal of the Chemical Society, Faraday Transactions I* **1989**, *85*, 1181–1188.
- [14] Albery, W.; Mount, A. *Journal of the Chemical Society, Faraday Transactions I* **1989**, *85*, 1189–1198.
- [15] Albery, W.; Mount, A. *Journal of the Chemical Society, Faraday Transactions I* **1989**, *85*, 3717–3724.
- [16] Yamanaka, K. *Japanese Journal of Applied Physics* **1989**, *28*, 632–637.
- [17] Marzouk, S. *Analytical Chemistry* **2003**, *75*, 1258–1266.
- [18] Elsen, H. A.; Monson, C. F.; Majda, M. *Journal of the Electrochemical Society* **2009**, *156*, F1–F6.
- [19] Burke, L.; Mulcahy, J.; Whelan, D. *Journal of Electroanalytical Chemistry* **1984**, *163*, 117–128.
- [20] Griffith, W. *Platinum Metals Review* **2003**, *47*, 175–183.
- [21] Griffith, W. *Platinum Metals Review* **2004**, *48*, 182–189.
- [22] Tennant, S. *Philosophical Transactions of the Royal Society of London* **1804**, *94*, 411–418.
- [23] Hunt, L. *Platinum Metals Review* **1987**, *31*, 32–41.
- [24] Davy, H. *Philosophical Transactions of the Royal Society of London* **1808**, *98*, 1–44.
- [25] Children, J. *Philosophical Transactions of the Royal Society of London* **1815**, *105*, 363–374.
- [26] Yao, S.; Wang, M.; Madou, M. *Journal of the Electrochemical Society* **2001**, *148*, H29–H36.
- [27] Usselmans, C., Melvyn *Platinum Metals Review* **1978**, *22*, 100–106.
- [28] Wollaston, W. *The Philosophical Magazine, or Annals of Chemistry, Mathematics, Astronomy, Natural History, and General Science* **1829**, *6*, 1–8.
- [29] Zhao, Y.; Hernandez-Pagan, E. A.; Vargas-Barbosa, N. M.; Dysart, J. L.; Mallouk, T. E. *The Journal of Physical Chemistry Letters* **2011**, *2*, 402–406.

- [30] Bestaoui, N.; Prouzet, E. *Chemistry of Materials* **1997**, *9*, 1036–1041.
- [31] Yoshino, T.; Baba, N.; Arai, K. *Japanese Journal of Applied Physics* **1987**, *26*, 1547–.
- [32] Gottesfeld, S.; Srinivasan, S. *Journal of Electroanalytical Chemistry* **1978**, *86*, 89–104.
- [33] Burke, L. D.; O'Sullivan, E. J. *Journal of Electroanalytical Chemistry* **1981**, *117*, 155–160.
- [34] Kang, K.; Shay, J. *Journal of the Electrochemical Society* **1983**, *130*, 766–769.
- [35] Katsube, T.; Lauks, I.; Zemel, J. *Sensors and Actuators* **1982**, *2*, 399–410.
- [36] Patil, P.; Kwar, R.; Sadale, S. *Electrochimica Acta* **2005**, *50*, 2527–2532.
- [37] Ardizzone, S.; Carugati, A.; Trasatti, S. *Journal of Electroanalytical Chemistry and Interfacial Electrochemistry* **1981**, *126*, 287–292.
- [38] Kim, S.; Kwon, S.; Kwak, D.; Kang, S. *Journal of Applied Physics* **2008**, *103*, 023517–023517.
- [39] Lodi, G.; De Battisti, A.; Bordin, G.; De Asmundis, C.; Benedetti, A. *Journal of Electroanalytical Chemistry* **1990**, *277*, 139–150.
- [40] Burke, L. *Platinum Metals Review* **1984**, *28*, 56–61.
- [41] Hackwood, S.; Dayem, A.; Beni, G. *Physical Review B* **1982**, *26*, 471.
- [42] Yagi, M.; Tomita, E.; Sakita, S.; Kuwabara, T.; Nagai, K. *The Journal of Physical Chemistry B* **2005**, *109*, 21489–21491.
- [43] Duo, I.; Michaud, P.-A.; Haenni, W.; Perret, A.; Comninellis, C. *Electrochemical and Solid-State Letters* **2000**, *3*, 325–326.
- [44] Nakagawa, T.; Beasley, C.; Murray, R. *The Journal of Physical Chemistry C* **2009**, *113*, 12958–12961.
- [45] Beni, G.; Schiavone, L. M.; Shay, J. L.; Dautremont-Smith, W. C.; Schneider, B. S. *Nature* **1979**, *282*, 281–283.
- [46] Kamegaya, Y.; Sasaki, K.; Oguri, M.; Asaki, T.; Kobayashi, H.; Mitamura, T. *Electrochimica Acta* **1995**, *40*, 889–895.

- [47] Hackwood, S.; Schiavone, L.; Dautremont-Smith, W.; Beni, G. *Journal of the Electrochemical Society* **1981**, *128*, 2569–2573.
- [48] Fierro, S.; Nagel, T.; Baltruschat, H.; Comninellis, C. *Electrochemistry Communications* **2007**, *9*, 1969–1974.
- [49] Burke, L. D.; Lyons, M. E. *Modern aspects of electrochemistry* **1986**, *18*, 169–248.
- [50] Gottesfeld, S. *Journal of the Electrochemical Society* **1980**, *127*, 272–277.
- [51] O’Sullivan, E. J.; Burke, L. D. *Journal of the Electrochemical Society* **1990**, *137*, 466–471.
- [52] Burke, L.; Roche, M. *Journal of Electroanalytical Chemistry and Interfacial Electrochemistry* **1984**, *164*, 315–334.
- [53] Buckley, D.; Burke, L. *Journal of the Chemical Society, Faraday Transactions I* **1975**, *71*, 1447–1459.
- [54] Burke, L.; Nugent, P. *Gold Bulletin* **1997**, *30*, 43–53.
- [55] Conway, B.; Mozota, J. *Electrochimica Acta* **1983**, *28*, 9–16.
- [56] Pickup, P.; Birss, V. *Journal of Electroanalytical Chemistry* **1987**, *220*, 83–100.
- [57] Olthuis, W.; Robben, M.; Bergveld, P.; Bos, M.; Van der Linden, W. *Sensors and Actuators, B: Chemical* **1990**, *2*, 247–256.
- [58] Terashima, C.; Rao, T.; Sarada, B.; Spataru, N.; Fujishima, A. *Journal of Electroanalytical Chemistry* **2003**, *544*, 65–74.
- [59] Meyer, R.; Cogan, S.; Nguyen, T.; Rauh, R. *IEEE Transactions on Neural Systems and Rehabilitation Engineering* **2001**, *9*, 2–11.
- [60] Lu, Y.; Wang, T.; Cai, Z.; Cao, Y.; Yang, H.; Duan, Y. *Sensors and Actuators, B: Chemical* **2009**, *137*, 334–339.
- [61] Mozota, J.; Conway, B. *Electrochimica Acta* **1983**, *28*, 1–8.
- [62] Emsley, J. *Nature’s Building Blocks: An A-Z Guide to the Elements*; Oxford University Press, USA, 2011.

- [63] Earnshaw, A.; Greenwood, N. *Chemistry of the Elements, Second Edition*; Butterworth-Heinemann, 1997.
- [64] McIntyre, J. D. E.; Peck, W. F., Jr.; Nakahara, S. *Journal of the Electrochemical Society* **1980**, *127*, 1264–1268.
- [65] Yano, J.; Noguchi, K.; Yamasaki, S.; Yamazaki, S. *Electrochemistry Communications* **2004**, *6*, 110–114.
- [66] Sziraki, L.; Bobics, L. *Electrochimica Acta* **2002**, *47*, 2189–2197.
- [67] Chen, Y.; Taylor, P.; Scherson, D. *Journal of the Electrochemical Society* **2009**, *156*, F14–F21.
- [68] Gottesfeld, S.; McIntyre, J. D. E.; Beni, G.; Shay, J. L. *Applied Physics Letters* **1978**, *33*, 208–210.
- [69] Yamanaka, K. *Japanese journal of applied physics* **1991**, *30*, 1285–1289.
- [70] Mortimer, R. J.; Dyer, A. L.; Reynolds, J. R. *Displays* **2006**, *27*, 2–18.
- [71] Baur, J.; Spaine, T. *Journal of Electroanalytical Chemistry* **1998**, *443*, 208–216.
- [72] Elsen, H. A. Thermodynamic and Dynamic Investigations of Hydrated Iridium Oxide Potentiometric pH Micro-Sensors. Ph.D. thesis, University of California Berkeley, 2007.
- [73] Harriman, A.; Thomas, J.; Milward, G. *New Journal of Chemistry* **1987**, *11*, 757–762.
- [74] Castillo-Blum, S. E.; Richens, D. T.; Sykes, A. G. *Journal of the Chemical Society, Chemical Communications* **1986**, 1120–1121.
- [75] Castillo-Blum, S. E.; Richens, D. T.; Sykes, A. G. *Inorganic Chemistry* **1989**, *28*, 954–960.
- [76] Hoertz, P.; Kim, Y.; Youngblood, W.; Mallouk, T. *Journal of Physical Chemistry B* **2007**, *111*, 6845–6856.
- [77] Wöhler, L.; Witzmann, W. *Zeitschrift für anorganische Chemie* **1908**, *57*, 323–352.

- [78] Desideri, P.; F., P. *La Ricerca Scientifica, Serie II, Rendiconti, Sezione A* **1961**, *1*, 265–270.
- [79] Kolb, D. In *Spectroelectrochemistry: theory and practice*; Gale, R. J., Ed.; Plenum Press, New York, 1988.
- [80] Nakagawa, T.; Bjorge, N.; Murray, R. *Journal of the American Chemical Society* **2009**, *131*, 15578–15579.
- [81] Kwon, S. J.; Fan, F.-R. F.; Bard, A. J. *Journal of the American Chemical Society* **2010**, *132*, 13165–13167.
- [82] Kwon, S. J.; Zhou, H.; Fan, F.-R. F.; Vorobyev, V.; Zhang, B.; Bard, A. J. *Physical Chemistry Chemical Physics* **2011**, *13*, 5394–5402.
- [83] Kirkbright, G.; Narayanaswamy, R.; Welti, N. *Analyst* **1984**, *109*, 1025–1028.
- [84] Chen, H.; Wang, X.; Song, X.; Zhou, T.; Jiang, Y.; Chen, X. *Sensors and Actuators B: Chemical* **2010**, *146*, 278–282.
- [85] Jin, Z.; Su, Y.; Duan, Y. *Sensors and Actuators B: Chemical* **2000**, *71*, 118–122.
- [86] Steinhoff, G.; Hermann, M.; Schaff, W.; Eastman, L.; Stutzmann, M.; Eickhoff, M. *Applied Physics Letters* **2003**, *83*, 177–179.
- [87] Heo, Y.; Tien, L.; Kwon, Y.; Norton, D.; Pearton, S.; Kang, B.; Ren, F. *Applied Physics Letters* **2004**, *85*, 2274–2276.
- [88] Głab, S.; Hulanicki, A.; Edwall, G.; Ingman, F. *Critical Reviews in Analytical Chemistry* **1989**, *21*, 29–47.
- [89] López-Alonso, M.; Moya, M.; Cabo, J.; Ribas, J.; del Carmen Macías, M.; Silny, J.; Sifrim, D. *Pediatrics* **2006**, *118*, e299–e308.
- [90] Stock, J. T.; Purdy, W. C.; Garcia, L. M. *Chemical Reviews* **1958**, *58*, 611–626.
- [91] Kinoshita, E.; Ingman, F.; Edwall, G.; Thulin, S.; Głab, S. *Talanta* **1986**, *33*, 125–134.
- [92] Fog, A.; Buck, R. P. *Sensors and Actuators* **1984**, *5*, 137–146.

- [93] Yuen, M.; Lauks, I.; Dautremont-Smith, W. *Solid State Ionics* **1983**, *11*, 19–29.
- [94] Olthuis, W.; Van KerKhof, J.; Bergveld, P.; Bos, M.; van der Linden, W. *Sensors and Actuators B: Chemical* **1991**, *4*, 151–156.
- [95] Hitchman, M.; Ramanathan, S. *Analyst* **1988**, *113*, 35–9.
- [96] Kötzt, R.; Neff, H.; Stucki, S. *Journal of the Electrochemical Society* **1984**, *131*, 72–77.
- [97] Bernasconi, L.; Baerends, E. J.; Sprik, M. *Journal of Physical Chemistry B* **2006**, *110*, 11444–11453.
- [98] Parks, G. A. *Chemical Reviews* **1965**, *65*, 177–198.
- [99] Marzouk, S.; Ufer, S.; Buck, R.; Johnson, T.; Dunlap, L.; Cascio, W. *Analytical Chemistry* **1998**, *70*, 5054–5061.
- [100] Zhang, J.; Lin, C.; Feng, Z.; Tian, Z. *Journal of Electroanalytical Chemistry* **1998**, *452*, 235–240.
- [101] Carroll, S.; Baldwin, R. P. *Analytical Chemistry* **2010**, *82*, 878–885.
- [102] Hessami, S.; Tobias, C. *AIChE Journal* **1993**, *39*, 149–162.
- [103] Wang, Z. *Journal of Physics: Condensed Matter* **2004**, *16*, 829–858.
- [104] Izaki, M.; Omi, T. *Journal of the Electrochemical Society* **1997**, *144*, 1949–1952.
- [105] McCune, M.; Zhang, W.; Deng, Y. *Nano Letters* **2012**, *12*, 3656–3662.
- [106] Gal, D.; Hodes, G.; Lincot, D.; Schock, H. W. *Thin Solid Films* **2000**, *361-362*, 79–83.
- [107] Bao, J.; Zimmerler, M. A.; Capasso, F.; Wang, X.; Ren, Z. F. *Nano Letters* **2006**, *6*, 1719–1722.
- [108] Nadarajah, A.; Word, R. C.; Meiss, J.; Konenkamp, R. *Nano Letters* **2008**, *8*, 534–537.
- [109] Lupan, O.; Pauporté, T.; Viana, B.; Tiginyanu, I. M.; Ursaki, V. V.; Cortès, R. *ACS Applied Materials and Interfaces* **2010**, *2*, 2083–2090.

- [110] Huang, M.; Mao, S.; Feick, H.; Yan, H.; Wu, Y.; Kind, H.; Weber, E.; Russo, R.; Yang, P. *Science* **2001**, *292*, 1897–1899.
- [111] Zhu, H.; Shan, C.-X.; Yao, B.; Li, B.-H.; Zhang, J.-Y.; Zhang, Z.-Z.; Zhao, D.-X.; Shen, D.-Z.; Fan, X.-W.; Lu, Y.-M.; Tang, Z.-K. *Advanced Materials* **2009**, *21*, 1613–1617.
- [112] Beek, W.; Wienk, M.; Janssen, R. *Advanced Materials* **2004**, *16*, 1009–1013.
- [113] Bashir, A.; Wöbkenberg, P. H.; Smith, J.; Ball, J. M.; Adamopoulos, G.; Bradley, D. D. C.; Anthopoulos, T. D. *Advanced Materials* **2009**, *21*, 2226–2231.
- [114] Chatterjee, A.; Mitra, P.; Mukhopadhyay, A. **1999**, *34*, 4225–4231–.
- [115] Paraguay D., F.; Miki-Yoshida, M.; Morales, J.; Solis, J.; Estrada L., W. *Thin Solid Films* **2000**, *373*, 137–140.
- [116] Klason, P.; Magnusson, K.; Nur, O.; Zhao, Q. X.; Wahab, Q. U.; Willander, M. *Physica Scripta* **2006**, *T126*, 53–56.
- [117] Yi, G.-C.; Wang, C.; Park, W. I. *Semiconductor Science and Technology* **2005**, *20*, S22–S34.
- [118] Lyu, S. C.; Zhang, Y.; Lee, C. J. *Chemistry of Materials* **2003**, *15*, 3294–3299.
- [119] Liu, B.; Zeng, H. C. *Journal of the American Chemical Society* **2003**, *125*, 4430–4431.
- [120] Wang, Y.; Li, M. *Materials Letters* **2006**, *60*, 266–269.
- [121] Greene, L. E.; Yuhas, B. D.; Law, M.; Zitoun, D.; Yang, P. *Inorganic Chemistry* **2006**, *45*, 7535–7543.
- [122] Vayssieres, L.; Keis, K.; Lindquist, S.-E.; Hagfeldt, A. *Journal of Physical Chemistry B* **2001**, *105*, 3350–3352.
- [123] Mills, B. 2013; <https://commons.wikimedia.org/wiki/File:Zincite-3D-balls.png>.
- [124] Gao, Y.; Wang, Z. *Nano Letters* **2007**, *7*, 2499–2505.

- [125] Li, W.; Shi, E.; Zhong, W.; Yin, Z. *Journal of Crystal Growth* **1999**, *203*, 186–196.
- [126] Pauporté, T.; Jirka, I. *Electrochimica Acta* **2009**, *54*, 7558–7564.
- [127] Könenkamp, R.; Word, R.; Dosmailov, M.; Meiss, J.; Nadarajah, A. *Journal of Applied Physics* **2007**, *102*, 056103–056103–3.
- [128] Pauporté, T.; Lincot, D. *Applied Physics Letters* **1999**, *75*, 3817–3819.
- [129] Pauporté, T.; Lincot, D.; Viana, B.; Pellé, F. *Applied Physics Letters* **2006**, *89*, 233112–233112–3.
- [130] Canava, B.; Lincot, D. *Journal of Applied Electrochemistry* **2000**, *30*, 711–716.
- [131] Elias, J.; Tena-Zaera, R.; Lévy-Clément, C. *Thin Solid Films* **2007**, *515*, 8553–8557.
- [132] Govender, K.; Boyle, D.; Kenway, P.; O'Brien, P. *Journal of Materials Chemistry* **2004**, *14*, 2575–2591.
- [133] Sounart, T.; Liu, J.; Voigt, J.; Hsu, J.; Spoerke, E.; Tian, Z.; Jiang, Y. *Advanced Functional Materials* **2006**, *16*, 335–344.
- [134] Tian, Z. R.; Voigt, J. A.; Liu, J.; McKenzie, B.; McDermott, M. J.; Rodriguez, M. A.; Konishi, H.; Xu, H. *Nature Materials* **2003**, *2*, 821–826.
- [135] Elias, J.; Tena-Zaera, R.; Lévy-Clément, C. *Journal of Physical Chemistry C* **2008**, *112*, 5736–5741.
- [136] Tena-Zaera, R.; Elias, J.; Lévy-Clément, C. *Proceedings of SPIE* **2007**, *6650*, 66500A–1–66500A–11.
- [137] Tena-Zaera, R.; Elias, J.; Lévy-Clément, C.; Bekeny, C.; Voss, T.; Mora-Seró, I.; Bisquert, J. *Journal of Physical Chemistry C* **2008**, *112*, 16318–16323.
- [138] Faulkner, L.; Bard, A. *Electrochemical Methods Fundamentals and Applications*; John Wiley & Sons, 2001.
- [139] Bockris, J. O.; Reddy, A. K.; Gamboa-Aldeco, M. E. *Modern Electrochemistry 2A: Fundamentals of Electrodeics*; Springer, 2001.

- [140] Laviron, E. *Journal of Electroanalytical Chemistry and Interfacial Electrochemistry* **1980**, *112*, 1–9.
- [141] Brown, A. P.; Anson, F. C. *Analytical Chemistry* **1977**, *49*, 1589–1595.
- [142] Honeychurch, M. J.; Rechnitz, G. A. *Electroanalysis (New York)* **1998**, *10*, 285–293.
- [143] Honeychurch, M. J.; Rechnitz, G. A. *Electroanalysis (New York)* **1998**, *10*, 453–457.
- [144] Kötz, R.; Barbero, C.; Haas, O. *Journal of Electroanalytical Chemistry* **1990**, *296*, 37–49.
- [145] Birss, V.; Elzanowska, H.; Gottesfeld, S. *Journal of Electroanalytical Chemistry* **1991**, *318*, 327–333.
- [146] Bock, C.; Birss, V. *Journal of Electroanalytical Chemistry* **1999**, *475*, 20–27.
- [147] He, P. *Analytical Chemistry* **1995**, *67*, 986–992.
- [148] Penczek, M.; Stojek, Z.; Buffle, J. *Journal of Electroanalytical Chemistry and Interfacial Electrochemistry* **1989**, *270*, 1–6.
- [149] Albery, W.; Hitchman, M. *Transactions of the Faraday Society* **1971**, *67*, 2408–2413.
- [150] Karman, T. v. *Zeitschrift für Angewandte Mathematik und Mechanik* **1921**, *1*, 233–252.
- [151] Cochran, W. G. *Mathematical Proceedings of the Cambridge Philosophical Society* **1934**, *30*, 365–375.
- [152] Albery, W.; Hitchman, M. *Ring-Disc Electrodes*; Clarendon Press London, 1971.
- [153] Tourwé, E.; Pintelon, R.; Hubin, A. *Journal of Electroanalytical Chemistry* **2006**, *594*, 50–58.
- [154] Tourwé, E.; Breugelmans, T.; Pintelon, R.; Hubin, A. *Journal of Electroanalytical Chemistry* **2007**, *609*, 1–7.
- [155] Parys, H. V.; Tourwé, E.; Breugelmans, T.; Depauw, M.; Deconinck, J.; Hubin, A. *Journal of Electroanalytical Chemistry* **2008**, *622*, 44–50.

- [156] Prater, K. B.; Bard, A. J. *Journal of the Electrochemical Society* **1970**, *117*, 335–340.
- [157] Prater, K. B.; Bard, A. J. *Journal of the Electrochemical Society* **1970**, *117*, 207–213.
- [158] Prater, K. B.; Bard, A. J. *Journal of the Electrochemical Society* **1970**, *117*, 1517–1520.
- [159] Van den Bossche, B.; Bortels, L.; Deconinck, J.; Vandeputte, S.; Hubin, A. *Journal of Electroanalytical Chemistry* **1995**, *397*, 35–44.
- [160] Parys Van, H.; Teliás, G.; Nedashkivskyi, V.; Mollay, B.; Vandendael, I.; Van Damme, S.; Deconinck, J.; Hubin, A. *Electrochimica Acta* **2010**, *55*, 5709–5718.
- [161] Alexiadis, A.; Cornell, A.; Dudukovic, M. *Journal of Electroanalytical Chemistry* **2012**, *669*, 55–66.
- [162] H., H. C.; R., R. *Principles of Colloid and Surface Chemistry 3rd ed.*; CRC Taylor & Francis, 1997.
- [163] Goldstein, I.; Newbury, D.; Echlin, P.; Joy, D.; Lyman, E.; E., L.; Sawyer, L.; J.R., M. *Scanning Electron Microscopy and X-Ray Microanalysis*; Springer, 2003.
- [164] Sawyer, D. T.; Sobkowiak, A.; Roberts, J. L. *Electrochemistry for Chemists, 2ed.*; Wiley-Interscience, 1995.
- [165] Poulsen, I.; Garner, C. *Journal of the American Chemical Society* **1962**, *84*, 2032–2037.
- [166] Petrovic, S. *The Chemical Educator* **2000**, *5*, 231–235.
- [167] Kruszyna, H.; Bodek, I.; Libby, L.; Milburn, R. *Inorganic Chemistry* **1974**, *13*, 434–438.
- [168] Cota, H. M.; Katan, T.; Chin, M.; Schoenweis, F. J. *Nature* **1964**, *203*, 1281–1281.
- [169] Petit, M.; Plichon, V. *Journal of Electroanalytical Chemistry* **1998**, *444*, 247–252.

- [170] Chen, T.; Hung, J.; Pan, F.; Chang, L.; Wu, S.; Tien, T. *Journal of Nanoscience and Nanotechnology* **2009**, *9*, 3264–3268.
- [171] ICDD **2011**, PDF-4 03-065-2822.
- [172] Viskari, L.; Stiller, K. *Ultramicroscopy* **2011**, *111*, 652–658.
- [173] Steegstra, P.; Ahlberg, E. *Electrochimica Acta* **2012**, *76*, 26–33.
- [174] Steegstra, P.; Busch, M.; Panas, I.; Ahlberg, E. *Manuscript* **2013**,
- [175] Britton, H.; Robinson, R. *Journal of the Chemical Society* **1931**, 1456–1462.
- [176] *CRC Handbook of Chemistry and Physics, 92nd Ed.*; CRC Press, 2011.
- [177] Mo, Y.; Stefan, I. C.; Cai, W.-B.; Dong, J.; Carey, P.; Scherson, D. A. *Journal of Physical Chemistry B* **2002**, *106*, 3681–3686.
- [178] Pearson, R. G. *Inorganic Chemistry* **1988**, *27*, 734–740.
- [179] Butler, M. A.; Ginley, D. S. *Journal of the Electrochemical Society* **1978**, *125*, 228–232.
- [180] Ardizzone, S.; Lettieri, D.; Trasatti, S. *Journal of Electroanalytical Chemistry and Interfacial Electrochemistry* **1983**, *146*, 431–437.
- [181] Yoon, R. H.; Salman, T.; Donnay, G. *Journal of Colloid and Interface Science* **1979**, *70*, 483–493.
- [182] Kosmulski, M. *Advances in Colloid and Interface Science* **2009**, *152*, 14–25.
- [183] Lervik, I. A.; Tsyppkin, M.; Owe, L.-E.; Sunde, S. *Journal of Electroanalytical Chemistry* **2010**, *645*, 135–142.
- [184] Pauporté, T.; Aberdam, D.; Hazemann, J.; Faure, R.; Durand, R. *Journal of Electroanalytical Chemistry* **1999**, *465*, 88–95.
- [185] Hüppauff, M.; Lengeler, B. *Journal of the Electrochemical Society* **1993**, *140*, 598–.
- [186] Busch, M. Mechanistic insights into transition metal oxide catalyzed water oxidation. Ph.D. thesis, University of Gothenburg, 2012.
- [187] Busch, M.; Ahlberg, E.; Panas, I. *Physical Chemistry Chemical Physics* **2011**, *13*, 15069–15076.

- [188] Busch, M.; Ahlberg, E.; Panas, I. *Physical Chemistry Chemical Physics* **2011**, *13*, 15062–15068.
- [189] Busch, M.; Ahlberg, E.; Panas, I. *Journal of Physical Chemistry C* **2013**, *117*, 288–292.
- [190] Rossmeisl, J.; Qu, Z.; Zhu, H.; Kroes, G.; Nørskov, J. K. *Journal of Electroanalytical Chemistry* **2007**, *607*, 83–99.
- [191] Man, I. C.; Su, H.; Calle-Vallejo, F.; Hansen, H. A.; Martínez, N. G., J. I. Inoglu; Kitchin, J.; Jaramillo, T. F.; Nørskov, J. K.; Rossmeisl, J. *ChemCatChem*. **2011**, *3*, 1159–1165.
- [192] Lundberg, M.; Blomberg, M. R. A.; Siegbahn, P. E. M. *Inorg. Chem* **2004**, *43*, 264–274.
- [193] Zhao, Y.; Vargas-Barbosa, N. M.; Hernandez-Pagan, E. A.; Mallouk, T. E. *Small* **2011**, *7*, 2087–2093.
- [194] Miksis Jr, J.; Newman, J. *Journal of the Electrochemical Society* **1976**, *123*, 1030.
- [195] Battino, R.; Rettich, T.; Tominaga, T. *The solubility of oxygen and ozone in liquids*; American Chemical Society and the American Institute of Physics for the National Bureau of Standards, 1983.
- [196] Elsen, H.; Slowinska, K.; Hull, E.; Majda, M. *Analytical Chemistry* **2006**, *78*, 6356–6363.
- [197] Dubruel, P.; Vanderleyden, E.; Bergadà, M.; De Paepe, I.; Chen, H.; Kuypers, S.; Luyten, J.; Schrooten, J.; Van Hoorebeke, L.; Schacht, E. *Surface Science* **2006**, *600*, 2562–2571.
- [198] Xu, C. X.; Wei, A.; Sun, X. W.; Dong, Z. L. *Journal of Physics D: Applied Physics* **2006**, *39*, 1690–1693.
- [199] Greene, L. E.; Law, M.; Goldberger, J.; Kim, F.; Johnson, J. C.; Zhang, Y.; Saykally, R. J.; Yang, P. *Angewandte Chemie, International Edition* **2003**, *42*, 3031–3034.
- [200] Greene, L.; Law, M.; Tan, D.; Montano, M.; Goldberger, J.; Somorjai, G.; Yang, P. *Nano Letters* **2005**, *5*, 1231–1236.

- [201] Rasband, W. ImageJ. 1997-2012; <http://imagej.nih.gov/ij/>.
- [202] Zhou, J.; Xu, N.; L., W. Z. *Advanced Materials* **2006**, *18*, 2432–2435.
- [203] Han, P.; Bartels, D. M. *Journal of Physical Chemistry* **1996**, *100*, 5597–5602.
- [204] Oelkers, E. H.; Helgeson, H. C. *Geochimica et Cosmochimica Acta* **1988**, *52*, 63–85.
- [205] Goux, A.; Pauporte, T.; Lincot, D. *Electrochimica Acta* **2006**, *51*, 3168–3172.
- [206] Elias, J.; Tena-Zaera, R.; Lévy-Clément, C. *Journal of Electroanalytical Chemistry* **2008**, *621*, 171–177.
- [207] Khajavi, M. R.; Blackwood, D. J.; Cabanero, G.; Tena-Zaera, R. *Electrochimica Acta* **2012**, *69*, 181–189.
- [208] Eriksson, G. *Analytica Chimica Acta* **1979**, *112*, 375–383.
- [209] Peterson, R.; Fields, C.; Gregg, B. *Langmuir* **2004**, *20*, 5114–5118.
- [210] Kuiken, H.; Bakkers, E.; Ligthart, H.; Kelly, J. *Journal of the Electrochemical Society* **2000**, *147*, 1110–1116.